Emergence of chemotherapy resistance in cancer: microenvironments, genomics, and game theory approaches

Amy Wu

A Dissertation
Presented to the Faculty
of Princeton University
in Candidacy for the Degree
of Doctor of Philosophy

Recommended for Acceptance
by the Department of
Electrical Engineering
Adviser: Professor James C Sturm

June 2015

Abstract

Most cancers are still incurable because resistance to therapy is inevitable. Cancer cells usually acquire chemotherapy resistance due to two properties of cancer: adaptive cellular response to a heterogeneous microenvironment, and nonlinear interactions among various types of cells in a tumor community. In this thesis we construct *in vitro* heterogeneous tumor microenvironments to gain physiologically relevant information of phenotypic properties of cancer, cancer genomes, and interactions among various cells. Here we focus on metastatic breast cancer and multiple myeloma, a top five common cancer and blood cancer, respectively.

We first design drug gradient devices to mimic a tumor microecology during chemotherapeutic treatment, and assess multi-day spatio-temporal dynamics of breast cancer cells. Elevated resistance to doxorubicin (a chemotherapeutic drug) of breast cancer cells has been observed in a doxorubicin gradient based on proliferation rate, cell morphology, and cell motility. We test the hypothesis of horizontal gene transfer in breast cancer as a mechanism to diversify a population and enhance cellular adaptability to drug.

We then investigate genomic aspects of the rapid emergence of 16-fold elevated doxorubicin resistance in multiple myeloma (MM), which is achieved in a doxorubicin gradient within two weeks. We analyze RNA-sequencing data of the emerged resistant MM against non-resistant MM. Strikingly, we discover that mutational cold spots are ancient genes, maintaining the fitness of cells and playing an important role in elevated drug resistance. Furthermore, we probe the interacting population dynamics of MM and bone marrow stromal cells in a doxorubicin gradient. By developing a spatial model inspired by game theory, we successfully predict the future densities of multiple myeloma and stromal cells in such heterogeneous environment.

Finally, we suggest that our approaches, including microfluidics experiments, next-generation sequencing analyses, and quantitative modeling, can provide deeper in-

sights on the emergence of therapy resistance in cancer and implications of novel therapy design.

Acknowledgements

First and foremost, I would like to thank James Sturm for being an excellent Ph.D. advisor in conducting research and career development, and encouraging me to become an independent researcher. I would like to thank Robert Austin for giving me the opportunity to do research in his lab and leading a fantastic voyage in the physics of cancer. This is a team with an atmosphere of innovation and exploration, which I will definitely miss in future.

My special thanks to Guillaume Lambert and Kevin Loutherback for initially introducing me to the equipment, microscopes and facilities in the lab after I joined the lab. I would like to thank Qiucen Zhang and David Liao for countless discussion that are tremendously inspiring and helpful. I am grateful to my colleagues Liyu Liu, Bo Sun, Jonas Peterson, Julia Bob, Karen Malatesta, Jason Puchalla, Saurabh Vyawahare, Yu Chen, Joseph D'Silva, Ke-Chih Lin, John Bestoso, Temple Douglas, Eduardo Contijoch, Vladimir Kirilin, Jie Wang, and Brandon Comella for our random and interesting discussions about research and lives.

Due to the Physical Science Oncology Center (PSOC) program, I have been fortunate to collaborate with cancer biologists, oncologists, and theorists outside of Princeton. I appreciate to work with my collaborators Kenneth Pienta at Johns Hopkins Medical Institute, Chira Chen-Tanyolac and Thea Tlsty Laboratory at University of California-San Francisco, John Kim and Nader Pourmand Laboratory at University of California-Santa Cruz, Zayar Khin and Robert Gatenby Laboratory at Moffitt Cancer Center, Fernando Lopez-Diaz and Beverly Emerson Laboratory at Salk Institute, Atif Kahn at Cancer Institute of New Jersey, and Christopher McFarland from Leonid Mirny Laboratory at Massachusetts Institute of Technology.

This work was performed at the Princeton Institute for the Science Technology of Materials (PRISM) Micro/Nano Fabrication Laboratory. I appreciate the help from clean room staffs, especially Joe Palmer and Pat Watson. The research described

was supported by National Cancer Institute grant U54CA143803. I am grateful for the support from PSOCs program managers, especially Michael Espey and Larry Nagahara.

I thank my parents for their excellent support throughout the years. Their experience as graduate students in the U. S. and as professors at Taiwan encourages me tremendously. Finally, thanks to my husband, Yu-Cheng Tsai, for sharing all the challenging and joyful moments since we had become Ph.D. students at Princeton.

To my parents and my husband, No. 1 Yu.

Contents

List of Tables

List of Figures

Chapter 1

Introduction

1.1 Motive

Although numerous "Wars on Cancer" have been declared, mortality rate of many types of cancer has not dropped significantly for the past few decades. The major reason of this failure is metastasis: cancer cells spread into different organs from a primary tumor, become not operable, and usually become resistant to the original chemotherapy used to keep the tumor in check. Therefore, a clearer knowledge of how cancer metastasizes and how therapy resistance emerges is one of the most pressing needs for reducing cancer mortality.

In the past, most attempts to understand cancer have been focused on the signaling pathways that result in the hallmarks of cancer, for examples, how cancer cells grow, divide, avoid death, and invade [1]. Thanks to the progress of molecular biology and genomics, we have learned which proteins may enhance tissue invasion or which proteins induce therapy resistance. Although we know the size of human genome is composed of 3 billions of nucleotides, the function of most regions are still unknown; also, novel "important" human genes that regulates the hallmarks of cancer are still being discovered in a rapid and unlimited manner. This seems to be good news

for pharmaceutical companies because the list of potential "targets" for developing cancer therapy is still expanding. However, most therapies, including chemotherapy, radiation therapy, and targeted therapy, are found to merely extend the patients' survival for a few months or years and eventually fail.

Why is curing cancer so challenging? There is a growing awareness that cancer genomic landscape is highly heterogeneous and unstable [2]. More specifically, genomic landscape varies across different regions within a tumor, among different tumors in a patient, and also varies across different patients. Cancer therapy might be able to inhibit a subpopulation of cancer cells but not all of them. Additionally, cancer cells change rapidly in response to stress, a threat to cell survival. Regarding the heterogeneity, instability, and adaptability of cancer, physics becomes an alternative perspective to tackle the cancer problem.

Since cancer is a mixture of various types of cells and keeps changing with time, the spatial distribution and temporal dynamics of cancer are very essential for understanding the fundamental aspects of cancer. Physics, the study of matter and its motion through space and time, becomes a promising methodology to study the dynamics of cancer. For example, cancer is still poorly prognostic because quantitative information such as abundance of key molecules or various cell types, their spatial distribution, and their rates are still unknown. This quantitative information will be helpful for studying their non-linear interaction and potential effects on malignancy transformation. Therefore, the approach of the physical sciences, such as quantitative measurements or analytical modeling, may provide insights on understanding the fundamental mechanisms and control of cancer initiation, progression, therapy resistance, and metastasis.

1.2 Physical Sciences Oncology Centers (PSOCs)

With the aims to address some of the major questions in cancer research, the National Cancer Institute launched 12 Physical Sciences-Oncology Centers (PS-OCs) to support the integration of physical sciences and cancer research in 2009. Our center, Princeton Physical Sciences-Oncology Center (Princeton PS-OC), focuses on how to understand the evolution of cancer resistance to chemotherapy.

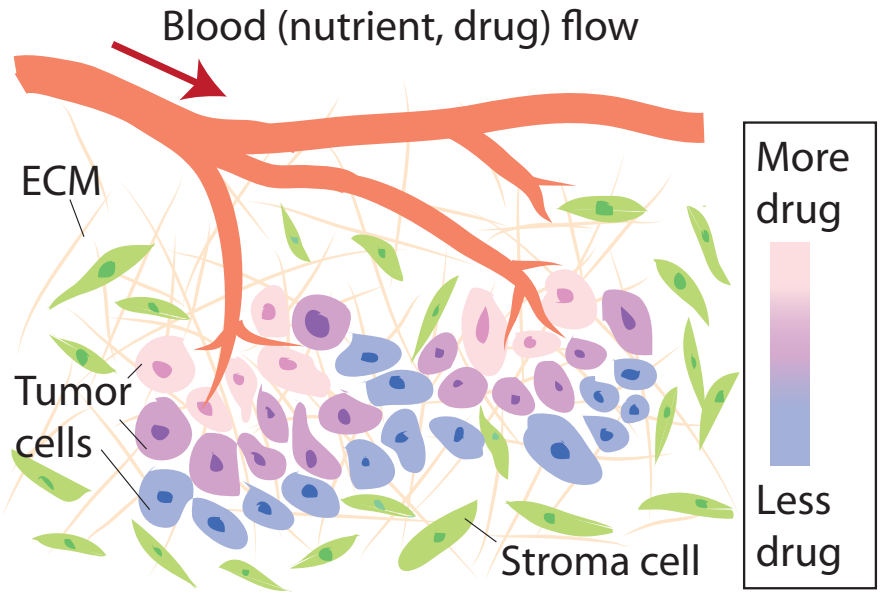

Figure 1.1: **Tumor microenvironment.** Blue cells, purple cells, and pink cells are cancer cells exposed to low, medium, and high levels of drugs, respectively. Green cells: stromal cells, neighboring non-cancer cells. ECM: extracellular matrices.

The emergence of cancer resistance is an evolutionary process since it is associated with a variaty of traits, environmental selection of the fittest, and heritability of fitness. Our hypothesis is that the tumor microenvironment provides a complex fitness landscape for cancer cells, in which blood vessels provide rich nutrients, oxygens, and drugs (during chemotherapy treatment) to certain part of a tumor, but in other regions within the tumor, the tumor is poor in nutrients, oxygens, and drug (Fig. 1.1). Therefore, the drug concentration in the tumor core may be insufficient to kill all

cancer cells and these surviving cancer cells might propagate toward the nutrient-rich blood vessel, then mutate, become reproducible and drug resistant. More specifically, our approach focuses on microfabrication techniques to engineer microenvironment, with drug gradients or glucose gradients, for exploring the origin and dynamics of cellular adaptation to stress.

1.3 Microhabitats: acceleration of evolution

With some clues about rapid evolution, we also adopt the concept of Darwin's living laboratory: the Galápagos Islands, a unique set of small islands relatively close to each other, as shown in Fig. 1.2. In the Galápagos islands, the sizes of the birds' beaks changed to reach food in response to drought within decades, not thousands of years. So why could the evolution of beaks proceed so rapidly? The mathematical form of population and evolutionary dynamics can be found in Sewell Wright's pioneering work [3]. Simply speaking, if a population is separated into multiple subpopulations in microhabitats, distinct species may emerge in response to local environments and the most fit specie can dominate in a smaller population (a process called fixation), easier and faster than in a larger population. Furthermore, if these microhabitats are weakly connected to each other across a fitness landscape, such as a stress gradient, then the stress-resistant specie may migrate to neighboring microhabitats in search of food and space, and gradually dominate the entire population.

Can we have our own Gálapagos Islands for experimental validation of rapid evolution? Yes. Using microfabrication techniques, we can scale down the Gálapagos Islands from kilometers to micrometers, probing the evolution of microorganisms instead of birds' beaks. Qiucen Zhang *et al* in Princeton PS-OC have demonstrated a fascinating example of "engineered Galápagos Islands", in which the resistance of bacteria to antibiotic developed within 20 generations, with as few as 100 bacte-

Figure 1.2: **Galápagos Islands: Darwin's living laboratory.** Image from the Distance Between Website (http://disween.com/galapagos-islands.html).

ria in the initial inoculation. Also, the resistant bacteria genome revealed that 4 novel functional mutations emerged and fixed, resulting in the antibiotic resistance [4]. This work explores the striking role of connected microhabitats combining with stress gradients in the acceleration of emergence of bacterial antibiotic resistance.

1.4 Bacteria versus cancer

Then, how is bacterial evolution related to oncology? First of all, human cells and bacteria have similar DNA repair and stress response mechanisms; when these mechanisms are defective, human cells become more susceptible to tumorigenesis, and bacteria increase their adaptability [5]. Also, tumor microenvironments and bacteria biofilms share several components such as colony formation, heterogenous fitness landscapes, extracellular matrices (ECM) which hinder the motion of cells, and the emergence of mobile (metastatic) cells which break through the ECM [5, 6]. There-

fore, the study of rapid bacterial evolution in engineered microenvironments provides a framework for exploring rapid evolution of cancer.

Although the bacteria model is a great tool for studying cancer, bacteria and human cancer are very different at many physical aspects such as size, motility, and doubling time. Such difference poses several challenges, and a detailed discussion is presented in Chapter 2 and Section 4.2.

So, this is where we started.

1.5 Thesis organization

In this thesis, we focus on generating chemotherapy gradients to mimic tumors, and explore how and why chemotherapy gradients and microhabitats accelerate the emergence of cancer resistance.

First we study breast cancer, the second most common cancer in women in the United States. Chapter 2 describes the rapid adaptive behaviors of cancer cells in chemotherapy gradients, such as cell proliferation, death, and motility. In Chapter 3, we test an hypothesis of how advantageous (or drug resistant) cancer cells may spread into a population: horizontal gene transfer.

We then study on multiple myeloma, a hematologic cancer which frequently occurs at many sites in the bone marrow. In Chapter 4, we demonstrate the rapid emergence of myeloma resistance in engineered microenvironments with chemotherapy gradients and microhabitats. Then we analyze the biomolecular signatures of resistant myeloma genome and discover the role of mutational cold spots in cancer resistance.

In order to explore environment-mediated drug resistance [7, 8], which involves cancer cells and stromal cells, we describe the non-linear interaction of myeloma and bone marrow stromal cells in such an engineered microenvironment, including cooperation and competition, in Chapter 5.

In Chapter 6, we demonstrate the technology transfer of metronomic dosing chip, two-dimensional gradient chip, and the Death Galaxy chip (combining metapopulation and "various drug gradients") to collaborators from University of California at San Francisco, Salk Institute, and Johns Hopkins Medical Institute. Preliminary experiments conducted in our collaborating labs within the Princeton Physical Sciences-Oncology Center are also demonstrated in this chapter.

We summarize these studies and discuss future directions in Chapter 7. And finally, the instrumentation, experimental protocols and data analysis procedures are presented in the appendices.

Chapter 2

Breast Cancer: Cell Motility and Drug Gradients

Cancer cells evolve drug resistance to chemotherapy within the tumor microenvironment. Although it is widely accepted that tumor microenvironment provides a sequential selective pressure for pre-existing mutants within the population[9, 10, 11], an additional contribution to rapid cancer evolution is stress-induced mutagenesis, following by the emergence of adaptive phenotypes [12, 5]. Chemotherapeutic drugs such as doxorubicin, can cause DNA damage and generate mutations for cancer cells. Further, mutagenic drug gradients in the tumor microenvironment lead to a spatially-dependent fitness landscape of the cancer cells and can further accelerate the evolution of drug resistance if the cells are motile across the gradient [13, 5].

Using a bacteria model, we recently demonstrated how a spatial gradient of antibiotic concentration in a metapopulation accelerated the evolution of antibiotic resistance [4]. We would expect similar processes to occur in cancer cell metapopulations as well. Because cancer cells have a much longer doubling time ($\sim$1 day) compared to that of bacteria ($\sim$ 30 minutes), similar experiments with cancer cells take nearly two order of magnitude more time (days vs hours) than those for bacteria. This presents

two experimental challenges: (i) the creation of a drug gradient stable for weeks, and (ii) the creation of an environment hospitable for healthy cell growth over the course of weeks. Once these conditions are established, it is possible to probe in an *in vitro* system the complex driving forces of resistance in systems that are *in vivo*.

Microfluidic devices have become a versatile platform to provide precise concentration gradient control for understanding various biological systems and controlling the population size [14, 15, 16]. Gradient generating devices can be classified as: (i) the static generators which are solely based on diffusion[17, 18], and (ii) the constant flow generators[19, 20, 21, 22]. In this chapter, we adopt the constant-flow approach because it is capable of creating time-independent stable gradients. However, to date it has been challenging to grow mammalian cells in such platforms [23, 24]. Thus, the time scale of previous studies of breast cancer chemotaxis in a gradient of epidermal growth factors (EGF) was limited to 24 hours [25]. In this chapter we then develop a microfluidic platform for the long-term (multi-week) culture of breast cancer cells (MDA-MB-231) in a stable gradient.

2.1 Effects of fluid flow on cell culture

We first tested the "pre-mixer" approach [19] in which six pre-mixed streams (200 μm wide) of increasing drug concentrations flow in parallel into a 1.2-mm-wide culture chamber adjacent to one another (Fig. 2.1A). Subsequent diffusion causes the boundaries between the streams to be blurred and create a smooth gradient in the culture chamber (Fig. 2.1B). The concentration profiles can be maintained down through the culture chamber if the flow speed is fast enough (i.e. v>3mm/s) (Fig. 2.1C). If the flow speed is too slow, however, (i.e. v<0.1mm/s), diffusion flattens the concentration profiles as the liquids move along the culture chamber (Fig.2.1D) and the gradient is lost.

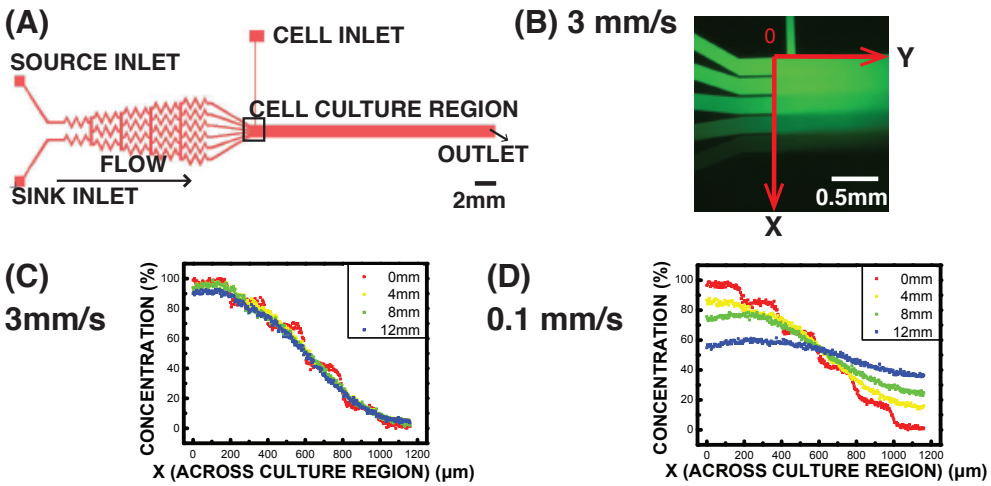

Figure 2.1: **Premixer design and gradient characterization.** A. Top view of premixer (red, channels). Source inlet and sink inlet were supplied with drug solution and growth medium, respectively. The two streams were repeatedly mixed and then divided into more streams. Then six streams were introduced into a single channel (cell culture region) and mixed again. B. Fluorescein gradient with average flow speed v=3 mm/s, zoomed in from the black square in A. We characterized the concentration gradient profile across cell culture region (X-axis) and observed its mixing along cell culture region (Y-axis). C. Fluorescence intensity in consecutive cross sections (Y=0, 4, 8, 12 mm) along the chip (v=3 mm/s). D. Fluorescence intensity in consecutive cross-sections (Y=0, 4, 8, 12 mm) along the chip (v=0.1 mm/s).

The minimum flow rate requirement is significant, because we found that even with zero drug concentration (only fresh media flowing in the culture region in all channels) fluid flows as low as 8 μm/s in the culture region would adversely affect the growth of MDA-MB-231 cells (supplied by Thea Tlsty Laboratory at University of California at San Francisco, cell culture protocol is presented in Appendix B.3). After 48 hours without flow, MDA-MB-231 cells in the culture chamber showed a healthily elongated morphology (Fig. 2.2A, top), but under a 16 μm/s of flow (from 24 to 48 hours), the cancer cells became round and blebbing (Fig. 2.2A, bottom). Furthermore, the population under flow decreased in 72 hours because several cells became detached from the substrate and flushed away by the flow, even at flow speed of only 8 μm/s (Fig. 2.2B). One reason that the cells grew poorly under a continuous

flow may be the loss of secreted growth factors [14], although replacing the fresh medium with conditioned medium, used medium enriched with cell-derived factors, did not substantially alter the results (Fig. 2.2C). More complicated mechanisms such as flow-mediated mechanotransduction also explain the disruption of cell growth by shear stress [26].

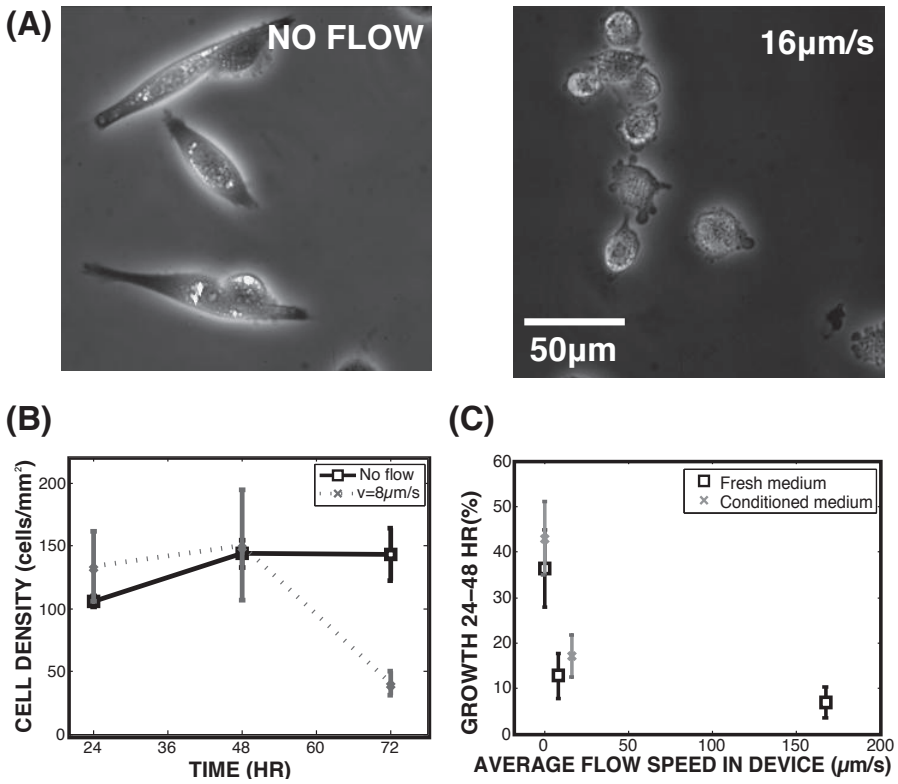

Figure 2.2: **MDA-MB-231 cells at various flow speeds in premixer device without drug gradient.** A. Image of cancer cell after 48 hours of cell inoculation (no flow vs. average flow speed v=16 μm/s) from 24 to 48 hours after cell inoculation. B. Population density vs time of MDA-MB-231 cells in premixer device with flow (v=8 μm/s) and without flow. C. Percentage increase of population density from 24 to 48 hours at various flow speeds with fresh or conditioned media.

2.2 Long-term on-chip cell culture

As discussed in Sec. 2.1, we found that a necessary condition for successful long-term (16-day) MDA-MB-231 cell culture is the absence of any continuous fluid flow above 1 μm/s in the culture region, which led us to the cross-channel diffuser device architecture. Cross-channel diffuser gradient device can generate stable gradients with low fluid flow rate in culture region [27, 21]. We developed a cross-channel diffuser approach for long term cell culture using silicon microfabrication techniques (Appendix B.1). This device separates the culture chamber (1 mm$\times$1mm, with a depth of 150 μm in our case) from the flow channels on opposing sides of the chamber, one of which supplies the drug and the second of which has a flow of media free of drug. These two channels are separated from the culture region by a linear array of microposts, which have a narrow gap of 5 μm between them. The arrays of posts serve as a perfusion barrier, which allows the drug to diffuse through the gaps between the posts but do not allow a substantial fluid flow from the source and sink channels through the gaps into the culture chamber (Fig. 2.3 A and B). To ensure there is no flow in the culture chamber, the external connection through the left/right ends (inlet/outlet for cell loading) are closed during cell culture (as shown in Fig. 2.3A).

Using continuous source and sink flow in the outer channels with an average flow rate of 100 μm/s (supplied by syringe pumps), the resulting gradient profile was linear, when tested using fluoroscein, which has a similar diffusion coefficient to doxorubicin, drug we will use later for our experiments. By maintaining a constant flow in the outer source and sink channels, the gradient was stable for 72 hours (Fig. 2.3 D and E). In contrast to static gradient devices in which there is no flow to refresh the source/sink regions outside the culture region so that gradient can be maintained up to 24 hours [17, 18], in our devices the gradients can in principle be maintained as long as we supply a constant flow in source and sink channels. To measure fluid flow speeds, in one case we added fluorescent beads to the input media. In the culture

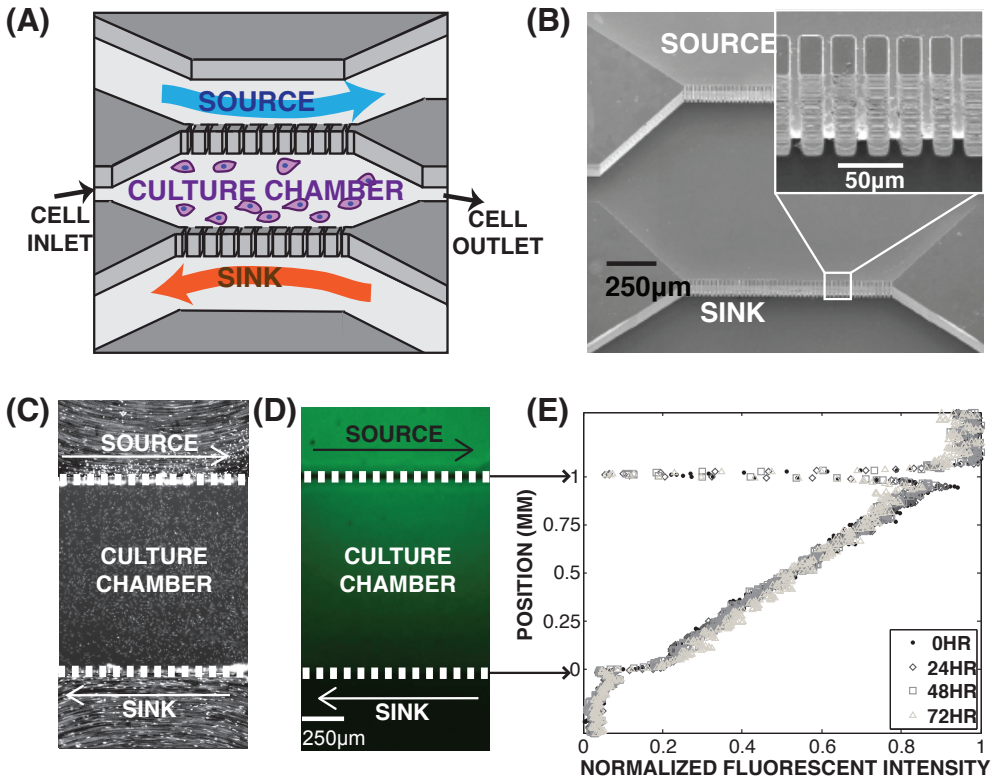

Figure 2.3: **Cross-channel diffuser design and gradient characterization.** A. Schematic of the cross-channel device. B. Scanning electron microscopic image of the cross-channel device etched into silicon (depth:150 μm). The gap between the microposts (20 μm x 40 μm) is 5 μm. The source and sink channels were 3 mm wide. C. Characterization of flow speeds using fluorescent beads (diameter: 1 μm). Exposure time: 2 s. D. Fluorescent micrograph of fluorescein gradient, with source and sink flow velocities of 100 μm/s. E. Gradient profile across the culture chamber.

chamber, we found the fluid flow speed was less than 1 μm/s, over 100 times lower than in the side channels and comparable to physiologic level of interstitial flow about 0.5 μm/s (Fig. 2.3 C) [28].

In a control experiment without any drugs (flowing fresh growth media in both the source and sink channels), the MDA-MB-231 cells grew well in the chip for more than 2 weeks (Fig. 2.4 A). The cells showed healthily elongating morphologies and became more confluent with time. The growth curves of the cells (Fig. 2.4 B) show that the cells grew in a log-phase for 4 days with the doubling time of 2.2 days (in chips) and

2 days (in tissue culture flasks), and then entered the stationary phase, where they remained for the rest of two weeks. Creating such a hospitable environment for the cancer cells on the microchips was an experimental challenge, the critical steps for which are described in more detail in Appendix B.3.

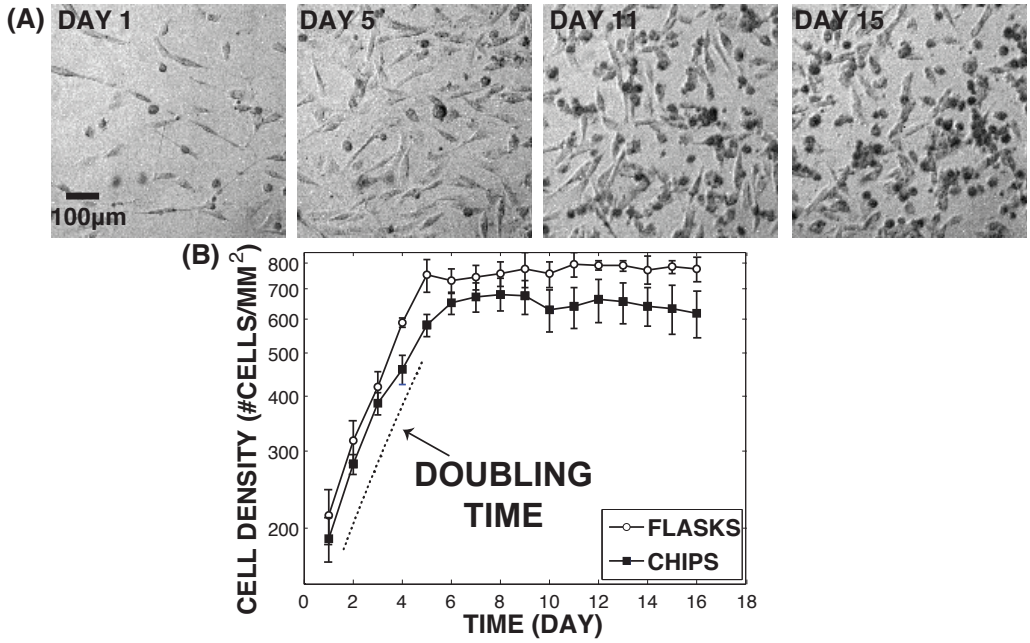

Figure 2.4: **Control experiments of MDA-MB-231 cells in the cross-channel diffxer without drug** A. Micrographs of MDA-MB-231 cells in the culture chamber of the cross-channel device in time series from day 1 to day 15. B. Growth curves of MDA-MB-231 cells in culture chamber of the cross-channel mixer vs. conventional tissue culture flask. In the mixer, the flow rate in the source and sink channels was 100 μm/s. For the flasks, the medium has been replaced every 4 days. The doubling time in the cell culture chamber is 2.2 days and is 2 days in tissue culture flasks. Error bars represent the standard deviation of three replicates.

2.3 Population dynamics of breast cancer cell adaptation in a microenvironment with drug gradients

We use doxorubicin, a genotoxic chemotheraputic drug, as the stressor to create a drug gradient. Unfortunately in the literature, the IC50 (drug concentration that inhibits the viability of 50% of population in a drug-free growth medium) of doxorubicin for MDA-MB-231 cells varies from 25 nM, 88nM to 2.7 μM [29, 30, 31]. Thus, to find the desired dosage for our gradient experiments, we compared the effect of different doxorubicin concentrations on our MDA-MD-231 cell line for multiple days in tissue culture flasks (Fig. 2.5).

We found that 200nM of doxorubicin effectively inhibited the growth of MDA-MB-231 after 24 hours and also induced morphological changes in 96 hours (Fig. 2.5 A and B), and chose this value for the concentration for the input stream for the channel on the source side of the culture chamber. Thus, after loading the cells into the culture chamber of our gradient device and a 24-hour attachment period, a doxorubicin gradient was then constructed by pumping 200nM of doxorubicin at the source channel and pumping growth medium alone at the sink channel.

That doxorubicin is a genotoxic drug which damages the chromatin of cells was shown in cells exposed to 200nM of doxorubicin in the chip. After 72 hours, we used a Single Cell Gel Electrophoresis assay (SCGE) and observed an average tail moment length of 27 μm (Fig. 2.5 C). In this assay, broken DNA migrates farther in the electric field, resulting a comet tail at single cell level (experiment protocol presented in Appendix B.6). This shows that 72-hour exposure of 200nM doxorubicin is adequate to induce significant DNA damage in MDA-MB-231 cells. The resulting distribution of cells was imaged using bright field microscopy every 25 minutes over 72 hours.

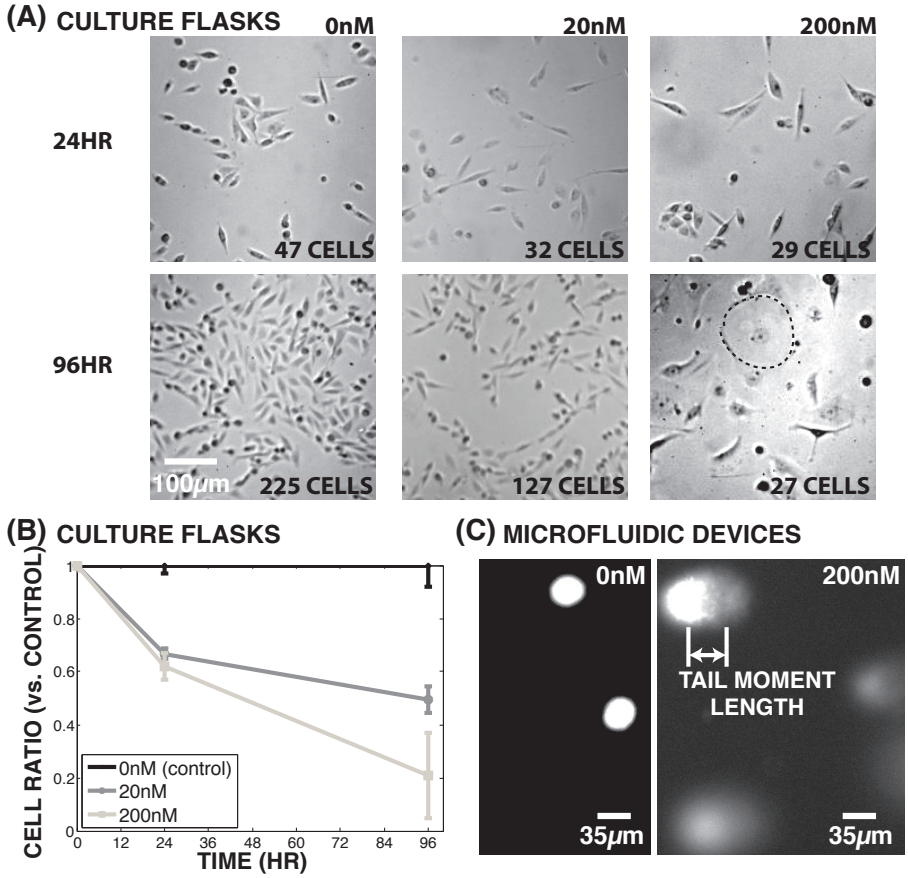

Figure 2.5: **MDA-MB-231 cells in various concentrations of doxorubicin.** A. Micrographs of MDA-MB-231 exposed to 0 nM, 20 nM, and 200 nM of doxorubicin for 24 hours or 96 hours in the tissue culture flasks. Under 200 nM of doxorubicin, the cell growth was effectively inhibited in 24 hours and cells became large and flattened significantly in 96 hours (for example, the cell circled by the dotted line). B. Population ratio to control experiment (0 nM) vs. time in the tissue culture flasks. Error bars represent the standard deviation of three replicates. 200 nM of doxorubicin inhibits 50% of cells after approximately 48-hour exposure (IC50). C. DNA damage (comet assay) of the cells from the microfluidic mixer after 72-hour doxorubicin exposure (0 nM vs. 200 nM). Fifteen cells have been analyzed in each concentration. The tail moment length (measured from the center of the head to the center of the tail) is 0 and 27.0 $\pm$ 8.4 μm for 0 nM and 200 nM, respectively.

Fig. 2.6 A shows the image of cells in the growth chamber at 0 hour (defined as after the 24-hour attachment period). Qualitatively, after 72 hours with the applied gradient, the cell density increased throughout the culture chamber, under all drug concentrations, and not surprisingly increased faster in the lower half (low drug re-

gion) of the culture chamber Fig. 2.6 B. To quantify the population versus space and time, we divided the culture chamber into 5 regions of interest along the gradient direction, with drug concentrations from top to bottom of 200-160 nM, 160-120 nM, 120-80 nM, 80-40 nM, and 40-0 nM, indicated by the dotted lines.

The cell density was uniform initially, in the 5 regions (between 260 and 300 cells/mm^2), and after 24 hours the cell population increased more significantly in the low drug region than the high drug region, forming a population gradient in response to the drug gradient (Fig. 2.6 B). Most surprisingly, the cell population in the high drug region (160-200nM) began to increase significantly after only 48 hours. It is also instructional to plot the cell density in each drug concentration region vs time (Fig. 2.6 C). One notes that in the low drug region, cells grow continuously from the beginning of the experiment, where in regions of increasingly higher drug concentration, there is a delay until the cell population starts growing. The delay increases with the drug concentration. Over the range of time for which we have data, after the delay, to first order the growth rates in all drug concentration regions are similar.

There are three possible ways that cancer cells in a fitness landscape can show growth at levels of a drug which should inhibit growth:

(i) Long-range random migration: If the cancer cells migrate rapidly and randomly on a length scale as large as the culture chamber in a drug gradient, they would survive longer in high drug region than in a uniform high drug environment since they would only spend a short portion of their life in the high drug region.

(ii) Long-range directed motion to regions of higher stress as resistance emerges: Conventional chemotaxis would be expected to drive the cells away from the high drug region. However, from a fitness advantage perspective it is advantageous for a cell to move towards regions of higher stress if resistance emerges because of reduced competition for resources such as glucose, oxygen, or space [32].

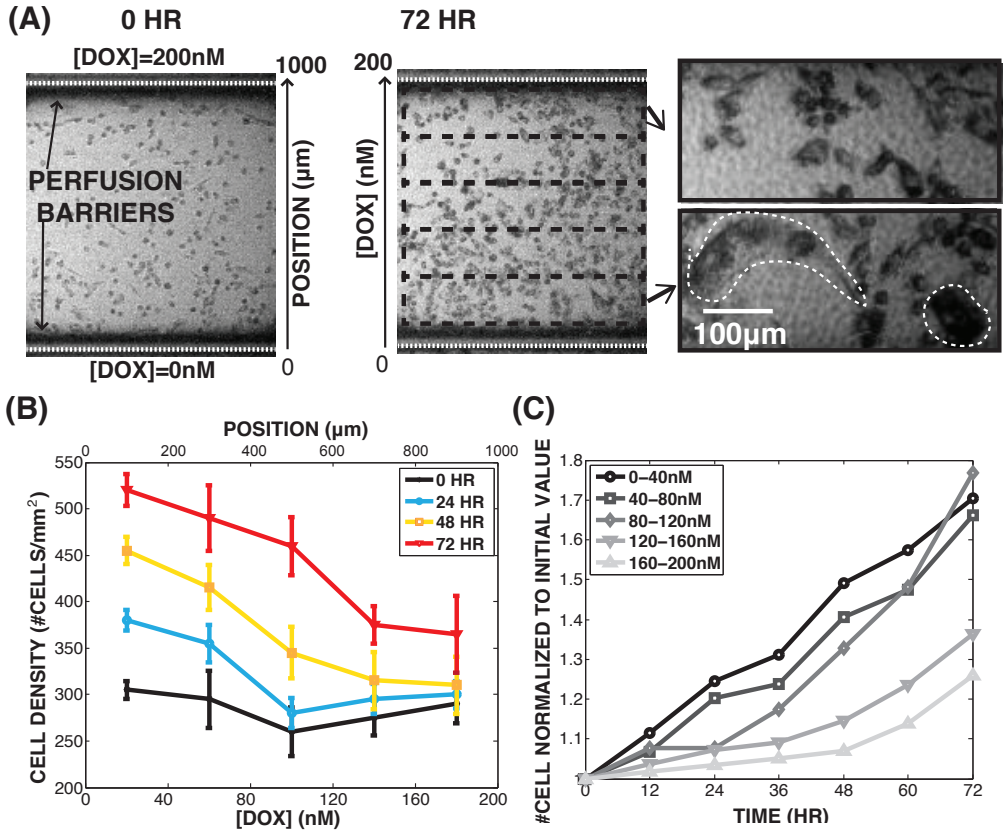

Figure 2.6: **MDA-MB-231 cells (0 to 72 hours) under doxorubicin gradient (200nM/mm).** A. Micrographs of the cells. The rows of the posts separating the culture chamber from the source channel (top) and sink channel (bottom) have been artificially added to the image for clarify. The source channel contains 200 nM of doxorubicin and the sink channel has 0 nM. The 72-hour image has schematically indicated 5 regions for different drug concentrations for counting cells. The cell morphology at the high drug region (160 to 200 nM) and the low drug region (0 to 40 nM) are compared. We observed some enlarged cells at the low drug region, circled by dotted lines. B. Cell population density in 5 regions (200 μm) of the culture chamber versus time. Error bars represent standard deviation of the data within 100 minutes of each time point, indicating the temporal variation due to cell migration and division. C. Normalized growth curves in different regions of interest. Each curve is normalized by its initial value.

(iii) Local evolution of resistance to the drug without any influence of migration of the cells. In this case the cells should show proliferation in the high drug region during our observation. Preexisting resistant cells would be selected and proliferate

proliferate regardless of the drug, and emergent resistant cells should show a delayed growth.

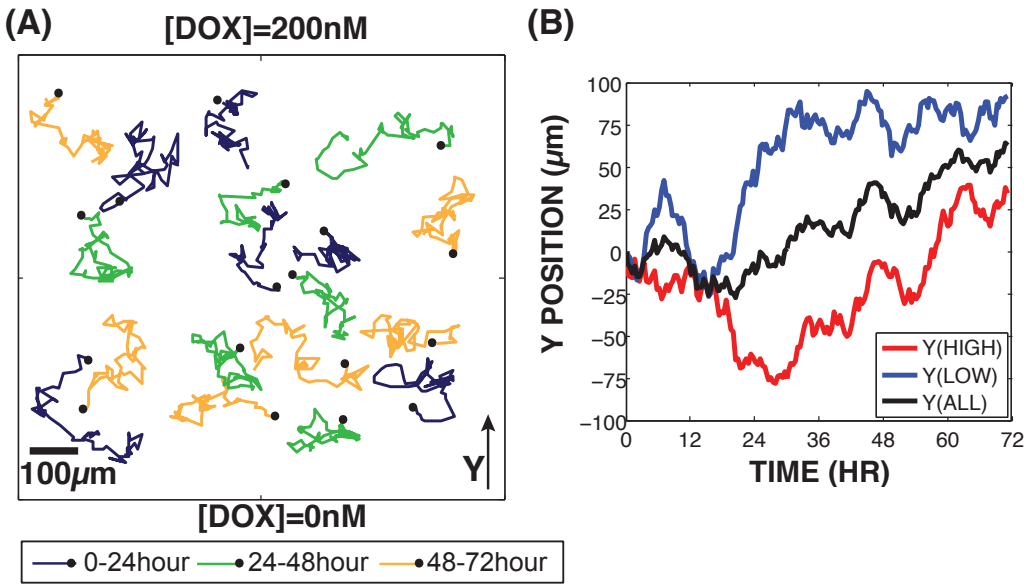

Figure 2.7: **MDA-MB-231 cell migration in a doxorubicin gradient (200nM/mm)** A. Movement of selected cancer cells in the doxorubicin gradient tracked over 3 time intervals. B. Integrated net displacement in the y direction (the drug gradient axis) for the six cells in the upper half of the culture region (high drug concentration) and lower half of the culture region and the net overall displacements for 12 individual cells.

To test these hypotheses, we first analyzed the trajectories of 12 individual cells at different positions within the doxorubicin gradient. Fig. 2.7 A shows the local trajectories of the individual cells over time. The information to be extracted here is that there is no obvious bias to the motions of the cells versus position in the gradient, and one must integrate the positions and the cells in different regions versus time to address the 3 hypothesis that we posed above. Fig. 2.7 B shows the integrated displacements, averaged over cells in the region, versus time. It is clear that (i) the cells do not move from the drug, that (ii) they move only over a net distance of 50 μm at most, for less than the total 1000-μm width of the drug gradient, and (iv) there is a biased movement towards the higher doxorubicin drug levels. The statistical

significance analysis of this biased motion is described in more detail in Appendix C.1.

In order to gain information on whether the cells acquired division capability at high drug region, we characterized the cell divisions in each bin in the drug gradient versus time. We count the number of cell divisions using a tracking software developed by Danusers Laboratory at Harward [33]. Then we define the cell proliferation rate as the accumulated number of cell divisions in each bin divided by the initial cell population in each 12-hour time span in each bin. And then we show the deviation of cell proliferation rate in each bin from the average proliferation rate over the entire culture chamber (Fig. 2.8). We find that the peak of the deviation of cell proliferation rate spreads from the low drug region to the high drug region with time. The cells in the high drug region gradually acquired greater division capability than that of the low drug region with time.

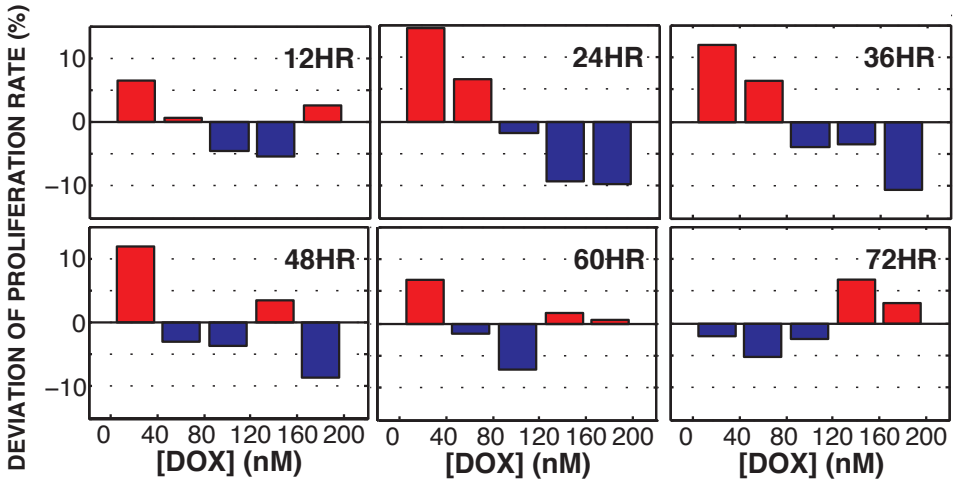

Figure 2.8: **Deviation of cell proliferation rate per 12-hour (in each bin) from cell division percentage of the entire chamber vs. time.** We count the number of cell divisions in each bin over every 12-hour period from 0 to 72 hours. The cell proliferation rate is defined as number of cell divisions divided by the initial population. Here, we show the deviation of cell proliferation rate in each bin from the average cell proliferation rate over the entire chamber.

2.4 Discussion

We have shown that stable long-term drug gradients can be engineered into a cell culture region with microfluidic methods, and that MDA-MB-231 cells can be successfully cultured for over two weeks in these on-chip environments without drugs. With a strong drug gradient applied (200 nM to 0 nM over 1 mm) to the culture chamber, the population density increases even in regions of high drug concentration within 72 hours. This population increase was not due to the fact the cells spent only a small fraction of their life in the high drug regions due to random motion. Instead, the cells migrated in a biased random motion towards the drug source because of reduced competition for resources, and successfully divided in the high drug region.

The competition for resources may be a combination of (i) space, due to contact inhibition of adherent cells, and (ii) metabolic resources, such as glucose or oxygen. The first one is obvious but one may ask, does the rate of resource consumption exceed the rate of resource replenishment by constant perfusion? Although we apply constant perfusion in cross-channel diffuser, cell-secreted growth factors may not be rinsed away since the cells grow well in cross-channel diffuser. It is possible that each cell becomes a local sink of metabolic resources and creates microheterogeneities in resource concentrations that can be detected by neighboring cells. The propagation of cell proliferation versus time from low drug to high drug region also suggests that the growth of cells in low drug regions confers an advantage to cells in adjacent regions with higher drug concentration. This advantage could be due to a diffusion of cell-secreted growth hormone, or other effect. One of the other mechanism is the focus of the next Chapter.

Chapter 4 and 5 will combine this drug gradient device with microhabitats and 3D culture, such microhabitats separate small populations and increase the fixation of mutations [5], [4].

Chapter 3

Horizontal Gene Transfer and Cancer Evolution

In Chapter 2, breast cancer cells (MDA-MB-231) develop doxorubicin resistance within 72 hours in a gradient of 0 to 200 nM of doxorubicin in a 1mm wide culture region [34]. However, the mechanism of how cancer cells rapidly acquired doxorubicin resistance in such environment remains unresolved. In this chapter, we test our hypothesis that cell-cell communication via transfer of genetic materials may diversify their genome and contribute to the emergence of the drug resistance.

3.1 Horizontal gene transfer in bacteria and cancer

One rapid process for acquiring a new combination of DNA among microorganisms is termed horizontal gene transfer. It is an effective mechanism for the exchange of genetic information. Horizontal gene transfer allows bacteria to acquire antibiotic resistance. Using this mechanism, bacteria do not have to wait for the right mutations to come along if they receive resistant genes from other already resistant cells. The process of horizontal gene transfer in bacteria is shown in Fig. 3.1. In a heterogeneous population of bacteria, some cells might contain a plasmid with antibiotic resistant

DNA sequence. When these bacteria are in contact with wild type bacteria without the resistant plasmid, a connection through pili might form and the plasmid can be copied. Then, both bacteria will then contain the plasmid, and the wild type cell will become resistant to antibiotics.

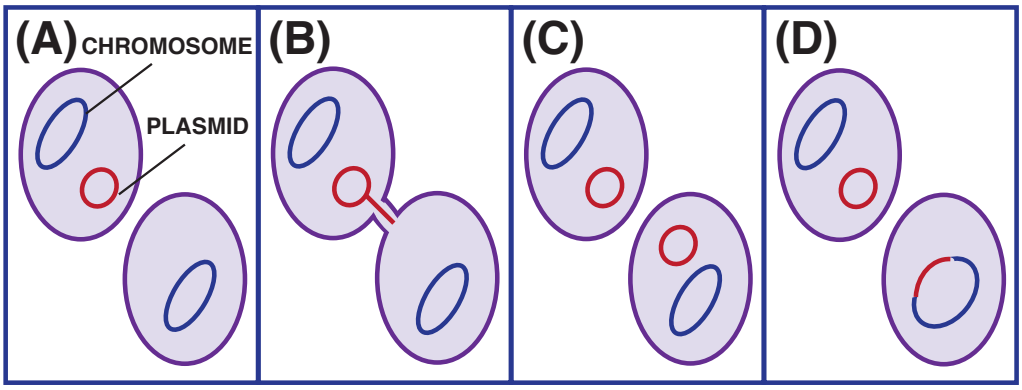

Figure 3.1: **Horizontal gene transfer in bacteria.** A. One bacterium contains a plasmid to be transferred. B. A connection (pilus) forms and the plasmid is copied. C. Both bacteria now contain the plasmid. D. The recipient may even integrate the plasmid into its chromosome.

Horizontal gene transfer between human cells within a tumor has been proposed to induce genetic instability and genomic heterogeneity. In contrast to bacterial horizontal gene transfer, it has been shown that activated oncogenes can be transferred in fibroblast cells by engulfment of apoptotic bodies. The accumulation of genetic changes may further lead to transformation of tumor malignancy [35]. Following works proposed that transfer of genes in cancer could be a method of rapidly acquiring chemotherapy resistance [36]. An alternative model of mammalian horizontal gene transfer is via cell fusion following by genomic hybridization. As shown in Fig. 3.2, the emerged hybrid cells have been observed in mice and exhibit a deregulated cell cycle and epigenomes of both parental lines [37].

Yet visualizing the dynamic process of horizontal gene transfer in cancer under chemotherapy stress still remains challenging. A common luminescent markers to

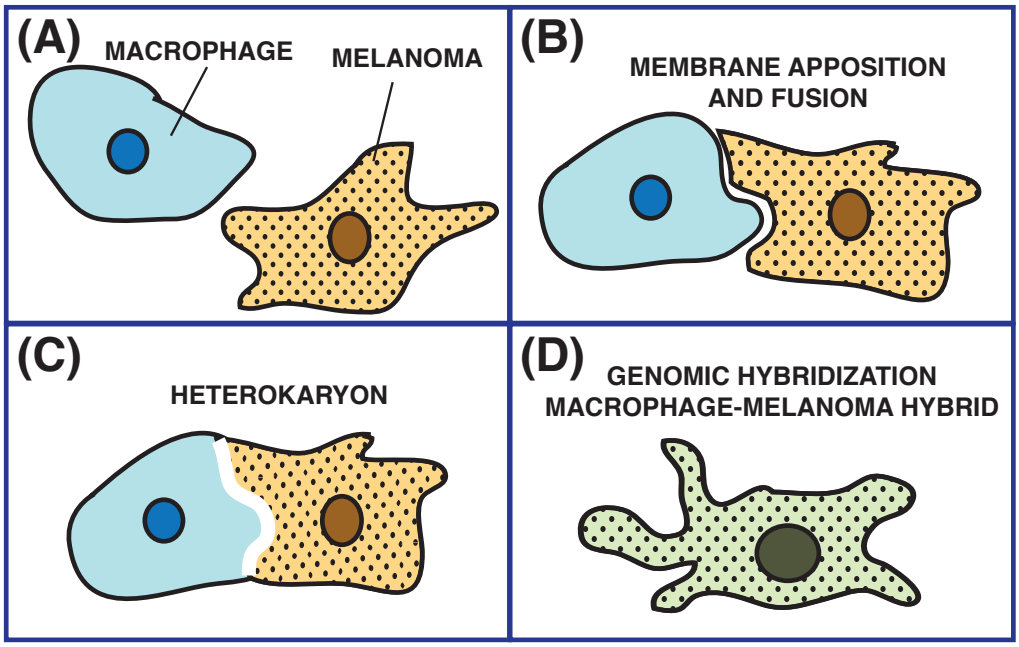

Figure 3.2: **A model of mammalian horizontal gene transfer via fusion.** A. A macrophage is attracted to a melanoma cell, which produces melanin and appears golden-brown in the cytoplasm. B. The macrophage and melanoma plasma membrane form side-by-side contact. Normally, it leads to ingestion of the melanoma cell. However, in some cases the two cells fuse. C. Following fusion a heterokaryon is formed with two nuclei separate in the cytoplasma. D. Genomic hybridization occurs and a mononuclear macrophage-melanoma hybrid emerges [37].

visualize the DNA, chromosomes and nuclei are DAPI or other fluorescent DNA dyes. Unfortunately, most DNA dyes are cytotoxic so it is hard to acquire dynamic information over an extended period (longer than 10 hours).

Direct horizontal gene transfer mediated by F pilus in bacteria has been demonstrated using a fluorescent protein fusion (SeqA-YFP) and real-time fluorescence microscopy [38]. The successfully transferred DNA was then found to occasionally split and segregate with different chromosomes, indicating the diversification of the genome by foreign DNA. Thus, fluorescent protein fusion vectors is a promising real-time marker to visualize the dynamics of horizontal gene transfer in cancer.

3.2 Research plan

Among various fluorescent protein fusion vectors, we chose histone-fluorescent protein fusion vectors in our study. Histones are found in eukaryotic cell nuclei that package and order the DNA into structural units to compose chromatin. As shown in Fig. 3.3 A, histones act as spools around which DNA winds. Since histones have high DNA affinity, they become an ideal candidate for tracing DNA from one cell to another cell.

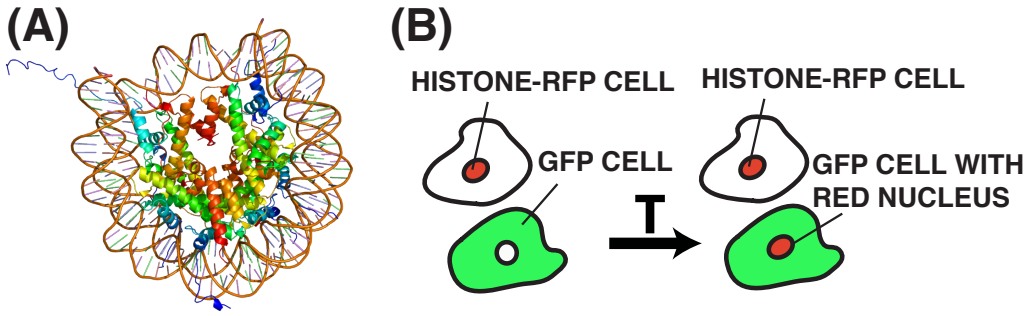

Figure 3.3: **Research method.** A. Complex between nucleosome core particle (histone) and 146 bp long DNA fragment (Protein Data Bank). B. Co-culture of GFP cells and histone-RFP cells. After time (t), if a red nucleus emerges in GFP cells, that would indicate foreign DNA (adhering to histone-RFP) might transfer to the GFP cell.

In this project, we co-culture breast cancer cells (MDA-MB-231, a courtesy from Beverley Emerson Laboratory at Salk Institute) expressing uniform GFP and the same cell line with H2B-RFP lentiviral vectors (Appendix B.2) under doxorubicin exposure (or not, as a control) for multiple days and acquire fluorescent images hourly. We choose to co-culture two groups of cells: one has GFP uniformly expressed over the cell body, and the other is specific in nuclei containing DNA. When a red fluorescent compartment emerges inside a green cell, the donor DNA are transferred to recipient cells (Fig. 3.3 B). The histones labeling vectors expressed in the donor cells may enable us to identify potential genomic integration incidence of the transferred DNA in the recipient cells.

3.3 Results

We mixed 1×10^4 metastatic breast cancer cells MDA-MB-231/GFP and 1×10^4 MDA-MB-231/H2B-RFP in each well in a 24-well plate.

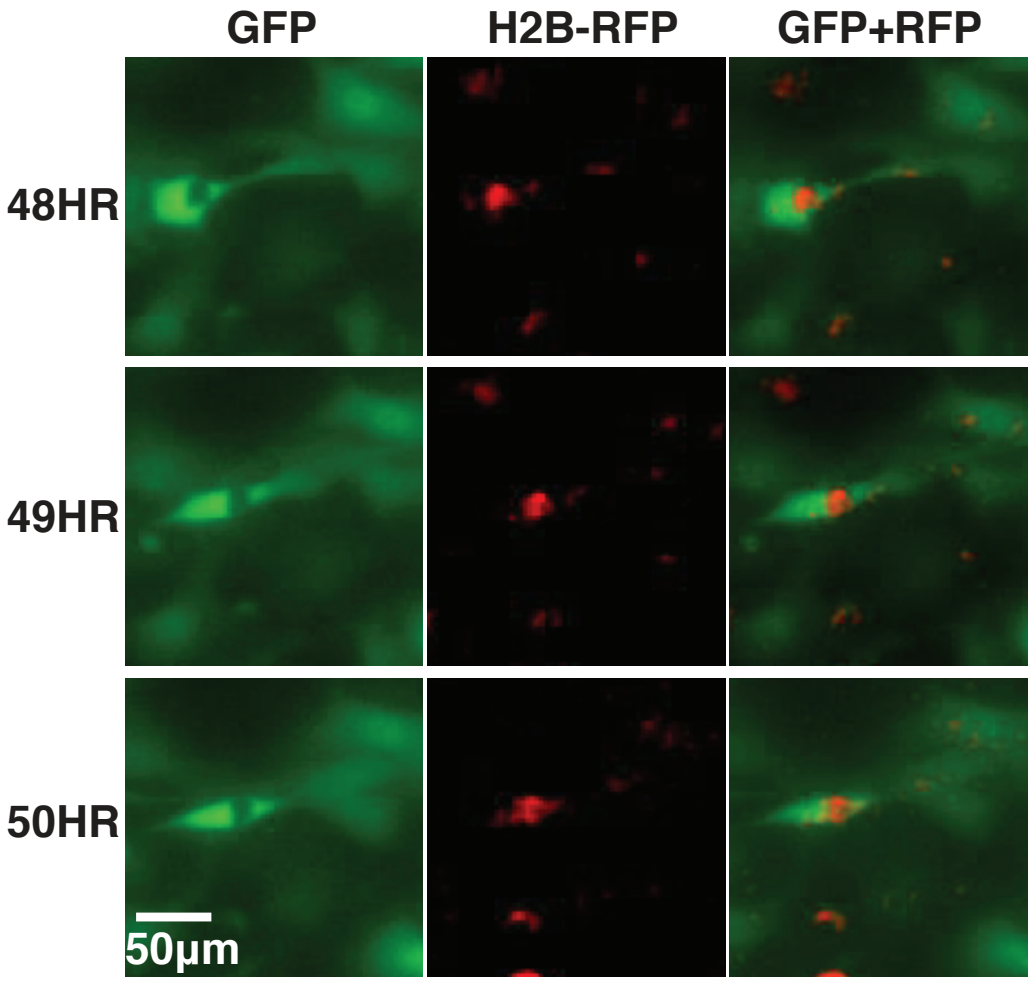

Figure 3.4: **Emergence of horizontal gene transfer in cancer under doxorubicin exposure.** Emergence of red fluorescent donor (H2B-RFP, in nucleus) within the recipient green cell (GFP) was observed by time-lapse microscopy at 48, 49, 50 hours of doxorubicin exposure (100nM).

In this preliminary study, we mixed two types of cells: one expressed GFP in cytoplasm, the other expressed RFP in histones (localized in nuclei). Among a 24-well plate, four wells (with a diameter of 15.6 mm) of cells were exposed to 100 nM of doxorubicin, and four wells of cells were supplied with regular growth medium (10%

FBS in DMEM). We used an inverted fluorescence microscope (Nikon TE-2000) with an on-stage incubator (Okolab) to take time-lapse images (Fig. A.2). Hourly green and red fluorescent images for 20 positions in each condition were taken for 80 hours.

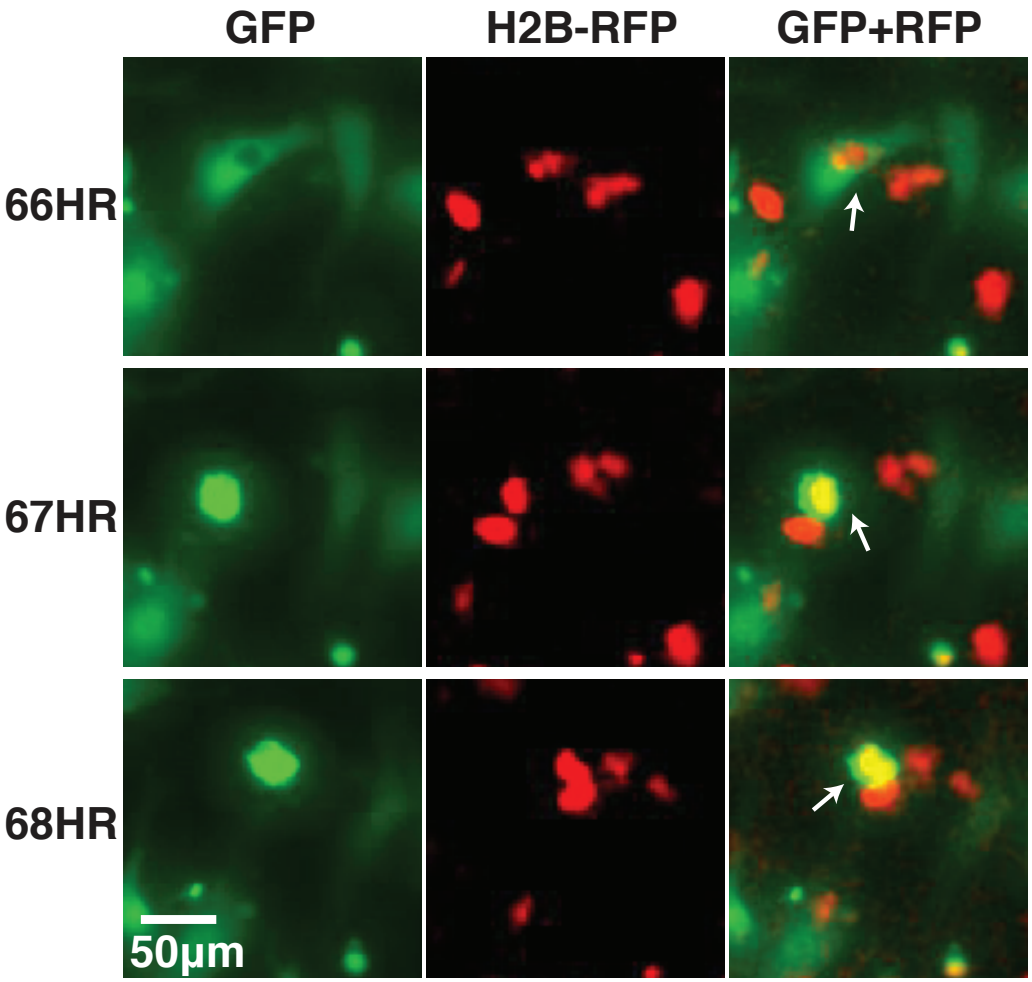

Figure 3.5: **Fate of horizontal gene transfer in cancer under doxorubicin exposure.** Red fluorescence of donor (H2B-RFP, in nucleus) within the recipient green cell (GFP) as followed by time-lapse microscopy at 66, 67, 68 hours of doxorubicin exposure (100nM). The merged cell eventually bursted in 67 hours.

In all, we observed red nuclei (H2B-RFP) emerged in 4 out of 262 GFP cells (1.5%) under 48-hour exposure of 100nM. As we traced the movement of green cells with red nuclei, we could exclude the scenario that two cells were overlapped (Fig. 3.4). The nuclei of GFP cells should not appear red unless they received DNA or

protein from H2B-RFP cells. This result shows that horizontal gene transfer occurs if cancer cells exposed to 100 nM of doxorubicin for 48 hours.

We then followed these recipient cells (green cells with red nuclei) to find out whether these cells become more resistant to doxorubicin. As shown in Fig. 3.5, the nucleus of the recipient cells divided within 66 hours but these cells eventually failed to divide and bursted within 70 hours.

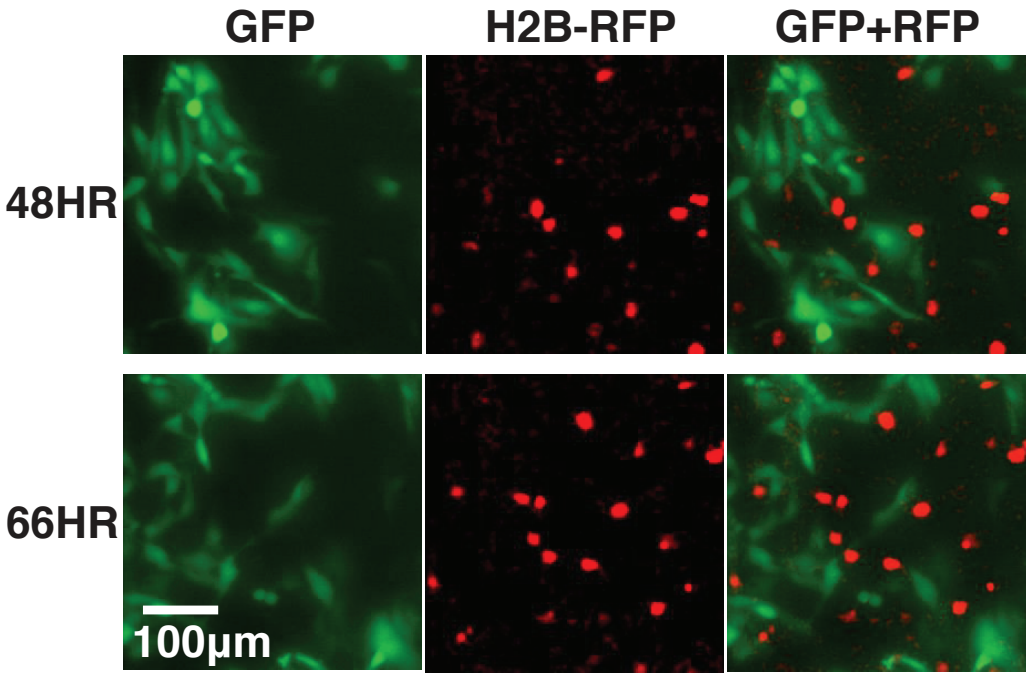

Figure 3.6: **No horizontal gene transfer in cancer without doxorubicin exposure.** Red fluorescence of donor (H2B-RFP, in nucleus) did not emerge in any of the 338 recipient green cells (GFP) as we observed by time-lapse microscopy at 48 and 68 hours.

Although horizontal gene transfer in cancer is a rare event, it become observable after 48 hours of 100nM doxorubicin exposure. In contrast, no transfer event was observed among 338 GFP cells traced in our control experiment without any doxorubicin exposure, as shown in Fig. 3.6.

3.4 Discussion

Our preliminary result demonstrated potential horizontal gene transfer in cancer occurred under doxorubicin exposure. The recipient cells (and other cells) eventually bursted in uniform 100nM doxorubicin within 70 hours. Therefore, the role of horizontal gene transfer in chemotherapy resistance is still unclear. Since mutations can be advantageous, deleterious, or neutral, it is possible that horizontal gene transfer might be advantageous, deleterious, or neutral as well. Then, pieces of DNA transferred to the recipient cells do not necessarily enhance the fitness of the recipient cells. However, the role of gene transfer in the diversification process of cancer should not be ignored.

We then ask, how did the genes actually transfer in our experiments? There are two possible ways that cancer cells can undergo horizontal gene transfer:

(i) Cell fusion: If two cells fuse, they would form a cell with two nuclei (Fig. 3.2 C). If two nuclei fuse, genomic hybridization may occur (Fig. 3.2D). However, in our experiments we did not observe cell fusion occurring before the emergence of a red nucleus in green cells.

(ii) Viral infection: Viruses are an important natural cargos of transferring genes between different species, facilitating genetic diversity and driving evolution [39]. Before our co-culture experiments, the histones of MDA-MB-231 cells were labeled using H2B-RFP lentiviral vectors. Viral vectors are a tool commonly used by molecular biologists to deliver genetic materials into cells, a process termed transduction. More specifically, these MDA-MB-231/H2B-RFP cells were infected by viruses carrying H2B-RFP sequences, so that these cells kept expressing H2B-RFP. Although usual virus infects a cell and multiple copies of the virus are build and leave the cell, the lentiviruses we used in our experiments are replication-defective for safety issues so that these virus are not able to replicate by lysing their host cells. For safety concerns, these genetic engineered lentiviral vectors (used in our experiments) are capable of

infecting their target cells and delivering their viral payload, but cannot continue the typical pathway that leads to cell lysis and death. Therefore, the emergence of red nuclei in green cells is less likely to be due to lysis of virus-infected H2B-RFP cells and re-infection of GFP cells.

While we temporarily set aside the open question "how do genes horizontally transfer", we may discuss: why horizontal gene transfer in cancer became observable if doxorubicin was supplied? Does doxorubicin make the cells more susceptible to gene transfer? It is possible that doxorubicin, which is mutagenic, switches off some "guardians" of the cells (such as P53) so that the cells would be more likely to accept foreign DNA. Perhaps doxorubicin killed some H2B-RFP cells and these dead cells released some viral vectors, or more complicated mechanisms beyond the scope of our work may be involved in horizontal gene transfer in cancer. Future work related to this topic is presented in the Chapter. 7.

Chapter 4

Multiple Myeloma: Accelerating the Emergence of Chemotherapy Resistance and the Role of Ancient Mutational Cold Spots

In this chapter, we demonstrate that the presence of an *in vitro* drug gradient coupled with cell motility and population fragmentation produces a strong Darwinian selective pressure that drives forward the rapid emergence of doxorubicin resistance in multiple myeloma (MM) cancer cells. The rapid emergence of drug resistance in MM cancer cells based on a drug gradient and metapopulation ecology is part of a general class of survival strategies.

RNA sequencing of the resistant cells was used to examine both (1) the emergence and location of de novo mutations (i.e. mutational hot spots), and (2) the role played by genes of the transcriptome which are never mutated (i.e. mutational cold spots). The analysis of the never mutated genes revealed that they belong to an important class of highly conserved and ancient genes essential to cellular function, while the

"highly mutated" regions mainly involve the regulation of chromatin organization, cell division and cellular defense mechanisms.

We thus propose that the mutational cold spots in addition to the hot spots play important roles in the emergence of doxorubicin resistance in MM cancer cells, and emphasize the non-mutational aspects to cancer progression and the emergence of resistance. Indeed, studying cold-spots could provide even more important targets in novel treatments than the mutated areas in terms of emergence of drug resistance, we show the cold spots contain many genes critical for cell survival. The presence of "never-mutated" genes indicates a possible programatic aspect rather than purely random genomic evolution.

4.1 Introduction

Multiple myeloma (MM), a hematologic cancer that develops in the bone marrow, is usually incurable because chemotherapy resistance emerges [40]. The emergence of resistance may be largely due to the fact that bone marrow represents a very complex environment, due to the spatial heterogeneity of the bone marrow structure and the non-uniform distributions of nutrient, oxygen, and drug (during chemotherapeutic treatment) [41].

Recent studies of the bone marrow represents an ideal ecology to be reproduced by microfluidic systems, with designed *in vitro* complex environments with glucose gradient or chemotherapy gradient [42]. Gradients have been used to study the phenotypic progression of cancer in complex environments [32, 34]; now we add the compartmentalization of small possibly clonal communities within the gradient. Just as rapid fixation of drug-resistant bacterial mutants in a metapopulation can occur in an environment with drug gradients and connected microhabitats[3, 43, 4], we now demonstrate that an ecologically-designed microenvironment, with drug gradients and

connected microhabitats, can drive the rapid emergence of resistance in MM. We then address a deeper question by transcriptome sequencing of the far more complex (than in bacteria) genomic mutation patterns in the evolved MM cancer cells: what is the role of both mutations and *non*-mutations in the evolved genomes of the resistant cells in driving drug resistance?

In Chapter 2, we analyzed the two-dimensional motions of metastatic breast cancer cells at the single cellular level within a drug gradient without any local population bottlenecks [34]. These experiments lasted for 72 hours (at most 3 generations) and there were no microhabitats within the culture region which entered the drug gradients, nor was any genomic analysis performed. Here we designed connected microhabitats (hexagonal arrays) in the cell culture region to mimic the porous bone marrow structure, creating a metapopulation within the drug gradient with local fixation possibilities and invasion of more fit mutants into higher toxicity environments [3], and then analyzed the genomic changes that emerged in such a short time.

The conventional view of the well-known emergence of drug resistance in cancer is that the initial stages are driven by mutations which are random and independent events [44]. In the conventional view, once a set of mutations occurs, selective pressure (i.e. chemotherapy for cancer) from the environment selects advantageous mutants out of this ensemble of mutations, with a background of neutral fitness passenger mutations carried along with the driver mutations which change fitness [45]. In the case of cancer cells under mutagenic stress, mutations are perhaps random but the frequency of the mutations is increased by the stress-induced mutagenesis, so that drugs used in chemotherapy perversely can play a crucial role in the acceleration of the evolution of drug resistance [46]. Here we chose genotoxic doxorubicin as a mutagen, and also use a strong spatial selective pressure created by chemotherapy gradients, and rapid fixation of mutations with the metapopulation to accelerate the evolution of drug resistance in cancer, unlike the conventional protocol of gradually

increasing in time the drug concentration (temporal drug gradients [47]). Clearly time-dependent gradients are also important in an *in vivo* setting, but that is beyond the scope of this work.

A critical part of this chapter is a detailed examination of mutations and non-mutations in the resistant cells. To be clear, we think there are two broad components of information dynamics in cancer evolution. One involves permanent changes in which genes are subject to gain or loss-of-function mutations. This is well established and the main focus of cancer research. The other component is the information in the human genome which is not mutated and even protected. The cancer cell potentially has access to all of this and can up-regulate or down-regulate any number of strategies used for survival and proliferation during embryogenesis, development, and normal adaptation to environmental stresses. The concept that a mutation is need to confer resistance is built into the Norton-Simon model which has dictated cancer therapy practice for 5 decades [48]. Certainly mutations play a general role in the evolution of drug resistance and so targeted therapy could require a mutational event to provide cancer cells with a strategy around the therapy. However, we also know that duplication of key genes is common. This is a well-known evolutionary event that allows asexually reproducing species to maximize their adaptability and overcome Mueller's ratchet [49]. Gene duplication can be one of the causes of up-regulation of proteins but is not necessary. We will examine this aspect also in this chapter.

4.2 Rapid emergence of drug resistance in a chemotherapy gradient metapopulation

The device, with drug gradients and microhabitats, were originally designed for bacteria (E. Coli.) [4, 50]. Considering the difference between cancer and bacteria, such

as cell size and motility (Table 4.1), we redesigned a version for cancer cells. The size of cancer cells is about 10 μm, 10 times greater than E. Coli. Multiple myeloma cells migrate at least 100 times slower than E. Coli. Therefore, the mammalian version is 100 μm in depth, comparing to 10 μm deep for bacterial version. Also, we chose the distance between neighboring microhabitats to be much shorter for mammalian version. The mammalian version is composed of two 1 mm wide parallel channels, continuously supplying nutrient at one side and drug plus nutrient at the other side.

Table 4.1: Physical parameters of cancer vs. bacteria

	Size	Motility	Slits Width	Chip Depth
E Coli.	1 μm	10 μm/sec[51]	100 nm	10 μm
Cancer	10 μm	10-100μm/hour[52]	5 μm	150 μm

Our device is composed of array of hexagons with small passageways connecting the six sides of the hexagons with adjacent ones (fabrication method is presented in Appendix B.1). The array is a 12mm by 2mm rectangular shape, connected with two parallel channels maintaining the boundary concentrations of drug by array of 5 μm slits (Fig. 2.3).

Our protocol (Appendix B.4) was to first inoculate cells into the device without a drug gradient and incubate the cells for 24 hours to ensure that the cells were alive and formed a uniform layer (Fig. 4.1C). Once this was achieved a drug gradient was put across the culture chamber by turning on two syringes containing growth media alone and growth media containing doxorubicin (Fig. 4.1D). The gradient became stable within 30 minutes and the drug concentration decreased approximately linearly from the high side to the zero side. While it is realistic in terms of clinical chemotherapy to first incubate the cells and then apply the drug gradient, a more realistic microecology would have had a distribution of gradients and time-varying gradients, but that is also beyond the scope of this work.

The emergence of doxorubicin resistance occurred on the time scale of days in "wild-type" parental MM with an high end doxorubicin concentration of 20 nM (x5

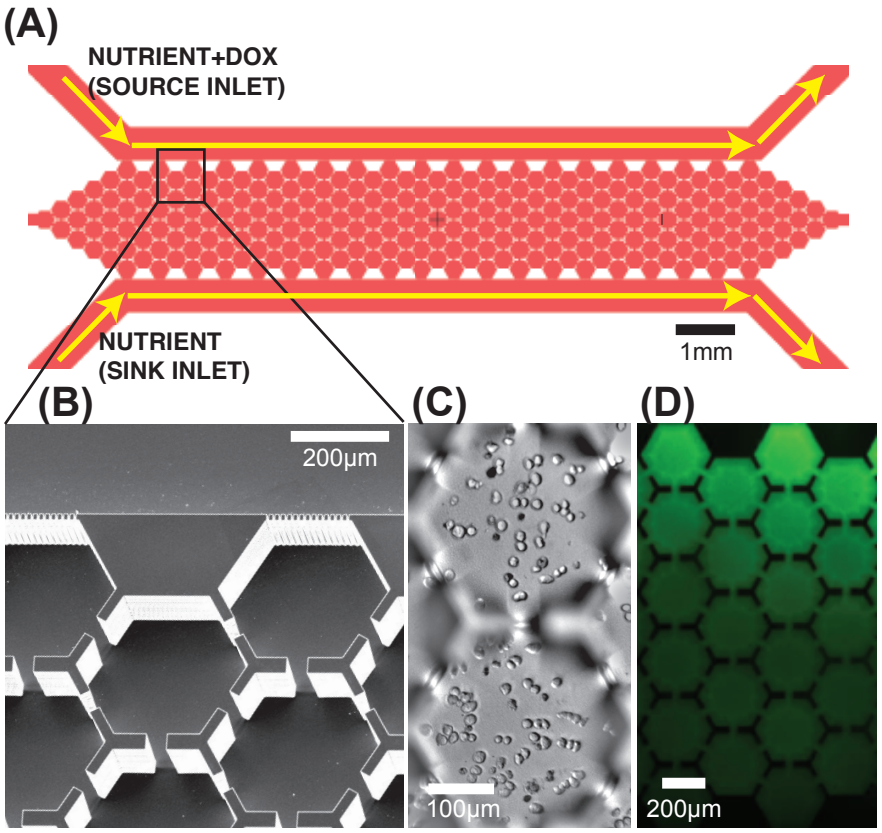

Figure 4.1: **Device layout and gradient characterization.** A. An overview of the entire microfluidic device, showing the flow of the nutrient streams and the nutrient+Doxorubicin (Dox) containing streams. The nutrient stream is growth medium, while the nutrient + Dox stream is growth medium + 20nM Dox. B. Scanning electron microscope (SEM) image of the area of the array outlined by the box in A. C. Image of MM cells in the device before imposing Dox gradient. D. Image of the expected Dox concentration using the dye fluorescein as a marker. Prior work with similar structure to create a gradient (but without the walls to create microhabitats) gives a linear gradient [34].

the IC50 under continuous exposure [53]) maintained in the top channel ("Dox+" in Fig. 4.2). In spite of the presence of doxorubicin, MM cells grew well and formed colonies initially near the nutrient channel ("Dox-" in Fig. 4.2). Near the "Dox+" channel, initially MM growth were inhibited for 3 days but resistant colonies ultimately appeared in a non-uniform manner across the gradient, as shown in Fig. 4.3.

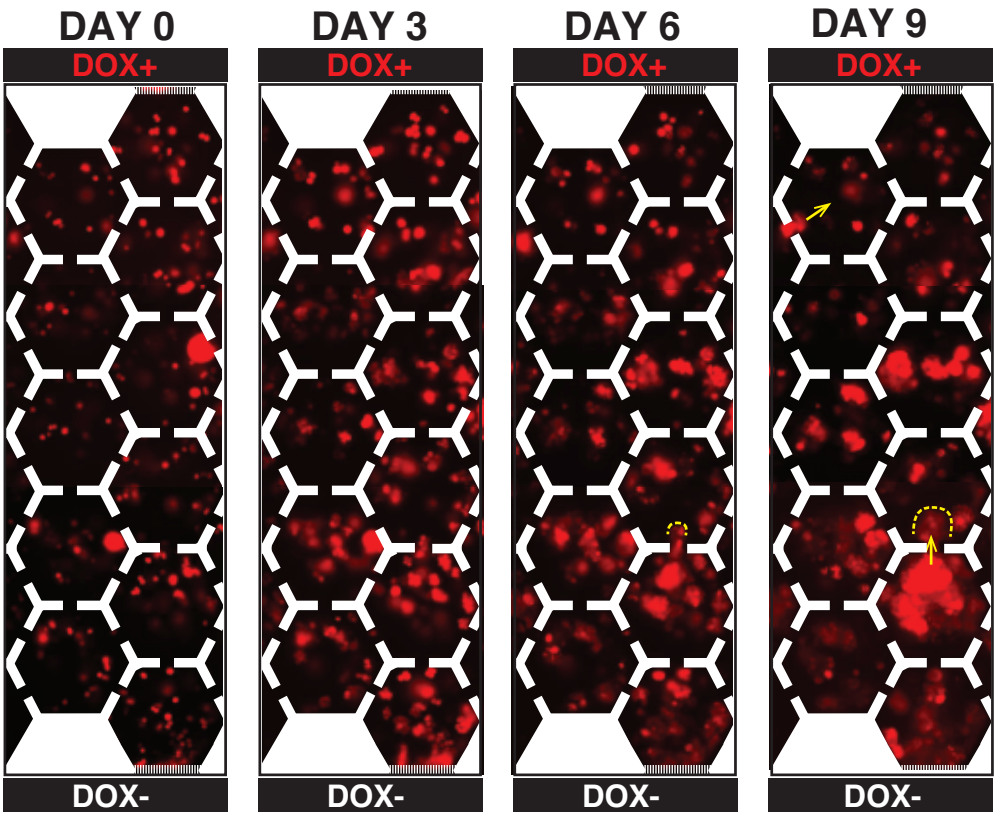

Figure 4.2: **Emergence of doxorubicin resistance of MM cells in a doxorubicin gradient.** Images of MM cells (8226/RFP) under a doxorubicin gradient (0-20nM/2mm) in time series. Doxorubicin diffuses from the top to the bottom. Yellow dotted lines: MM collectively migrated in Day 6 and 7 toward the doxorubicin channel ("Dox+").

The total increase in cell coverage during the experiments was only x4 (from 15% to 60%), indicating that in the absence of cell death only two generations of cells had passed before significant resistance had emerged. However, the increase in cell density was greatest at the mid-point of the gradient, where the doxorubicin concentration is still x2 the IC50, indicating the emergence of resistance across the gradient, and cell density proceeded towards the higher doxorubicin concentrations. Note that the overall population density only increases by a factor of x4 in within 9 days, which indicates that only 4 cell division cycles have occurred. Thus, the evolution of drug resistance in this experiment is relatively fast in terms of generation cycles.

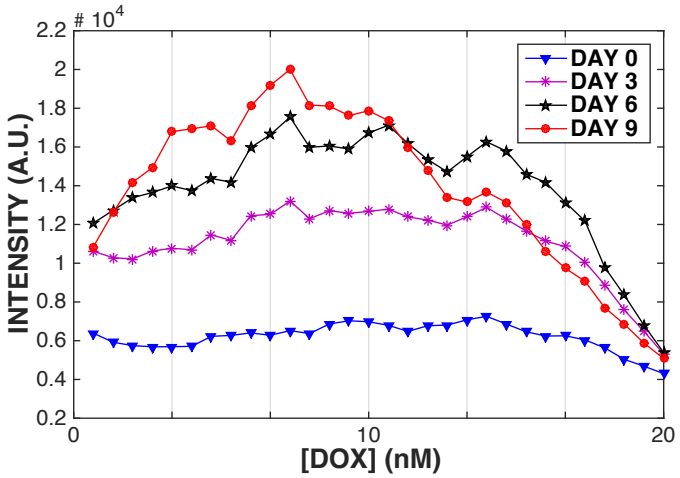

Figure 4.3: **MM vs. doxorubicin concentration vs. time in a doxorubicin gradient.** The gradient region is divided into 30 region of interest (ROI) and the mean pixel intensity over each ROI is measured by ImageJ. Each fluorescence intensity data point is the average over 3 gradient devices and then smoothed with a span of 3.

We performed two control experiments to demonstrate the necessity of a drug gradient for the emergence of resistant MM cells.

(1) We grew 10^6 cells in each tissue culture flask with 10nM of doxorubicin (replenished every 4 days). After 14 days, all the cells in three tissue culture flasks lost viability based on Trypan Blue staining, demonstrating that the emergence of drug resistance cannot be achieved by a conventional single-step of drug selection [47].

(2) To confirm that the doxorubicin gradient instead of extracellular matrix induced the doxorubicin resistance in MM in our microhabitats[54, 55], we pumped 10nM of doxorubicin at both side channels of our devices, so that the concentration of drug was uniform at 10nM throughout the microhabitat culture region, and compared the growth curves of MM with that in the same devices with doxorubicin gradient (0-20nM/2mm) (Fig. 4.4). The cells neither migrated nor grew after 3 days of uniform doxorubicin exposure in the devices. After 14 days, all cells in the devices (with or without gradients) were collected and the viability was measured by Trypan Blue staining. The fact that all cells in the uniform doxorubicin environment lost vi-

ability indicates the rapid emergence of doxorubicin resistance in MM only occurred in a gradient environment.

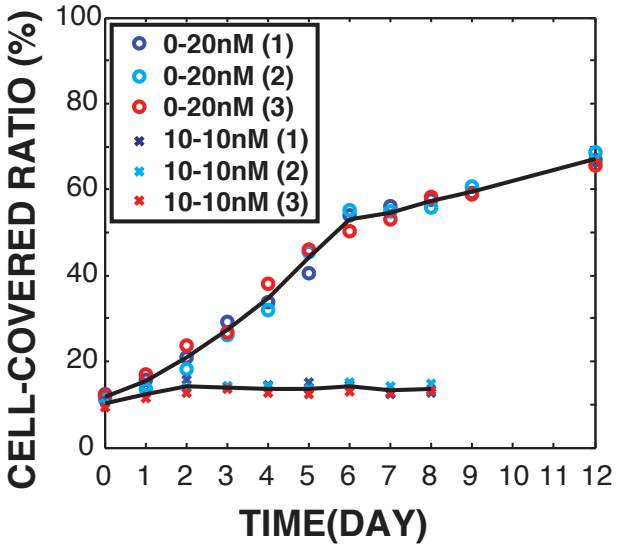

Figure 4.4: **Control experiments: drug gradients are essential for emergence of resistance.** Growth curves of MM in microfluidic devices with doxorubicin: uniform (10nM at both sides) vs. gradient (0-20nM/2mm) doxorubicin exposure. Circles: three devices of gradient (0-20nM/2mm) environment. Crosses: three devices of uniform (10-10nM) environment. Lines: mean of three devices.

Approximately 10^4 MM cells were harvested after 14 days from the device (named as Drug Resistant (DR) cells) and grown in a doxorubicin-free tissue culture flask for 1 week to expand the population size in the absence of stress. Then, the dose response was performed to characterize resistance of DR cells versus the wild type (the parental MM cells, WT) (Fig. 4.5) (cell collection and dose response methods, Appendix B.7). We found that the degree of cross-resistance (the IC_{50} of DR vs. WT) after 48 hours of doxorubicin exposure increased by 16-fold. This degree of cross-resistance requires 10 months to achieve by conventional protocols using step-wise increases of doxorubicin [53], indicating the rapid ability of the MM cells to adapt to mutagenic stresses in a complex microenvironment, of profound impact to MM mortality *in vivo*.

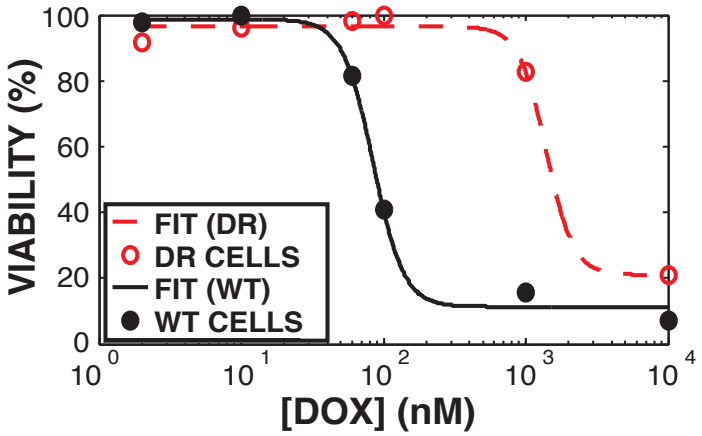

Figure 4.5: **Emergence of doxorubicin resistance in a doxorubicin gradient.** Doxorubicin dose response (48-hour exposure). Cells from drug gradient device (0-20nM/2mm for 14 days, named as DR, red) vs. parental MM cells (WT, black). Data fitting was based on Hill equation (Materials and Methods). The inhibitory concentration for 50% of control population (IC_{50}) of doxorubicin was increased by 16-fold.

Sampling MM cells from different regions within the drug gradient might unveil the degrees of resistance emerged along the gradient. Ideally, spatially resolved sequencing along the drug gradient would allow construction of the resistance phylogeny trajectory. At this point, we grouped the cells from the gradient for dose response characterization (Fig. 4.5) and for sequencing analyses so that we have to leave where the resistance evolves along the gradient and the true role of chemotaxis as an open question.

A common mechanism of drug resistance is via up regulation of a group of Multidrug Resistance (MDR) transporter proteins, which bind to ATP and pump drug molecules outside of cell membrane so that intracellular concentration of drug can be reduced. We characterized the expression level of MDR transporter of DR versus WT cells using Vybrant^{TM} Multidrug Resistance Assay (Life Technologies), as shown in Fig. 4.6.

The quantitative data of DR versus WT cells in MDR protein expression is shown in Fig. 4.6C. Since DR cells are dimmer than WT cells, DR cells accumulate less

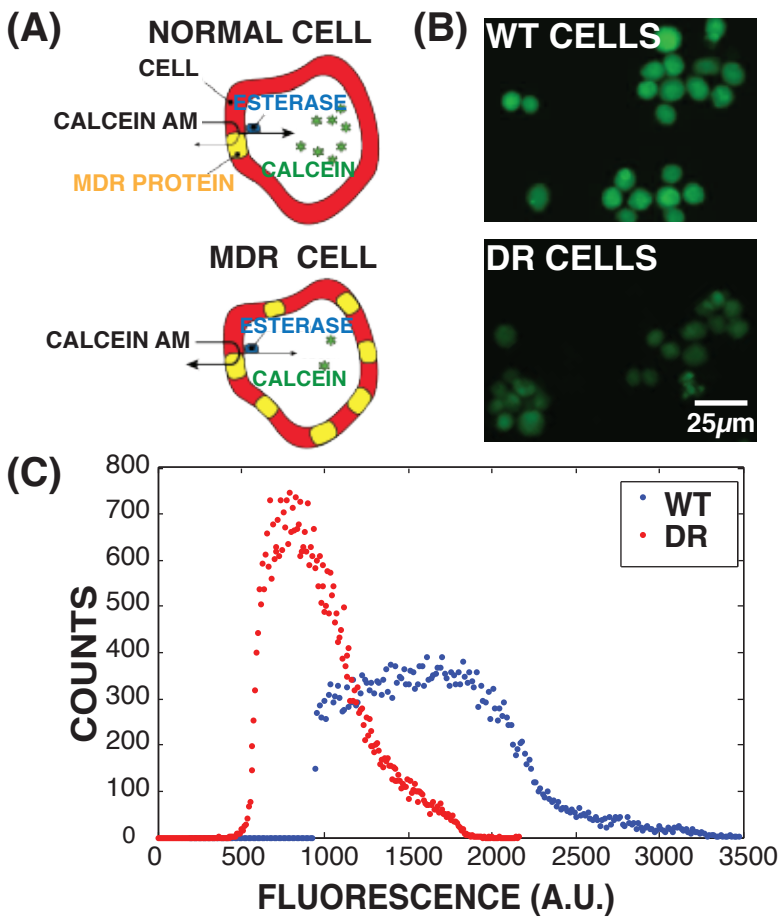

Figure 4.6: **Bioluminescent MDR assay shows the MDR proteins expression levels.** A. This assay utilizes the fluorogenic dye calcein AM as a substrate for efflux activity of MDR pumps. Calcein AM is non fluorescent dye that can rapidly penetrate the cell membrane. Once inside the cell, ester bonds are cleaved by endogenous esterase's, transforming calcein AM into fluorescent calcein retained in the cell. MDR cells expressing high levels of MDR proteins rapidly extrude non-fluorescent calcein AM from cell membrane, reducing accumulation of fluorescent calcein inside the cell. B. WT cells are brighter than DR cells based on MDR assay, indicating they expressed less MDR efflux pumps (qualitatively). C. Quantitative analysis of the bioluminescent MDR assay shows that the MDR proteins expression levels of most DR is higher than WT cells.

fluorescent calcein due to more MDR efflux pumps. Using the MDR assay, we learned that DR cells upregulated MDR efflux pumps and therefore demonstrate a resistance phenotype. In the next section, we will study the whole transcriptome of DR versus WT cells to explore deeper insights on the evolution of cancer resistance.

4.3 RNA sequencing analysis of resistant cells

We performed RNA sequencing analysis of WT and DR samples to identify the expressed mutations and differential expression levels of genes after the emergence of resistance. We sequenced 4 samples: 2 were samples came from evolution in the drug gradient (DR), 2 were not (WT), and each sample was composed of 10^4 cells collected from 3 microfluidic devices running simultaneously under the same condition (Appendix B.8). Although there is certainly a spatial dependence to the evolved genomes in the DR cells, in this preliminary analysis we grouped all the cells from the chip together. Basic statistics of 4 samples are shown in Table 4.2 and Table 4.3. Mapping, SNVs, and expression analyses were based on the protocol shown in Appendix C.2.

Table 4.2: Mapping statistics

Number of mapped reads	Sequencing 1	Sequencing 2
DR	50,292,847	93,016,838
WT	62,384,592	111,504,450

Table 4.3: Coverage

Number of covered bases	Sequencing 1	Sequencing 2
DR	337,174,818	479,156,993
WT	422,900,554	646,321,913

Investigation of the substitutions that occurred in the evolved DR cells was done by comparison of the mutations in the transcriptome of initial MM cells (WT) and the evolved resistant cancer MM cells (DR) to the human reference genome (Genome Reference Consortium GRCh37), this yielded the raw number of mutations within a given gene in both the WT and the DR cells (Table 4.4).

Table 4.4: Number of SNVs detected and percentage (Nonsynonymous/total)

Number of SNVs	Sequencing 1	Sequencing 2
DR	1238/5231 = 24%	3129/11882 = 26%
WT	2742/14333 = 19%	3107/15678 = 20%

Since the input WT cells are themselves cancer cells, there were coming into the evolution experiment with more than 5 thousands single nucleotide variants (SNVs) in each sample compared to GRCh37. DR SNVs which were not present in any of WT samples are called DR *de novo* substitutions for the purpose of this thesis. Fig. 4.7 shows the observed substitution rates vs. sequenced exon length. The observed mean DR *de novo* substitution rate, $< \mu >=2.0\times10^{-4}/bp$ may seem high, but this is the time integrated output of cancer cells under exposure to high concentrations of doxorubicin.

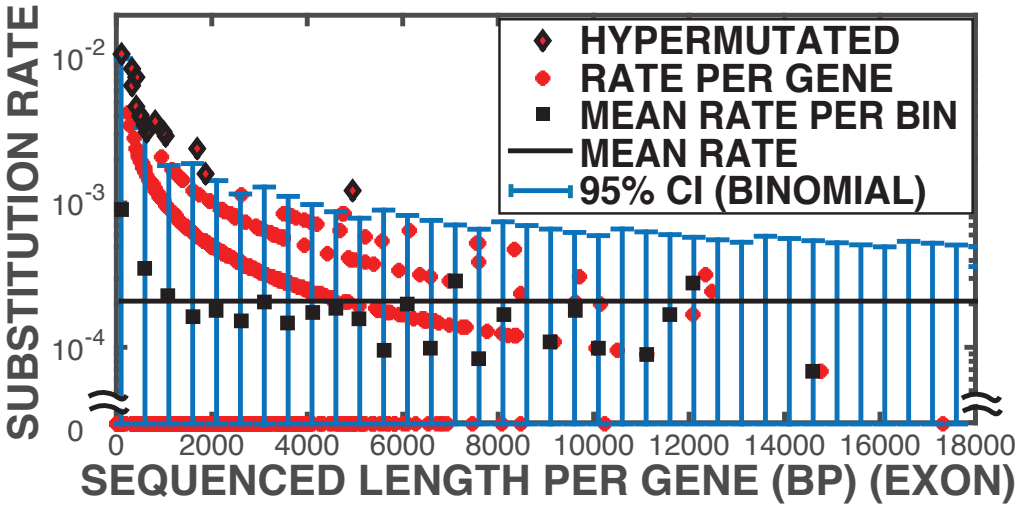

Figure 4.7: **Observed per base *de novo* substitution rate vs. sequenced exon length per gene (bp).** Red diamond: genes that were successfully sequenced for more than 80% of exon region. Black square: mean substitution rate within a 500bp window. Black line: mean substation rate $< \mu >=2.0\times10^{-4}$/bp. Blue error bars: 95% confidence intervals determined by binomial distribution (Appendix C.4). Black diamond with red center: hyper mutated genes determined by binomial distribution (Appendix C.5).

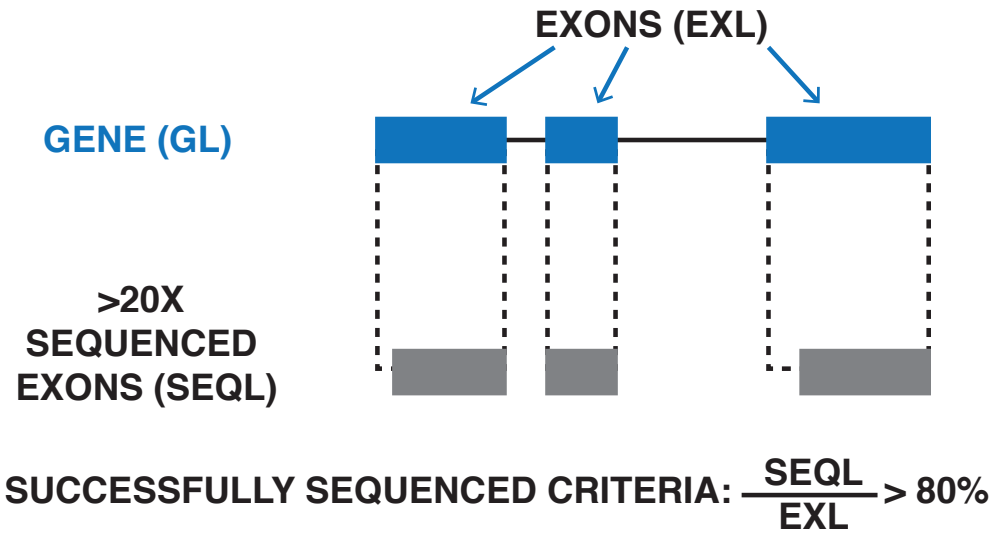

Figure 4.8: The criteria of successfully sequenced genes for mutation rate analyses: $> 80\%$ exon regions (bp) have been sequenced with a coverage depth > 20 reads.

Fig. 4.7 shows DR *de novo* substitution rates and mean substitution rate versus gene length for genes that were successfully sequenced for more than 80% of exon region. We follow the flow chart shown in Fig. 4.8. to determine successfully sequenced genes as 80% of exon regions were sequenced with 20 reads. The raw number of hits in a given gene, that is, the numbers of SNVs per gene, is widely applied as a way to find putative drivers of adaptation [56]. However, genes vary tremendously in length, ranging from hundreds to millions of bases in total (intron+exon) length as shown in Fig. 4.9, the histogram of the number of canonical human genes versus length. Of course, if substitutions are random then longer genes will show more mutations than shorter genes. This does not prove that they are hot spots for substitutions, but rather that they are simply longer. The SNV density is not a function of length in the random mutation model.

Since we did RNA sequencing rather than whole genome DNA sequencing we only looked at mutations in genes which were transcribed into expressed proteins (exomes). For each gene (i), we determine the "per base substitution rate" R_i as the number

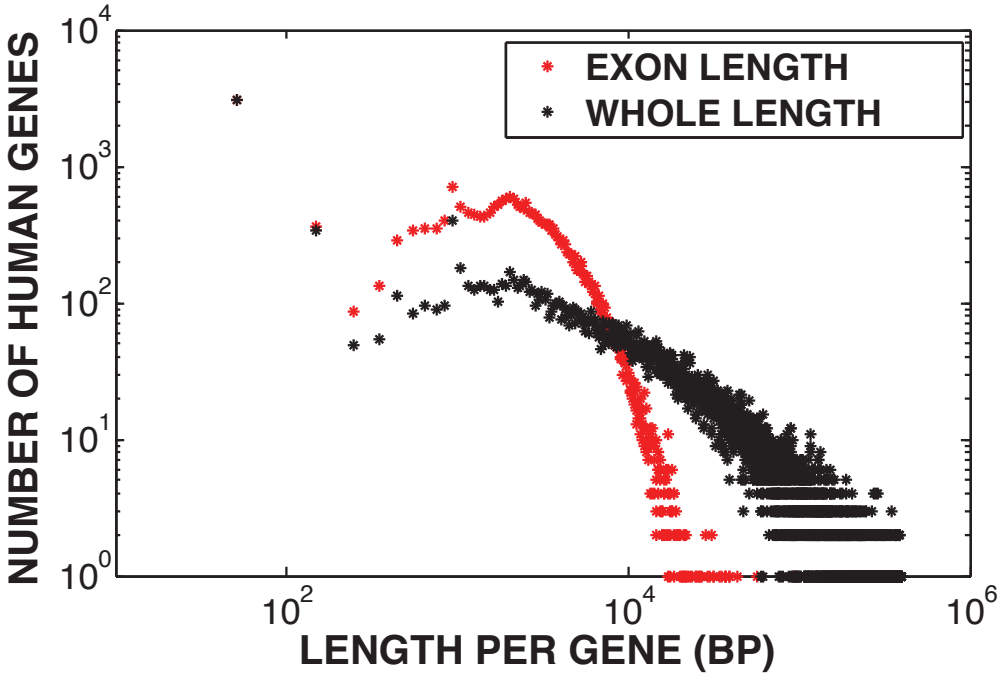

Figure 4.9: Histograms of numbers of canonical human genes (downloaded from UCSC Genome Browser) vs lengths. Red: exon length per gene; black: whole gene length.

of *de novo* substitutions M_i divided by the length in base pairs of the successfully sequenced exon region (covered with 20 reads) L_i, as shown in Fig. 4.10A. Since at most 3 substitutions were found in a gene, the binary nature of a substitution in a given gene yields the nested curves shown in Fig. 4.7. We thus set the per base gene substitution rate μ (substitutions/bp) by dividing by the length L of the gene to correct for the smaller target size of short genes. Likewise, if we saw 2 substitutions, then the rate is 2/L, etc. This is why you see a nested set (the substitution rates are quantized at the gene scale) and a set of ascending curves as one approaches the origin (because the 1/L effect). But note that as L decreases one has many more genes which are NOT mutated. Averaging over the number of genes in a given window size, in our case 500bp as shown in Fig. 4.7 gives a better representation of the rates of substitution versus length. This process flattens the nested curves into a single curve,

but there is still a tendency for more substitutions to occur in short genes compared to long genes, for resins discussed below.

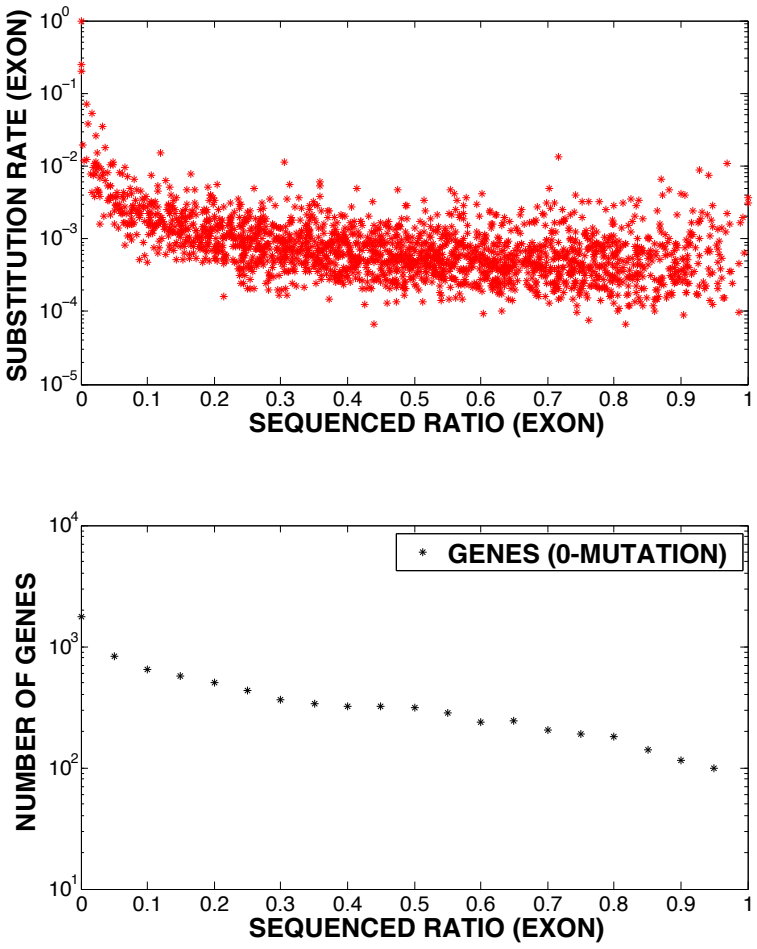

Figure 4.10: **Substitution rate and number of genes vs. successfully sequenced ratio (exon only).** A. Per base substitution rate (exon only) is defined as "number of substitutions" divided by "successfully sequenced length at exonic region". Successfully sequenced ratio is defended as "number of successfully sequenced bases at exonic region" divided by "canonical exon bases". B. Histogram of numbers of non-mutated genes vs. sequenced ratio (exon only).

Since the mean substitution density $< \mu >$ is low enough that even in the DR cells most genes do not have mutations, and hence the substitutions per gene are governed by Poisson statistics, we classified significantly substituted (hot) and not

substitute (cold) genes by calculating the mutation rate per base at the single gene level. If substitutions arise as a random Poisson process, the per base substitution rate averaged over of all genes should be independent of the gene length. However, most of the sequenced genes, have a per base substitution rate within 95% confidence intervals of $< \mu >$, determined by using error estimate of the mean substitution rate based on the binomial distribution (Appendix C.4). Genes with higher rates of mutations, using the Benjamini-Hochberg method [57], we call hyper-mutated genes. Our analysis identified 15 hyper-mutated genes in Table 4.5, such as HIST1H4H and TUBA1A, associated with nucleosome assembly, protein folding, and cell division. However, no clear pattern emerged in terms of function within the hyper-mutated genes, leading us to examine the never-mutated genes.

Table 4.5: Hyper-mutated genes (exon only)

Gene	SNVs	Bases	Sequenced bases	Mutation density	Probability*
HIST1H4H[1]	3	374	347	0.0086	1.1×10^{-6}
HIST1H2BF[1]	3	430	405	0.0074	2.0×10^{-6}
LOC101101776	3	816	816	0.0037	3.1×10^{-5}
PHB	4	1826	1703	0.0023	3.5×10^{-5}
HIST1H4B[1]	2	357	311	0.0064	4.3×10^{-5}
TUBA1A[3]	3	978	978	0.0031	6.1×10^{-5}
ARHGDIA[4]	3	1249	1040	0.0029	7.8×10^{-5}
AK022914	6	5104	4939	0.0012	1.0×10^{-4}
HIST1H2AM[1]	2	487	430	0.0047	1.1×10^{-4}
HIST1H2AC[1]	2	546	495	0.0040	1.7×10^{-4}
RPL36AL	2	577	503	0.0040	1.8×10^{-4}
PPP2CA[2,4]	1	96	93	0.011	1.8×10^{-4}
MRPS24	2	696	583	0.0034	2.7×10^{-4}
DPY30[1]	2	800	650	0.0031	3.8×10^{-4}
CALR[2,3]	3	1911	1860	0.0016	7.0×10^{-4}

*Probability to detect more mutations in this gene (p-value), calculation is presented in Appendix C.5.

[1]Biological process: chromatin organization, nucleosome assembly, telomere maintenance.

[2]Biological process: DNA replication, signal transduction, cell proliferation, cell growth, apoptotic process, DNA biosynthetic process.

[3]Biological process: protein folding, microtubule-based process, cell division.

[4]Biological process: cell adhesion, apoptotic process, protein localization.

4.4 Never-mutated genes and differential expression analysis

We also identified 163 successfully sequenced genes without any mutations in neither DR nor WT samples, "never mutated" genes, or cold genes. Among them, 13 genes are 4X up-regulated (Table 4.6) and 21 genes are 4X down-regulated (Table 4.7) in DR samples. These are presumably important genes which cannot be mutated because they play a key role in fitness of the cells. It has been suggested that these "never mutated" genes might actually be very ancient genes which represent a core functionality which cancer uses to maintain a basic fitness under high stress conditions, as presumably early lifeforms must have experienced [58, 59].

Table 4.6: Zero mutation, 4X **up-regulated** genes and their ages (exon only)

Gene	Bases	Sequenced bases	Age (10^6 years)	$Log_2(DR/WT)$
PRDX4[1]	921	801	3556.3	5.9
PGK1[2]	2733	2273	3556.3	2.0
NOB1	1775	1535	2269.5	5.9
CKS1B	1015	816	2269.5	4.4
TMEM167A	4721	3828	1530.3	2.7
COPZ1	2119	1727	1530.3	2.3
SEC61B	562	509	1369.0	3.0
CLIC1	1251	1157	1369.0	2.1
ID2	1364	1178	891.8	4.0
HIST1H2BC	438	403	891.8	2.9
SHFM1	498	433	839.4	3.0
PCP4	556	451	400.1	8.5
ART3	1216	1064	400.1	2.6

[1]Biological process: spermatogenesis, oxidation-reduction process.
[2]Biological process: gluconeogenesis, glycolysis, phosphorylation.

It is possible to estimate roughly the age of genes by assessing the relative positions of the genes' homologues in a phylogenetic tree (Appendix C.6). Such an analysis is shown in Fig. 4.11. We show there the histogram of calculated gene ages versus the human genome containing over 19,000 genes (solid black line) and the histogram of

Table 4.7: Zero mutation, 4X **down-regulated** genes and their ages

Gene	Bases	Sequenced bases	Age (10^6 years)	$Log_2(DR/WT)$
PSMC1[1]	1595	1531	3556.3	−3.7
ASB3[2]	1275	1094	3556.3	−3.5
RPS5[3]	741	728	3556.3	−3.6
RPLP0[3]	1304	1124	3556.3	−2.0
NDUFAB1	667	558	2535.8	−3.4
EEF1G	1538	1379	2269.5	−2.7
SUMO1	1527	1266	2269.5	−2.7
PFDN2	642	554	1530.3	−3.0
POLR2H	821	672	1530.3	−2.4
AHSA1	1537	1340	1530.3	−2.3
RBMX	2822	2338	1381.2	−2.4
OSTC	1152	1006	1369	−3.8
BRK1	1176	967	1369	−3.6
FAM3C	2542	2055	937.5	−2.8
XBP1	2172	1789	937.5	−2.5
COX6A1	572	517	937.5	−2.4
FBXO22	448	442	891.8	−2.2
TMSB4X	629	607	839.4	−3.7
COX7C	486	407	762.9	−3.9
NGRN	1760	1424	742.9	−2.8
CD74	1681	1443	400.1	−2.9

[1]Biological process: mitotic cell cycle, DNA damage response, apoptotic process.
[2]Biological process: protein ubiquitination, intracellular signal transduction.
[3]Biological process: translation.

"never mutated" genes from our experiment. We found that the zero-mutation genes we detected (4X change in expression) are older, on average, then all human genes, with the average age of 1.7 ± 1.0 billion years, compared to 19786 human genes with an average age of 1.3 ± 0.9 billion years. The error bars, quite large, and are simply a measure of the widths of the distributions and not a measure of the errors associated with this analysis, which are difficult to quantify at this stage. However, the large outlier of zero-mutation genes at 3.5 billion years age is statistically significant. These cold genes are presented in Table 4.6 and Table 4.7.

These genes seem to code for essential cellular functions: up-regulated PRDX4 is associated with spermatogenesis and oxidation-reduction process; up-regulated PGK1

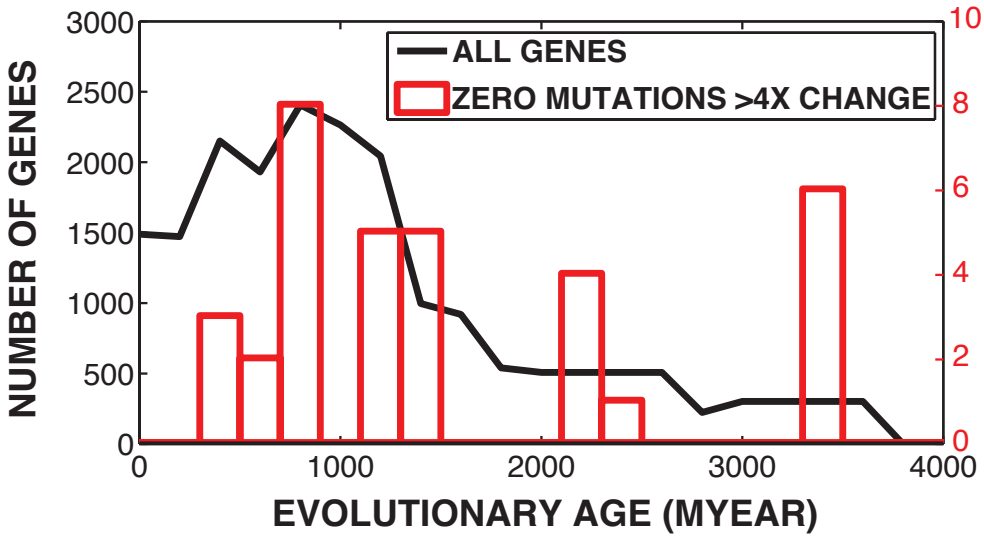

Figure 4.11: **Successfully sequenced genes without mutations in WT nor DR samples vs. evolutionary ages.** Red: histogram of numbers of genes vs. ages with a bin size of 200 MYEAR. MYEAR: 10^6 years. Black: histogram of all human genes with age information (19786 in total), shown as a control.

is associated with glycolysis and phosphorylation (Table 4.6); down-regulated PSMC1 is associated with cell cycle, DNA damage response, and apoptosis; down-regulated ASB3 is associated with protein ubiquitination; down-regulated RPS5 and RPLP0 are associated with translation. Although these zero-mutation ancient genes shared by DR and WT cells do not directly explain drug resistance in DR samples, they could provide insights on protected regions of the genome during malignancy transformation.

We finally address the expression levels of genes in DR vs. WT samples based on the abundance of RNA reads (fragments per kilomegabases, FPKM) mapped to genes (Appendix C.2). The log 2 ratio of DR to WT expression levels, $log_2(FPKM_{DR}/FPKM_{WT})$, describes how much the expression levels changed after exposure of doxorubicin gradient. In other words, the greater (or less) the log 2 ratio for a given gene, the greater it is up-regulated (or down-regulated) in DR samples.

Histograms of numbers of all sequenced genes (with FPKM 0.1 in both WT and DR samples) vs. log 2 ratio of expression levels is shown in Fig. 4.12.

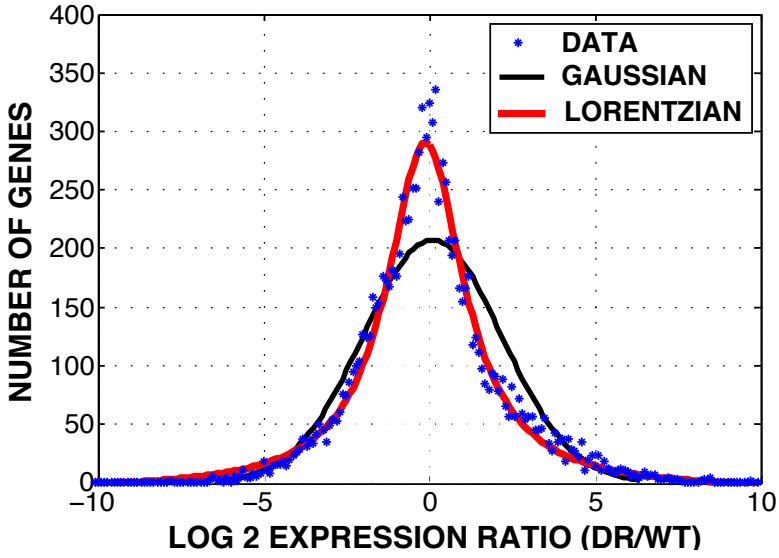

Figure 4.12: **Histograms of numbers of genes vs. log 2 ratio of DR to WT expression levels.** X-axis is the log2 ratio of DR expression abundance (FPKM) to WT expression abundance (FPKM). Blue: all sequenced genes with expression levels 0.1 in both WT and DR samples were taken into account (Dataset S2). Black: Gaussian model. Red: Lorentzian model.

The conventional way to analyze the gene expression data is to perform functional classification of gene sets [60] in search of genes that are significantly meaningful. For example, it is widely accepted that drug efflux pumps play an important role in reducing intracellular drug concentration and elevation of the drug resistance if they are up-regulated[61]. As we expected, we observed up-regulation of 3 drug efflux pumps, including ABCA13, ABCB11, ABCC3, greater than 4-fold in DR cells vs. WT cells (Dataset S2). Since these up-regulations are drug efflux pumps are commonly seen, we can question if this is purely random process driven by natural selection of a programmatic response which has been selected as part of the way that cells deal with drug toxicity.

A common mistake is to assume that a normal distribution of differential expressions would also yield simple Gaussian (normal) statistics. However, it has been pointed out by Brody et al [62] that a distribution of the ratio x/y of two normally distributed random variables is not necessarily Gaussian but rather a Lorentzian. The histogram shown in Fig. 4.12 does indeed fit a Lorentzian distribution much better than a Gaussian distribution. This implies that what appear to be outliers in the distribution are not in fact outliers but artifacts of the analysis, making comments about particular genes difficult. The mean of the distribution is however statistical significant. Since there is a shift of the mean of the Lorentzian curve to the left of the origin (Fig. 4.12), this may be a result of DR cancer cells suppressing some normal cell functions, but it is difficult to proceed further.

4.5 Discussion and summary

We observed that in a chemotherapy gradient landscape resistance of MM cells to doxorubicin can emerge rapidly, as we expected from previous bacterial work on antibiotic resistance emergence [4]. We show that cold genes are more protected as many evolutionary conserved genes [63]. We found that genes associated with nucleosome assembly and protein folding tend to mutate rapidly, while ancient genes associated with spermatogenesis, oxidation-reduction, and glycolysis are possibly protected and abnormally up-regulated on demand of acquired drug resistance. The trade-offs may be associated with energy and time limitation in harsh environment [64] and may be a strategy of cancer cells to evolve rapidly.

Since longer proteins have more surface area and more connections, it has been suggested that they encode more essential cellular functions than shorter proteins across various species [65]. Also, ancient genes have shown to evolve more slowly, and hence are cold, and express more "core" functional proteins compared with young genes [65, 66]. As shown in Fig. 4.11 and Fig. 4.12, we observed the selection for the abnormally regulated ancient genes with slow evolution rate in emerged resistant cancer. Our sequencing result of emergence of resistant cancer address the integration on gene length, evolutionary rates, functional essentiality, and evolutionary age; these properties have occurred in other species for guiding the animal body plans [67].

The adaptation to chemotherapy does not necessarily involve mutations - up-regulation of normal cellular defense mechanisms may be sufficient. The failure of a central-limit approach to the distribution of differential expression levels lies beyond the scope of this work. However, we can speculate that since there are thousands of pathways associated with chemotherapy resistance, cancer cells can simply activate selected pathways and increase expression levels of genes associated with those needed pathways to enhance their survival. Selectivity rather than random events could lead to failure of the central limit Gaussian distribution. Other than looking for new

pathways or validation of pre-existing pathways of drug resistance, we suggest that the quantitative and physical dynamic of how cells regulate the expression levels is equally important.

An important question that we cannot answer here is: were the *de novo* mutations generated spontaneously or induced by stress? It is experimentally challenging to prove the existence of stress-induced mutagenesis, via up-regulation of error-prone DNA polymerases or repressing DNA repair enzymes, because *de novo* mutation and selection usually come together [46]. However, we observed up-regulation of POLDIP2 of DR cells in our experiments. POLDIP2 is known to support DNA polymerase λ in translesion synthesis (TLS), which often has low fidelity (high propensity to insert wrong bases) on undamaged templates relative to regular polymerases and may induce *de novo* mutations [46, 68]. This error-prone recovery also protects DR cells from oxidative damage caused by doxorubicin [46, 69].

In this chapter, we have shown that in an array of interconnected microhabitats with an applied drug gradient, MM can develop extraordinarily rapid resistance to doxorubicin. We have shown that the mutational pattern of the resistant cells is quite diverse, with genes that show high mutation rates and genes that show very low, to no, mutations. It may seem strange to suggest, as we have here, that non-mutated genes may be critical targets for chemotherapy, we argue that these non-mutated genes may be the most fundamental ones for preservation of cancer cell fitness. There are two broad components of information dynamics in cancer evolution. One involves permanent changes in which genes are subject to gain or loss-of-function mutations. This is well established and the main focus of cancer research. The other component is the information in the human genome and preservation of that content. The cancer cell potentially has access to all of this and can up-regulate or down-regulate any number of strategies used for survival and proliferation during embryogenesis, development, and normal adaptation to environmental stresses.

Another question is the role that cancer plays in development [67] and the transition from unicellular to multi-cellular behavior, and the role that cancer has played as an evolutionary variable [70]. That is, since ancient genes seem to be protected from substitution perhaps cancer represents a return to unicellularity which are represented by these crucial and ancient genes, with cancer allowing substitutions in or abandoning higher level genes associated with multicellular cooperation [71]. Clearly, with our limited data set in this chapter we cannot address this question in a significant way, but we hope we can point the way to different ways of viewing how cancer has influenced the process of development and its deep origins.

Chapter 5

Friends or Foes? Game of Multiple Myeloma and Stromal Cells in Chemotherapy Gradients

Preventing relapse after an initial treatment is the major challenge of effective therapy in cancer. Within the tumor, stromal cells play an important role in cancer progression and emergence of drug resistance. During cancer treatment, the fitness of cancer cells can be enhanced by stromal cells because their molecular signaling interaction delays the drug-induced apoptosis of cancer cells. On the other hand, competition among cancer and stromal cells for space or resources should not be ignored.

In this chapter, we explore the population dynamics of multiple myeloma versus bone marrow stromal cells by using the same engineered micro environments as shown in Chapter 4, with a stable drug gradient and connected micro-habitats. Since evolutionary game theory is a quantitative way to capture the frequency-dependent nature of interactive populations, we use evolutionary game theory to model the populations in such engineered micro environments with the gradients of payoffs and successfully

predicts the future densities of multiple myeloma and stromal cells. We will discuss the possible clinical use of such analysis for predicting cancer progression.

5.1 Introduction

5.1.1 Players: cancer and stroma cells

Emergence of therapy resistance is inevitable in multiple types of cancer and significantly affects survival of cancer patients [72]. The tumor microenvironment can influence therapy efficacy because it is not merely composed of cancer cells but also stromal cells, a key player in cancer growth and progression [73, 55, 74]. During initial treatment, stromal cells suppress the apoptosis signal of cancer cells and further prolong the survival of cancer cells [75, 76]. As with many cancers, multiple myeloma, a cancer of plasma cells in the bone marrow, acquires therapy resistance by communicating with the stromal cells [7, 8]. The key signaling pathways in cancer-stroma communications (i.e. interleukin 6, IL-6, and stromal cell-derived factor 1, SDF1) have been extensively studied. However, it is challenging to extrapolate their biomolecular network to the resulting population dynamics of cancer and stromal cells. Therefore, we propose to use evolutionary game theory to interpret the interactions between cancer and stromal cells [5].

5.1.2 Evolutionary game theory

Evolutionary game theory has been used for modeling interacting populations in various biological networks[77]. In the evolutionary game theory, the fitness depends on population composition of various strategies or phenotypes. For a two-player game

between well-mixed player α and player β, the payoff matrix is given by

$$\begin{array}{c} \\ \alpha \\ \beta \end{array} \begin{array}{c} \begin{array}{cc} \alpha & \beta \end{array} \\ \begin{pmatrix} A & B \\ C & D \end{pmatrix} \end{array} \tag{5.1}$$

When a player α encounters a player α, it receives payoff "A". A player α versus a player β receives payoff "B" while the β receives payoff "C" from the α. A player β versus a player β receives the payoff "D". When we consider the absolute population of each type of players (α and β), then the population rate equations can be written as:

$$\frac{d\alpha}{dt} = (Ap_\alpha + Bp_\beta)\alpha \tag{5.2}$$

$$\frac{d\beta}{dt} = (Cp_\alpha + Dp_\beta)\beta \tag{5.3}$$

where population fractions $p_\alpha = \alpha/(\alpha+\beta)$ and $p_\beta = \beta/(\alpha+\beta)$, fitness of each player are $f\alpha = Ap_\alpha + Bp_\beta$ and $f_\beta = Cp_\alpha + Dp_\beta$. If A>C and B>D, player α dominates player β. Likewise, if A<C and B<D, player β dominates player α. This is a classic example of frequency-dependent selection. A coordination game occurs if A>C and B<D, then both α and β are stable. In a system with more α, it will keep being dominated by α. If currently there are more β, there will be more β. More complex dynamics occur if A<C and B>D, leading to a coexistence between the two players. In this case, a population with more α will then become dominated by β, and a population with more β will then become dominated by α ("Hawk-Dove game"[78]).

5.1.3 Evolutionary game theory and cancer

Evolutionary game theoretical models have been implemented on the interaction of cancer and other cells in various stages of cancer progression. Dingli et al have explored an evolutionary game between multiple myeloma, osteoclasts, and osteoblasts,

discussing disease progression and outcome of treatment[79]. Basanta et al have used evolutionary game to model the interaction and transformation of different stages of glioblastoma (such as glycolysis and invasive phenotypes) and predicted the stages of glioblastoma[80]. Flach et al have studied the role of fibroblasts in melanoma growth and drug resistance from a game theoretical point of vie [81]. However, it is very challenging to assess cancer and non-cancer populations versus time with high temporal resolution in clinical data. Because of the challenge of fitting experimental data, current game theoretical approach is limited to tuning parameters and discussing various scenarios in cancer progression. Even using *in vitro* co-culture experiments in tissue culture flasks, there is no information of complex heterogeneity in tumor microenvironment.

The tumor microenvironment highly influences the sensitivity of cancer cells to chemotherapy treatment. In a solid tumor, the drug diffuses into tumor core from the blood vessels. However, drug concentration drops significantly within hundreds of microns away from the blood vessels because of (i) diffusion barriers of closely packed cells, (ii) uptake of cells near the vessels, (iii) decreased activity of drug (such as doxorubicin) due to hypoxia, (iv) dissociation of drug in acidic tumor core[82, 13]. The relapse usually occurs when cancer cells in the tumor core suffer less dosage of drug, survive, and gradually form a tumor again.

On the other hand, various cells such as tumor cells, macrophages, or stromal cells form highly interactive micro-colonies[83]. In different conditions, the stroma can provide tumor-suppressing and tumor-promoting environments and influence cancer development and progression[83]. Combining with non-uniform distribution of drug within a tumor under treatment, one may ask whether the spatial drug distribution affects the role of stromal cells on cancer survival or proliferation. Therefore, we propose to use microfluidic technology to mimic tumor microenvironment with drug gradient, and probe the dynamics of cancer and stromal cells.

Microfluidics have been used to create versatile functions for studying various microorganisms. Microfluidics can create micro-fabricated landscapes, concentration gradients, or dynamic switching of different chemicals[84, 32, 34, 85]. Therefore, it is possible to reconstruct a heterogeneous microenvironment to asses the interactions such as competition or cooperation among cells. For example, a race has been held for prostate cancer cells to climb up micro-skyscrapers, characterizing the invasiveness of different cells[84]. The cooperation of cancer cells has been observed while the cells taking turns to lead the collective invasion through a glucose gradient across a collagen matrix[32]. Since invasion through an extracellular matrix has a metabolic cost, cancer cells intend to migrate toward a glucose abundant region with a higher fitness and reduce the total cost via exchanging leading positions.

Likewise, a drug gradient also provides a fitness gradient for cancer cells and causes a build up of a population gradient with time. Following by a population gradient, local competition for space and metabolic resources such as glucose or oxygen may drive the cancer cells to migrate toward the drug source, triggering the emergence of drug resistance[34]. In an engineered microenvironment with a chemotherapy gradient and microhabitats, we expect to capture the complex non-linear dynamics of multiple myeloma (MM) and stromal (ST) cells.

5.2 Results

5.2.1 Co-culture experiments

In the following experiments, we work with multiple myeloma (MM) and bone marrow stromal cells (ST) since bone marrow cancer is incurable and the biomolecular signaling network between MM and ST is already known[86, 7]. The MM cells (8226) are labeled with red fluorescent protein and ST cells (HS-5) are labeled with green fluorescent protein, a courtesy from Robert Gatenby Laboratory at Moffitt Cancer Center (Appendix B.2). We characterized their dose response (Appendix B.7) of doxorubicin, a chemotherapeutic agent which intercalates DNA and produces oxidative stress[61], prior the co-culture experiments. We found that MM is more sensitive to doxorubicin than ST, as shown in Fig. 5.1.

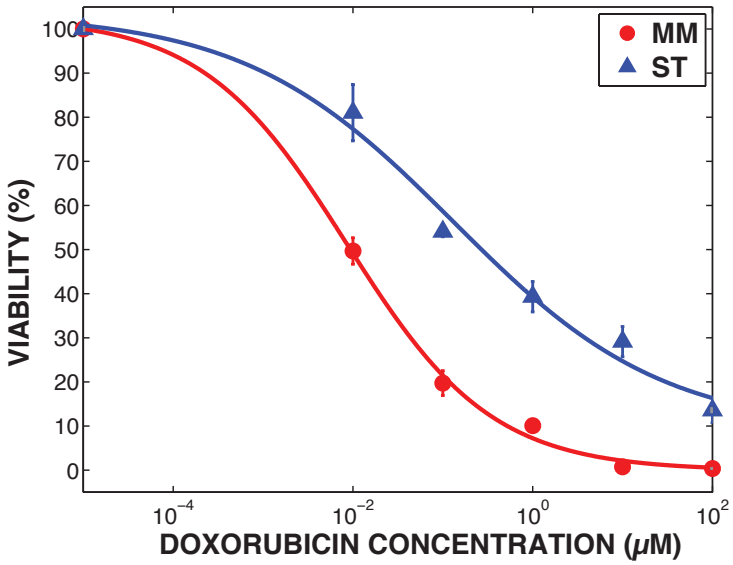

Figure 5.1: **Doxorubicin dose response (24-hour exposure) of MM (red) vs. ST (blue).** Error bars indicate standard deviation of 3 replicates.

We co-culture MM and ST in the microfluidic device with microhabitats and a linear gradient of doxorubicin (Fig. 4.1) for 2 weeks. The device is described in

Chapter 4. Cell loading and image acquisition methods are shown in Appendix B.4 and Appendix B.5, respectively. A representative image is shown in Fig. 5.2, in which MM and ST cells form 3D cluster near the nutrient-rich and drug-free channel within 6 days.

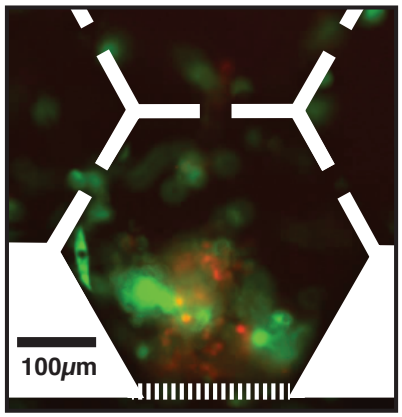

Figure 5.2: **MM and ST in a microhabitat** Image of cells in a microhabitat near the doxorubicin-free channel after applying 6 days of doxorubicin gradient (0-2μ M/2mm). Red: MM cells (8226/RFP), green: ST cells (HS-5/GFP).

First, we found that the MM grew only with the existence of ST; MM growth was not observed in the same environment (0-200nM/2mm) without any ST cells. The fact that MM show no growth without ST in the same strength of drug gradient is consistent with the known mechanism of stroma-mediated drug resistance[8].

Then, we performed the same drug gradient experiments with various initial population ratio of MM and ST (MM:ST) including 1:3, 4:1, and 1:0. The growth curves of both cells in the entire devices MM-rich (MM:ST=4:1) and ST-rich (MM:ST=1:3) are shown in Fig. 5.3.

We observed the following trends by looking at the cell densities every time in the entire devices with a drug gradient:

(1) ST cells are less sensitive to drug than MM cells.

(2) The MM do not survive for 5 days without ST cells in the same treatment.

(3) The initial ratio of MM versus ST affects the fate of MM cells: MM cells thrive if initially there were more MM than ST, but outcompete by ST cells if initially there were more ST than MM. The fact that a small population of ST cells may desensitize MM to drug, is consistent with previous discovery of stroma-mediated drug resistance [8] but competition between MM and ST should also be considered.

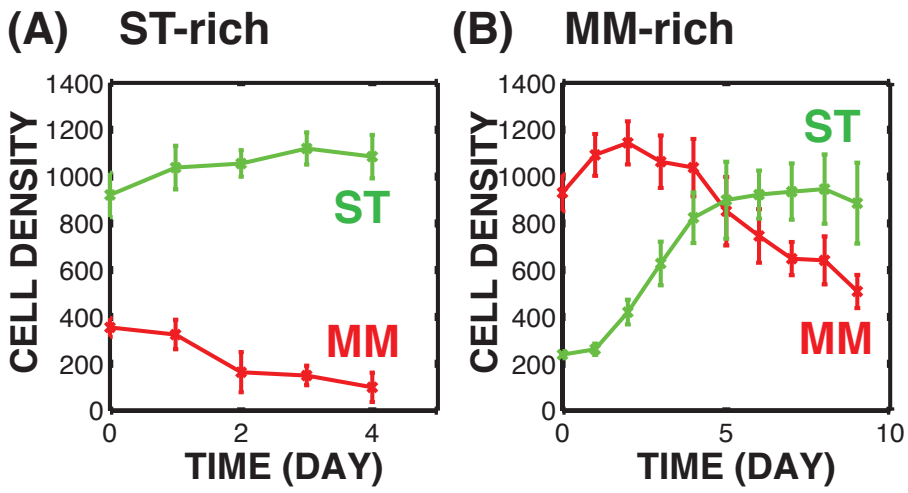

Figure 5.3: **Total MM or ST population density (number of cells/4mm^2) in the entire gradient device vs. time. MM and ST are co-cultured under a doxorubicin gradient from 0 to 200nM across 2mm.** A. ST-rich data with 5 replicates. Green: ST, orange: MM. B. MM-rich data with 3 replicates. Dark green: ST, dark red: MM. Error bars indicate standard deviation of the replicates.

5.2.2 Temporal dynamics

An alternative way to demonstrate the growth curves of the interacting populations of MM and ST from Fig. 5.3 is a phase portrait, in which the x-axis shows the population densities of MM, and the y-axis shows the population densities of ST. Then, population dynamics of the two co-culture experiments in the entire drug gradient, can be shown in a single Fig. 5.4. Given that we observed the fitness of

each cell type depends on initial population ratio, evolutionary game theory is an ideal model to describe the dynamics of this co-culture system.

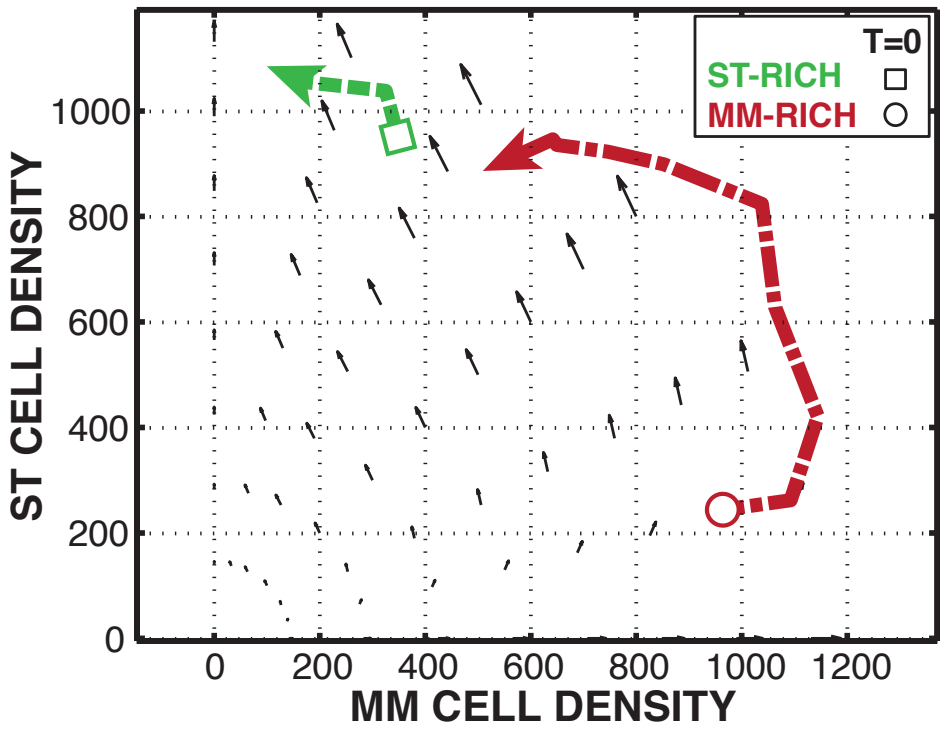

Figure 5.4: **Phase portrait of total MM and ST population density (number of cells/4mm^2) in the entire cell region vs. time. MM and ST are co-cultured under a doxorubicin gradient from 0 to 200nM across 2mm.** Green: ST-rich data. Bold green arrow shows the average over 5 ST-rich replicate experiments. Red: MM-rich data. Bold red arrow shows the average over 3 MM-rich replicate experiments. The gray arrows indicate the fitness determined by the experiments (the slopes of semi-log growth curves in Figure 5.3).

We first treat the system as a well-mixed populations and seek for parameters of a spatial-independent evolutionary game model. Here, we ignore the fact that there is a drug gradient. Therefore, the absolute populations MM or ST can be described by the ordinary differential equations

$$\frac{dMM}{dt} = (Ap_{MM} + Bp_{ST})MM \tag{5.4}$$

$$\frac{dST}{dt} = (Cp_{MM} + Dp_{ST})ST \tag{5.5}$$

where population fractions $p_{MM} = MM/(MM + ST)$ and $p_{ST} = ST/(MM + ST)$. If a MM cell encounters a MM cell, it receives a payoff A; a MM cell versus a ST cell receives a payoff B. A ST cell versus a MM cell receives a payoff C; a ST cell versus a ST cell receives a payoff D. From Fig. 5.4, we can see the system favors ST and if initially MM is much greater than ST, there exists a counterclockwise motion toward ST axis. Therefore, physical intuition tells us that A<C and B<D. By fitting the growth curves of each cell type with various initial population fractions [87, 88], we can find the payoffs A, B, C, and D (detailed in Appendix C.8). The quivers in Fig. 5.4 indicate the fitness as a function of population fractions and payoff matrix trained from our experiments ($f_{MM} = Ap_{MM} + Bp_{ST}$ and $f_{ST} = Cp_{MM} + Dp_{ST}$). Each quiver is a vector of (f_{MM},f_{ST}) determined by each position (MM,ST) in Fig. 5.4.

5.2.3 Spatial and temporal dynamics

We now address the spatial distribution of MM and ST in a drug gradient in time series. An example of initial MM-rich experiment is shown in Fig. 5.5. Surprisingly, after day 6, there were even more MM in the regions with higher drug concentration than that with lower drug concentration (Fig. 5.5). Quantitative population landscapes for ST-rich and MM-rich experiments are shown in Fig. 5.6 A and B. There are two possible mechanisms that MM cells can show survival at levels of a drug which should inhibit growth: (1) stroma-mediated drug resistance provides protection (but not permanent) for drug-induced apoptosis [55], (2) competition between ST and MM may be a significant factor for MM fitness. In all, the data suggests that ST can be friends or foes of MM cells under various population compositions and drug concentrations.

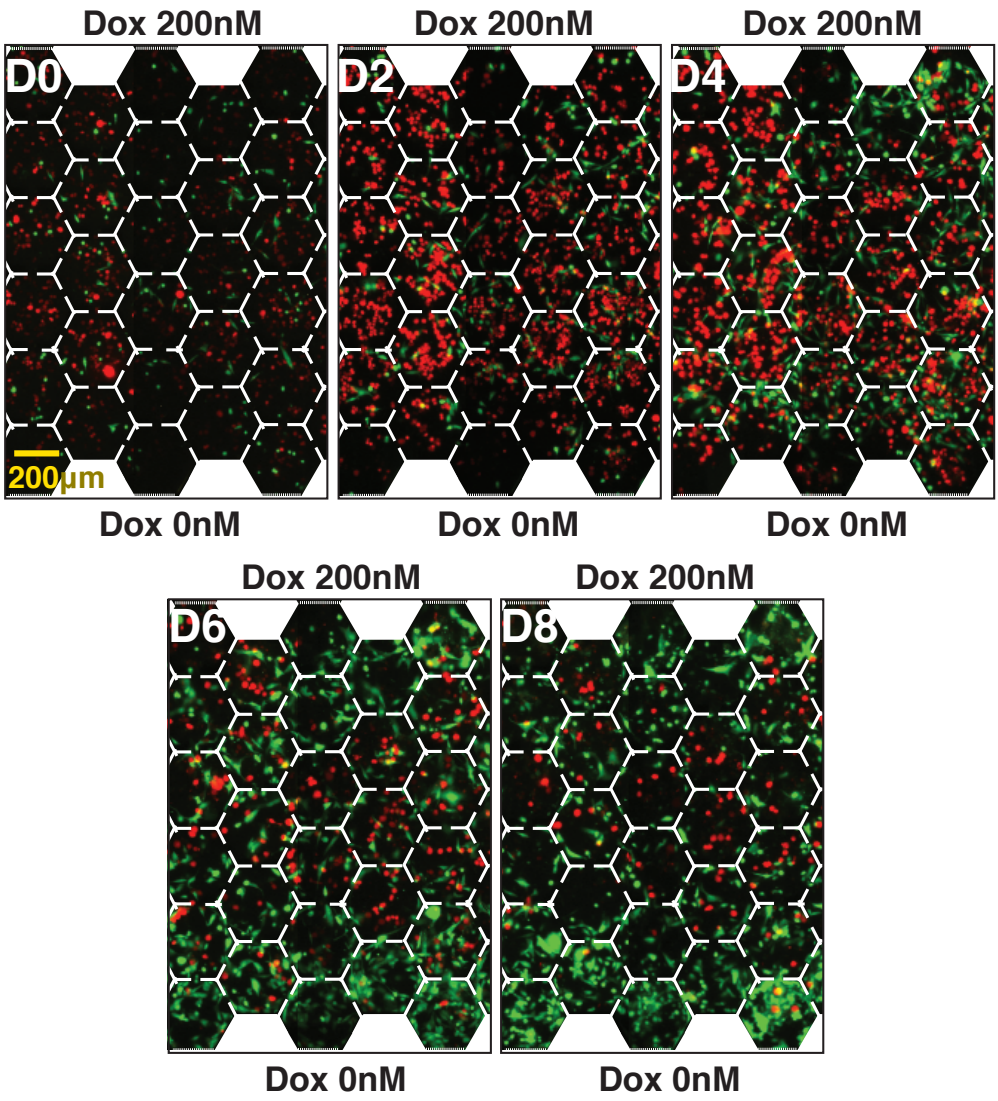

Figure 5.5: **MM and ST co-culture (MM-rich) under a doxorubicin gradient from 0 to 200nM across 2mm. (Day 0 to Day 8)** Red: MM cells (8226/RFP). Green: stromal cells (HS-5/GFP). Top: doxorubicin concentration is 200nM; bottom: doxorubicin concentration is 0nM.

5.2.4 Effect of drug gradient on fitness of MM and ST

Since doxorubicin causes DNA damage and inhibits cell proliferation [61], it further affects the fitness of all cell types. A spatially-resolved game theoretical model of the system can be achieved by assuming the payoff as a function of drug concentration. In the device with a linear drug gradient, we can simplify the system and assume the

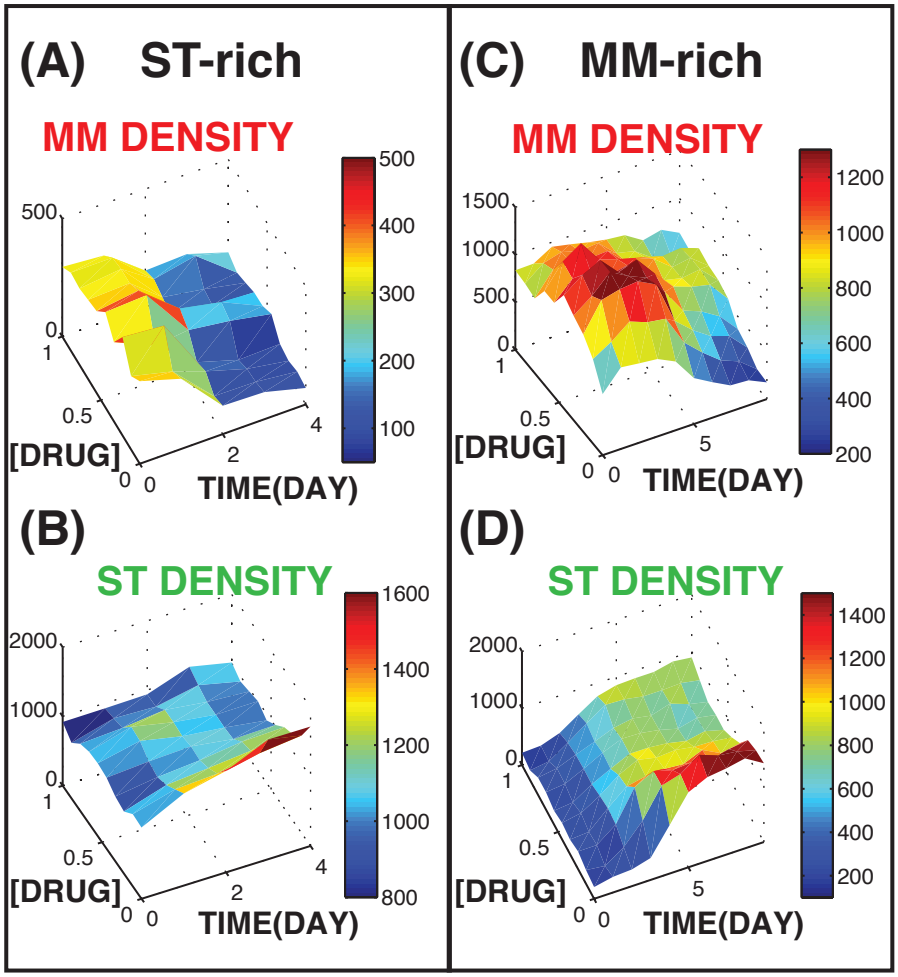

Figure 5.6: **MM and ST vs. space and time (experiments).** A-B. MM vs. ST populations within the drug gradient in ST-rich condition. C-D. MM versus ST populations within the drug gradient in MM-rich condition. Color bar indicates population density (unit: number of cells/4mm^2.)

payoff as a 1D function of space (x-direction, along the drug gradient in cell region). Here, we also assume the payoff coefficients (A, B, C, D) at a given location are fixed with time for simplification.

We use finite difference time domain (FDTD) analysis to solve rate equations (Eqs. 5.4 and 5.4). The detailed numerical method is presented in Appendix C.9. We tune the payoffs A(x), B(x), C(x), and D(x), linear functions along x-axis, using linear-square-fit function in Matlab (LMFnlsq) until they fit both experimental data

(ST-rich and MM-rich). Note that the spatial mean of the payoffs are the same as what we used to draw quivers in Fig. 5.3. The resulting payoffs as functions of space (or drug concentration) are shown in Fig. 5.7.

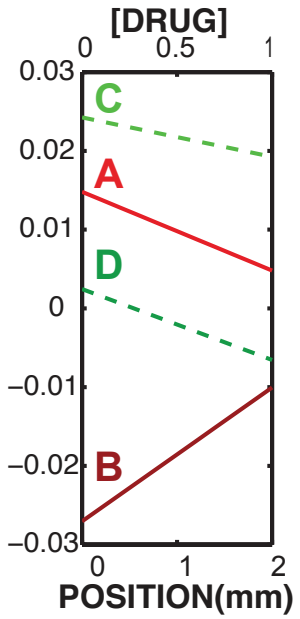

Figure 5.7: **The payoff as a linear function of drug concentration in a gradient. a** The mean and slopes are determined to match experimental results, as shown in Figure. 5.3. mean(A(x))=0.0093, mean(B(x))=-0.018, mean(C(x))=0.022, and mean(D(x))=-0.0025. The slopes of A(x), B(x), C(x), D(x), with a unit (per mm) are -0.02, 0.034, -0.01, -0.018, respectively.

To explore the effect of spatial fitness function on the dynamic behavior of population distribution, we plot the model output with an initial condition as an "uniform distribution" across the drug gradient. Fig. 5.8 and Fig. 5.9 share the same linear payoff functions, the only difference is initial populations of MM and ST are ST-rich and MM-rich, respectively.

Figure 5.8 shows the ST-rich condition, in which the initial condition is set as uniform distribution of 900 ST cells/4mm^2 versus 350 MM cells/4mm^2, same as the starting point of green arrow in Fig. 5.3. The model prediction of ST-rich population distribution within the drug gradient are shown in Fig. 5.8. The model agrees

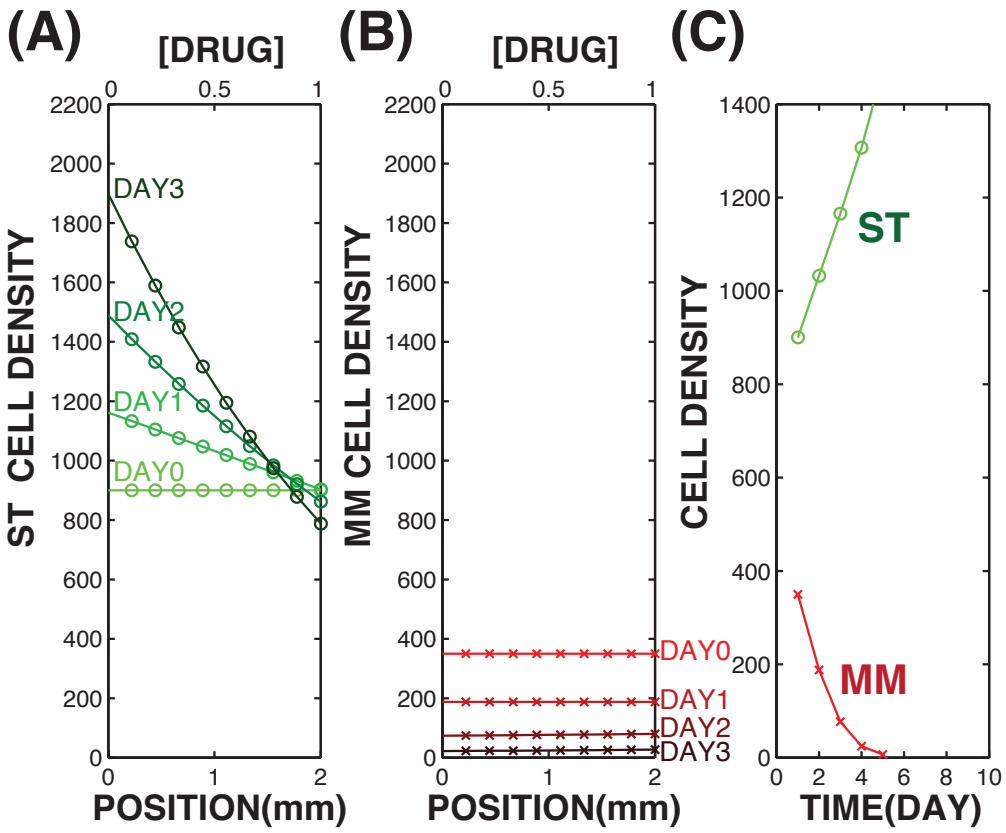

Figure 5.8: **Model prediction of ST-rich population distribution within the doxorubicin gradient.** A. ST population distribution versus time (from green to dark green). Initial condition is assumed as an uniform distribution of 900 cells/4mm^2. B. MM population distribution versus time (from red to dark red). Initial condition: uniform distribution of 350 cells/4mm^2. C. Total MM (red) and ST(green) population versus time.

with our observations that in ST-rich condition, ST cells form population gradient in response to drug gradient, less cells in the regions with greater concentration of drug (Fig. 5.6A). MM cells drop monotonically with time if its initial population is much lower than ST cells (Fig. 5.6B), but the MM distribution across the drug gradient remains approximately flat.

For the MM-rich condition, the model prediction of population distribution within the drug gradient are shown in Fig. 5.9, with an initial condition of uniform distribution of 200 ST cells/4mm^2 versus 1000 MM cells/4mm^2, the starting point of red

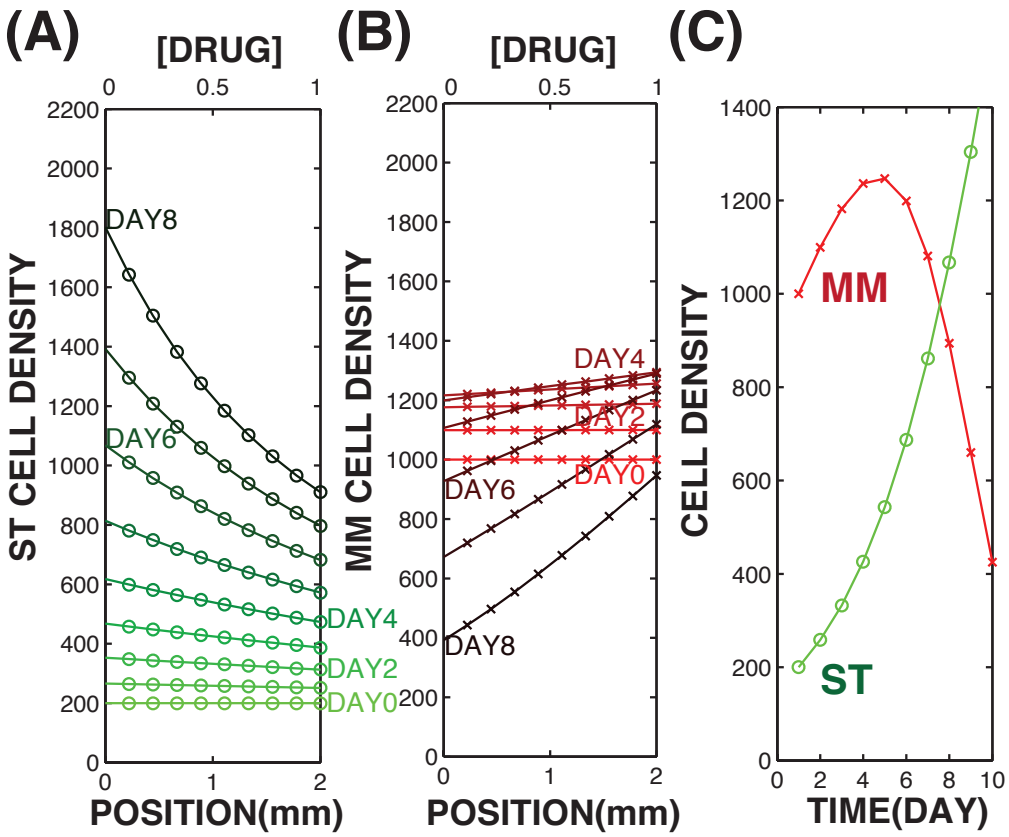

Figure 5.9: **Model prediction of MM-rich population distribution within the doxorubicin gradient.** A. ST population distribution versus time (from green to dark green). Initial condition is assumed as an uniform distribution of 200 cells/4mm^2. B. MM population distribution versus time (from red to dark red). Initial condition: uniform distribution of 1000 cells/4mm^2. C. Total MM (red) and ST(green) population versus time.

arrow in Fig. 5.3. The model is consistent with our experiments that in the MM-rich condition, the total MM population increases up to day 4 and then slowly drops with time (Fig. 5.3C and D). Interestingly, one may find the MM population gradient is against the drug gradient (Fig. 5.9B). It seems that there exists competition in the region with lower concentration of drug between MM and ST, different from our expectation that stromal cells should promote cancer survival and proliferation. Note that the population distribution after 6 days become nonlinear even with the payoff functions are linear.

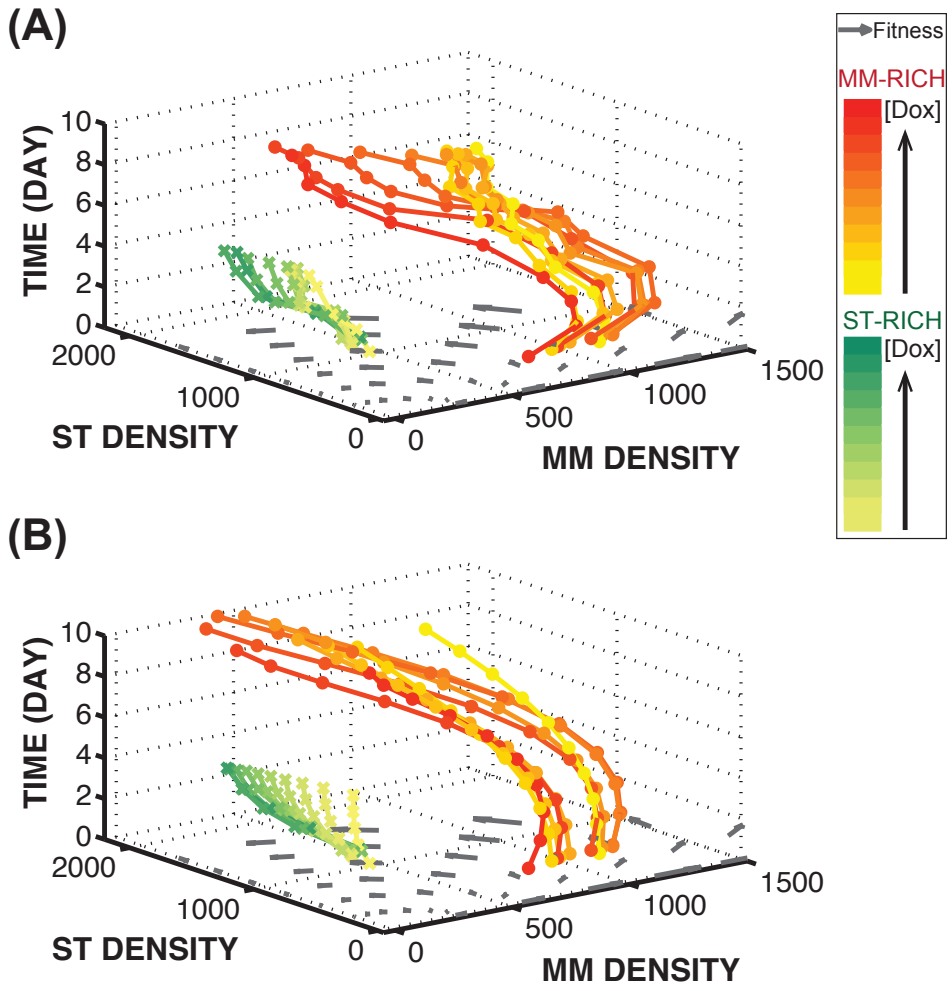

Figure 5.10: **Experiments versus model. Populations of regions with different doxorubicin concentrations in a gradient.** A. Phase portrait of experimental data (average over 3 to 5 replicates). B. Phase portrait of model with smoothed experimental data (span=3, averaged with neighboring zones) as initial condition. Yellow to red: MM-rich condition from low to high drug concentration regions. Grass to green: ST-rich condition from low to high drug concentration regions. The gray quivers are determined by the fitness as a function of population fractions (positions in xy-plane) and the payoffs at the center of the cell region.

The comparison of experiments and model output is summarized in three-dimensional phase portraits shown in Fig. 5.10, in which the z-axis is time axis.

5.2.5 Migration

Note that so far the neighboring zones in the cell growth region are independent because we only assign the payoffs in each zone and use the ordinary differential equations 5.4 & 5.5. An approach for spatial coupling is to consider one dimensional diffusive migration and fitness driven migration of the cells from each zone to another [89].

The first input is diffusive migration, which assumes that all cells migrate randomly following the Fick's Law: $J_k = -D_k \bigtriangledown k$, with D_k as the diffusion constant, and "k" is either the MM or ST density. The second input is fitness driven migration, with the assumption that cells migrate towards a region with better fitness[89]. Let fitness $f_{MM}(x,t) = A(x)p_{MM}(x,t) + B(x)p_{ST}(x,t)$, $f_{ST}(x,t) = C(x)p_{MM}(x,t) + D(x)p_{ST}(x,t)$. We obtain the partial differential equation system:

$$\frac{\partial MM(x,t)}{\partial t} = \underbrace{f_{MM}(x,t)MM(x,t)}_{\text{(i)}} + \underbrace{D_{MM}\frac{\partial^2 MM(x,t)}{\partial x^2}}_{\text{(ii)}} - \underbrace{\beta_{MM}\frac{\partial}{\partial x}[MM(x,t)\frac{\partial}{\partial x}f_{MM}(x,t)]}_{\text{(iii)}} \tag{5.6}$$

$$\frac{\partial ST(x,t)}{\partial t} = \underbrace{f_{ST}(x,t)ST(x,t)}_{\text{(i)}} + \underbrace{D_{ST}\frac{\partial^2 ST(x,t)}{\partial x^2}}_{\text{(ii)}} - \underbrace{\beta_{ST}\frac{\partial}{\partial x}[ST(x,t)\frac{\partial}{\partial x}f_{ST}(x,t)]}_{\text{(iii)}} \tag{5.7}$$

where (i) fitness by interaction, (ii) D_{MM}, D_{ST} are diffusion constants; (iii) β_{MM}, β_{ST} are the possibility of a cell moving along the fitness gradient flux.

By tracking both MM and ST cells in a device without any drug gradients, we can possibly measure the diffusion coefficients of MM and ST. The mean square displacements (MSD) versus time for MM and ST are plotted in Fig. 5.11, and the slopes indicate the diffusion coefficients of them ($MSD = Dt$). Based on polyfit function in Matlab, we found the diffusion coefficients of MM cells (D_{MM}) and ST cells (D_{ST}) are 3 and 44 $\mu m^2/min$, respectively. However, it is experimentally challenging to acquire information of β_{MM} and β_{ST}, which is beyond the scope of this work.

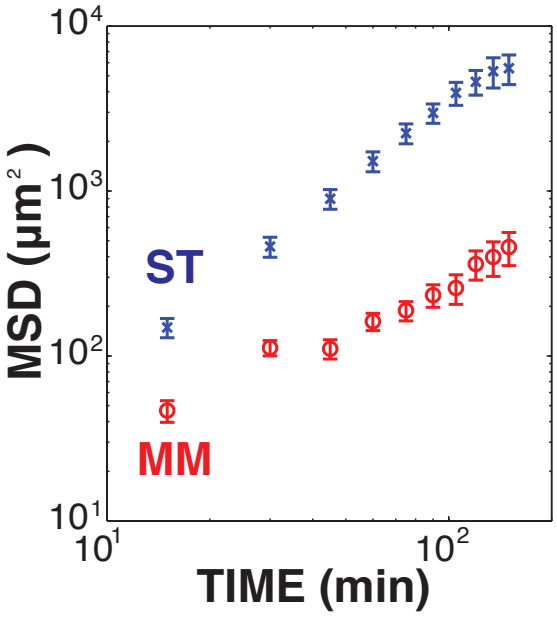

Figure 5.11: **Mean square displacements vs. time for MM and ST.**

5.3 Discussion

From a thermodynamics point of view, cell motility and developing drug resistance both have a cost of energy consumption. One common mechanism of drug resistance is upregulation of membrane drug efflux protein (Pgp), which binds to ATP and pumps the drug molecules outside of cell membrane[90]. Under drug treatment, the environmental capacity may become smaller than without drug because each cell requires more energy to be resistant or escape away[64]. Therefore, it is possible that cells were competing for nutrients at a crowded region with a lower concentration of the drug.

Conventionally, one can compare dose response of various drugs for different types of cells in single culture. If cancer and stromal cells are independent, applying a drug to the co-culture of cancer and stromal cells is a natural selection and should favor the more resistant one. However, it is more complex because cancer cells become

less sensitive to most anticancer drugs if in a co-culture with stromal cells[8]. The merit of evolutionary game theory provides a way to model the frequency dependent selection of interactive populations- cancer and stromal cells. Furthermore, if the drug concentration varies, the payoffs should vary as well because both players can change their mind if they cannot bear the stress. Thus, we here simply assume the payoffs as a linear gradient when a linear drug gradient is applied. We found that in regions with higher drug concentration, stromal cells grow more slowly while the most resistant cancer cells survive, related to previous discovery that the most aggressive cancer cells are the least limited by environmental constraint than the others[91].

In this work, we introduce a simple spatial game model to describe the population dynamics of multiple myeloma and stromal cells in a tumor-mimicking micro ecology with a drug gradient. This model considers the combination of competition and cooperation among the cells as a function of drug concentration and population structure.

Although we have not considered the migration of cells in current model, we successfully predict the future distributions of multiple myeloma and stromal cells in such micro ecology (Figure 5.10). The next question is, can we apply this analytical tool to predict cancer progression in patients? The evolutionary game theoretical model could be validated by experimental design or by mapping clinical medical imaging such as magnetic resonance imaging, computer tomography, and positron emission tomography [92]. With that information, we might be able to predict some steps of cancer progression in the short term. Integrating individual modules into systematic level involves circulation and multiple organs. Further integration, using network theory, may connect individual modules and become a promising tool to develop a systematic model of metastasis [93]. We hope this work can inspire more experimental validation, and eventually provide a clinical impact on potential intervention of cancer.

Chapter 6

Technology Transfer

In this chapter, we describe what we have worked to collaborate with multiple oncology groups to share our technology. The technology transfer includes instrumentation, chip fabrication and manipulation, and image acquisition. Early efforts include "the metronomic dosing chip" in the Sec. 6.1 and "the two-dimensional drug gradients" project in the Sec. 6.2. Recent efforts on "the Death Galaxy chip for mammalian cells" are described in the Sec. 6.3. Some preliminary experiments conducted at our collaborators' laboratories and discussions are also presented in this chapter.

6.1 Metronomic therapy (Princeton and UCSF)

Princeton and UCSF have been interested in using microfluidic devices to mimic metronomic therapy for controlling cancer. This work was conducted by Amy Wu and James Sturm (the Princetonian), collaborating with David Liao, Luis Estevez-Salmeron, Chira Chen-Tanyolac and Thea Tlsty (the San Franciscan).

Cancer is a heterogeneous and unstable population which undergoes "phenotypic stochasticity"[94]. Within a cancer cell population, some cells become more resistant to chemotherapy than the other cells since differences in protein levels can correspond to differences in drug-sensitivity. Another concept of phenotypic stochasticity is that

reversible transitions back and forth between different states (i.e. degree of resistance) may occur in a cancer population. For example, up-regulation of multidrug resistance proteins (MDR), the drug efflux pumps, reduces intracellular drug concentration and results in elevated drug resistance. Without the presence of drug molecules, MDR expression decrease to normal levels since these proteins are not necessary in normal (stress-green) condition.

Princeton and UCSF are interested in understanding the generation of heterogeneity within a cell population and the control of population composition based on the concept of phenotypic stochasticity. In particular, we would like to study both the ongoing emergence of drug resistance and the depletion of drug-resistant cells. The later aim is associated with "metronomic therapy", a proposed method to optimize dosing schedules. Doses greater than the maximum-tolerated dose (MTD) would cause toxicity so that current strategy of MTD therapy kills the cancer just before the drug kills the patient. High-frequency, low-dose therapy has been called "metronomic therapy", which has shown 4 times overall survival (6 years) compared with the low-frequency, MTD control on a clinical trial of women with metastatic breast cancer [95].

Our experimental system focuses on the interaction between (1) breast cancer cells' resistance to the drug methotrexate (MTX) and (2) the level of the enzyme dihydrofolate reductase (DHFR) in individual cells. MTX binds to DHFR, preventing the enzyme from participating DNA synthesis and further inhibiting cell growth. However, cells exposed to MTX can still proliferate if they express high levels of enzyme DHFR. The higher the concentration of MTX is applied, the higher level of DHFR is required for cell survival. In this view, increasing drug/MTX-resistance can be corresponding to increasing protein (DHFR) level. The dynamic fluctuations of DHFR would result in interconversion between relatively drug-sensitive state and drug-resistant state. If the MTX concentration periodically increases "faster" than

the accumulation of DHFR sufficient for cancer cell survival, the therapy could be effective to inhibit cancer cell growth[96].

Optimization of dosing schedules thus provides an opportunity for effective cancer treatment. So how to optimize the dosing schedules in the MTX-DHFR system? To simulate metronomical conditions in a cell culture, we want to raise or lower drug concentrations over time. Conventionally, reducing drug concentration requires removing media with drugs and replacing it, that disturbs the cell culture. We propose that microfluidic technology could become a solution to control temporal dynamics of drug dosage and assess single cellular levels of DHFR. The expression levels of DHFR in each cell can be monitored by using fluorescein methotrexate (F-MTX)[97, 98]. The quantitative binding of F-MTX (green fluorescent) to DHFR enables researchers to measure DHFR expression levels by fluorescence microscopy.

As shown in Fig. 6.1, the system of metronomic dosing chip is composed of the gradient chip (Section 2.2), two syringes (one continuously supplies growth medium, the other supplies F-MTX), additionally, two three-way stopcocks valves, and two tee connectors. At the drug ON state, F-MTX solution enters the chip, and gradually diffuses into cell culture region. At the drug OFF state, growth medium enters the chip, and gradually clear the residual F-MTX solution in the cell culture region. In this system, we can probe the drug levels based on green fluorescence in the cell culture region, and assess DHFR expression levels based on green fluorescence of individual cells after the clearance of F-MTX solution. The more DHFR a cell expressed, the higher fluorescent intensity a cell retained after removal of drug (F-MTX).

A preliminary data of cells in the metronomic dosing chip with two dosing cycles is shown in Fig. 6.2. Initially, we loaded the MDA-MB-231 on the chip based on the protocol in Appendix B.3. After 16 hours, we switched the three-way stopcocks valves and turn the drug on. The image taken after 39 hours shows that the F-MTX occupied the cell region. After 40 hours, we removed F-MTX. The image acquired

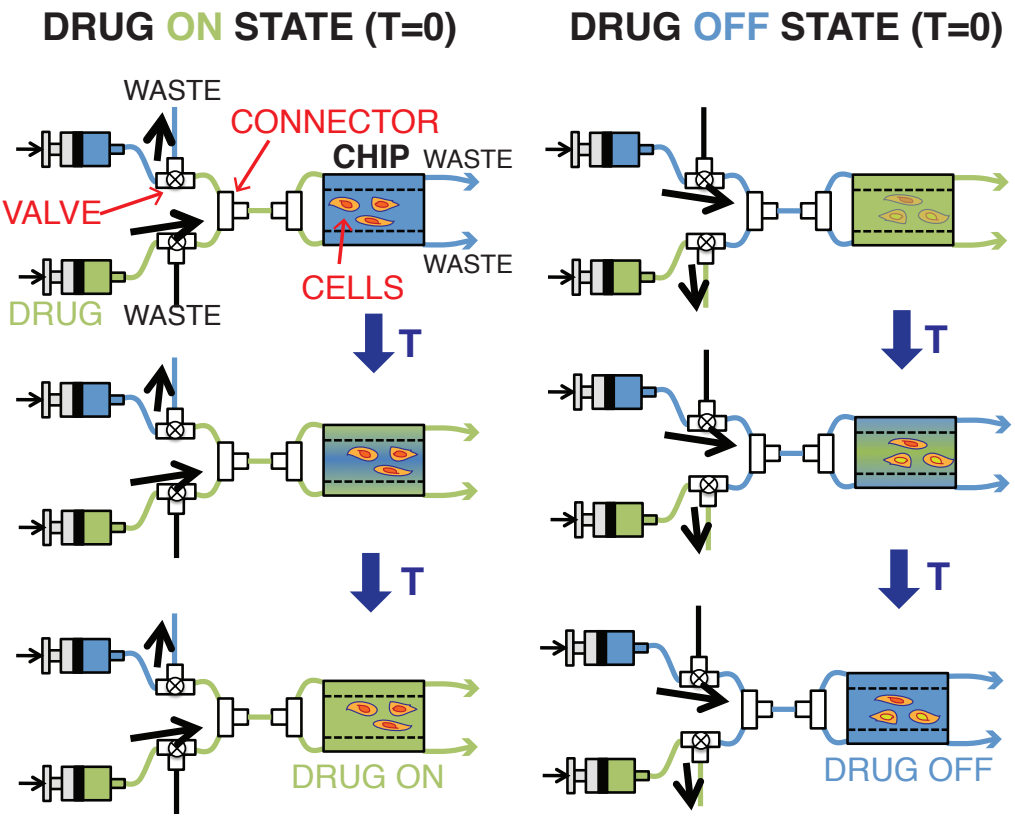

Figure 6.1: **The metronomic dosing chip system.** The syringe with F-MTX (green) and the syringe with growth medium (blue) are pumped continuously. The three-way stopcocks (Cole Parmer) are switched back and forth to enable fluid flow in drug ON/OFF directions (black bold arrow). After the cells exposed to F-MTX, some cells expressing more DHFR would appear higher intensity of green fluorescence.

after 42 hours indicates the heterogeneous expression levels of DHFR for different cells. After 87 hours, the F-MTX was cleared in cell culture region and some cells still appear green fluorescent, indicating their high expression levels of DHFR. We then repeated the dosing cycle after 88 hours and assess the cells after 113 hours.

In summary, we built a microfluidic system to assess spatio-temporal dynamics of drug (F-MTX) dosing and cell phenotype- single cellular content of DHFR. The microfluidic system can be upgraded by adding electronic control of the three-way stopcocks valves. On the other hand, there are several challenges of F-MTX and DHFR experiments. F-MTX labels DHFR but it is also a drug. Therefore, when drug

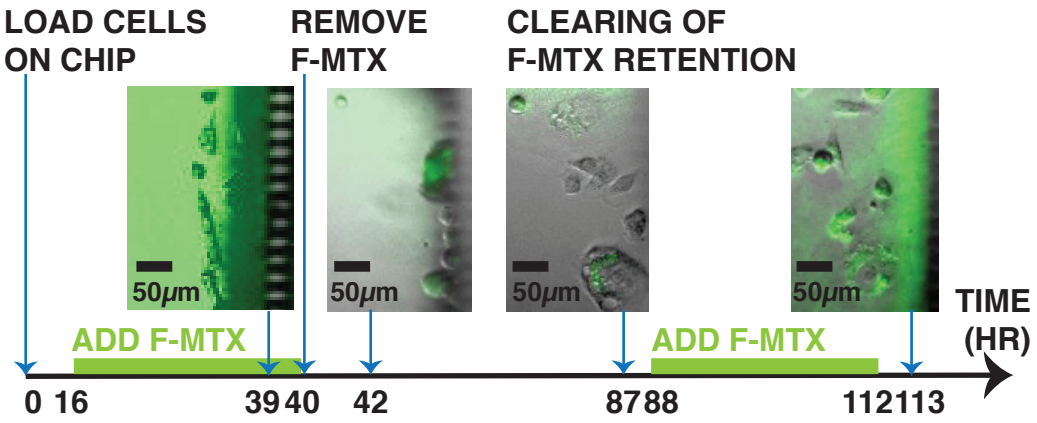

Figure 6.2: **Exposure of MDA-MB-231 cells to F-MTX in the metronomic dosing chip.**

is visible, the DHFR expression becomes invisible. The system will be improved if the drug concentration and the live-cell DHFR expressions can be assessed independently. We hope biologists may provide assistance to construct DHFR-RFP labeled cells for performing the same experiments.

6.2 Combination of Taxol and TGF-β and therapy resistance (Princeton and Salk)

Princeton and Salk Institute have been studying the effect of tumor-mimicking Taxol gradients on premalignant breast cancer (MCF10A) cell growth. This work was mainly conducted by John Bestoso, Amy Wu (Sturm and Austin Laboratory at Princeton) and Fernando Lopez-Diaz (Emerson Laboratory at Salk).

Taxol is an anti-cancer chemotherapy drug which interferes with the normal break-down of microtubules during cell division. Fig. 6.3 shows green fluorescent MCF10A cells grown in one-dimensional gradient chip (used in Chapter 4 and Chapter 5) at Salk Institute using the instrumentation described in Appendix A. As expected, MCF10A cells form a population gradient in response to the Taxol gradient in 96 hours.

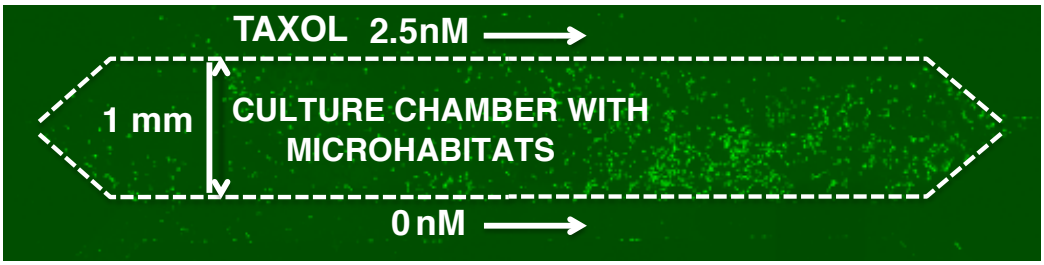

Figure 6.3: **Exposure of MCF10A cells to an Taxol on-chip gradient with microhabitats (Salk).** Taxol treatment for 96 hours with a gradient of 2.5nM/1mm.

We are now interested in how transforming growth factor beta (TGF-β) affects the evolution of drug resistance. TGF-β is a pleiotropic cytokine abundant in breast tumors. Salk researchers have determined that TGF-β protects cancer cells from chemotherapeutic drug-induced death at least partially by suppressing the P53 gene, but how cells sense the linear gradients of chemotherapeutic drugs and TGF-β existing in tumor tissues is still unknown [99]. Therefore, we have designed a prototype chip to create gradients of both Taxol and TGF-β, and has begun testing and validation.

To create two-dimensional concentration gradients, we apply four boundary conditions at the sides of a square-shaped culture region. The microposts at the sides of the culture region block direct fluid flow from the side channels and allow diffusion of drug molecules to build up the gradients. The Comsol simulation coupling the Laminar flow model and chemical transport model is shown in Fig. 6.4A. To create two perpendicular gradients across the culture region, we apply Taxol at the right two sides of the culture region, buffer at the top two sids, and TGF-β at the bottom two sides. In this design, the chip has totally 4 inlets and 4 outlets. The buffer is continuously provided from the top-left inlet, TGF-β is pumped into the bottom-left inlet, Taxol is pumped into the top-right inlet, and the mixture of TGF-β and Taxol is provided from the bottom-right inlet.

The two-dimensional gradient chip is designed to be compatible with the same apparatus used for one-dimensional chips. It features 2mm by 2mm culture chamber

with hexagonal microhabitats. This silicon chip is fabricated using the protocol in Appendix B.1. As shown in Fig. 6.4B, we use green fluorescent dye (fluorescein) and red fluorescent dye (rhodamine 6G) to visualize the 2D gradients of Taxol and TGF-β, respectively.

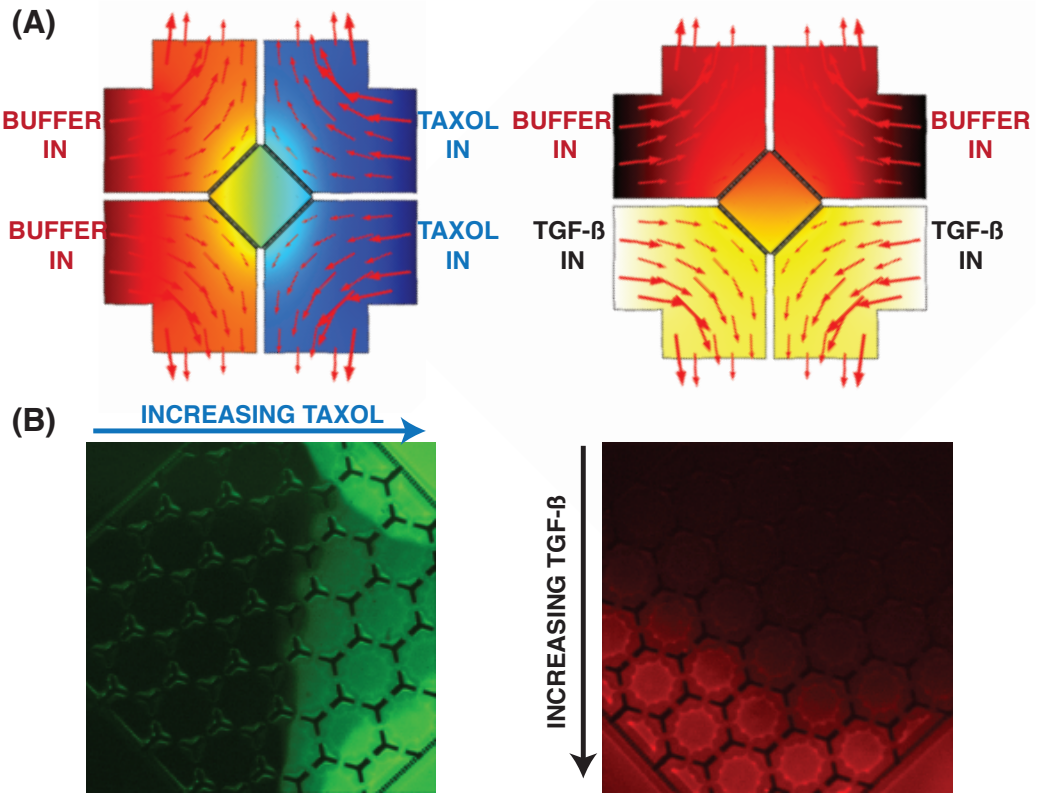

Figure 6.4: **The two-dimensional gradients chip: simulation and gradients characterization.** A. Comsol simulation. B. Gradient characterization using green fluorescent dye (fluorescein) and red fluorescent dye (rhodamine 6G).

In this section, we have demonstrated multi-day premalignant breast cancer cell culture on-chip, cellular response to a one-dimensional Taxol gradient, and a two-dimensional gradient chip design. We transferred our chip technology and live-cell imaging instrument so that the cell experiments are now able to be conducted at the Beverly Emerson Laboratory at Salk Institute. In future, we would like to apply the two-dimensional gradient chip to study the nonlinear effect of Taxol and TGF-β on breast cancer cells. We hope that the two-dimensional gradient chip can be used to

study the synergistic effect of cocktail therapies for various types of cancer and may provide clinical impact on personal medicine.

6.3 The Death Galaxy chips for mammalian cells (Princeton, UCSF and JHU)

Princeton Physical Sciences-Oncology Center have been transferring the microfluidic technology within the network. This work is the collective efforts emerged from Robert Austin, Douglas Austin, Brandon Comella, James Sturm, and Keh-Chih Lin (the Princetonian); Gonzalo Torga and Kenneth Pienta (the Hopkins); Chira Chen-Tanyolac and Thea Tlsty (the San Franciscan).

The Death Galaxy chip is an evolution reactor which was first designed for bacteria by Zhang et al [4]. It considers two key factors of accelerating the evolution: stress gradient and meta-population, as discussed in Sec. 1.2 and Sec. 1.3. The configuration of the Death Galaxy chip is different from our cancer works described in Chapter 4-5, which is based on a linear one-dimensional stress gradient. The Death Galaxy chip is composed of various strengths of gradients across a large hexagonal cell culture region (with arrays of small hexagonal microhabitats), as shown in Fig. 6.5. Thus, it creates a more complex fitness landscape and has been demonstrated to accelerate the emergence and fixation of antibiotic-resistant bacteria.

The difference between bacteria and cancer has been introduced in Sec. 1.4. Also, how the parameters such as growth rate, motility, and cell size influence on microhabitats design has been discussed in Sec. 4.2. In this section, we not only change the chip configuration but also use a new material, Lumox membranes (Sarstedt), as the cell culture substrate.

Lumox membranes are characterized by their ultra-thin, gas-permeable, low-autofluorescence film base, enabling a range of applications from tissue culture

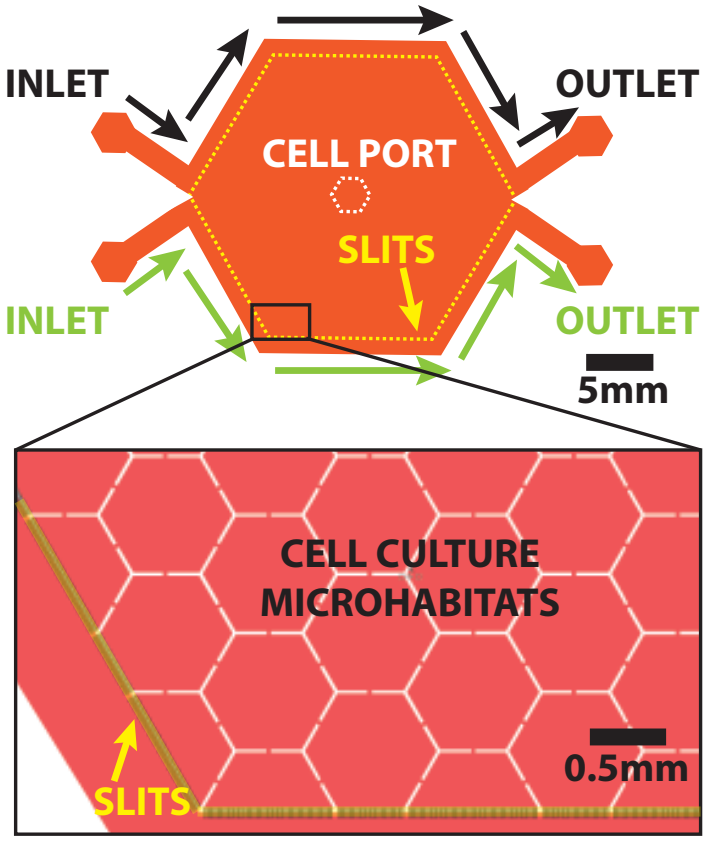

Figure 6.5: **The top view of the Death Galaxy design for mammalian cells.**The red shaded area shows the cell culture chamber and peripheral channels which are 60 μm tall. White hexagonal walls weakly divide the cell culture region into microhabitats. The green and black arrows from inlets to outlets are the flow directions in the peripheral channels, which are separated from the cell culture microhabitats by arrays of slits (yellow). The position of cell port is marked by white dotted lines.

to fluorescence-based cell assays. However, these membranes are rarely discussed as substrates for microfluidic cell culture devices, because Lumox does not bond well to polydimethylsiloxane (PDMS), arguably the most widely used material in microfluidic technology. This technical challenge can be solved by developing a custom clamp to press PDMS-based devices against Lumox substrates, as detailed in Sec. 6.3.1. The combination of the Death Galaxy chip and Lumox substrate dish opens the opportunities to explore the dynamics of cell under liquid stressors (such as chemotherapy) and gaseous stressors (such as hypoxia).

6.3.1 Experiments

The Death Galaxy design for mammalian cells is shown in Fig. 6.5. The PDMS chip, with a depth of 60 μm, is fabricated based on the protocol in Appendix B.1. The cell culture region is occupied by arrays of 250 hexagonal wells (microhabitats). Each well has sides 500 μm long and is connected to its nearest neighbors via six microchannels that are 20 μm long and 20 μm wide. Slits are 5 μm wide on the sidewalls of the peripheral wells at the edge of the array to allow nutrients and stressors (such as drug or glucose-free growth medium) to flow into the interior of the array. The center of the cell culture region is a cell port (white in Fig. 6.5) for loading the cells. The stressor (drug, or other chemicals) gradient can be built up by supplying stressor-containing growth medium at the top peripheral channel (black in Fig. 6.5) and stressor-free growth medium at the bottom peripheral channel (green in Fig. 6.5). The slits (yellow in Fig. 6.5) enable the diffusion of stressor molecules and create various strengths of drug gradients across the cell culture region since the two peripheral streams are separated by different distances.

Chip packaging and cell loading process is described in Fig. 6.6.

6.3.2 Preliminary results

Here we use a compound microscope with a micro-incubator, as shown in Fig. A.1D. This on-chip live-cell imaging system (incubator and microscope) is detailed in Appendix A. The preliminary result of bone marrow stromal cells (HS-5/GFP) in the Death Galaxy is shown in Fig. 6.7. With a large imaging area (2" by 2"), we can capture a high resolution image of the whole Death Galaxy chip and also zoom in to achieve single-cell resolution.

At Thea Tlsty Laboratory at University of California- San Francisco, the breast cancer cells (MCF10A/GFP) were introduced into the Death Galaxy chip by Chira Chen-Tanyolac (UCSF) for 2 days. The chip was then transferred to Nader Pourmand

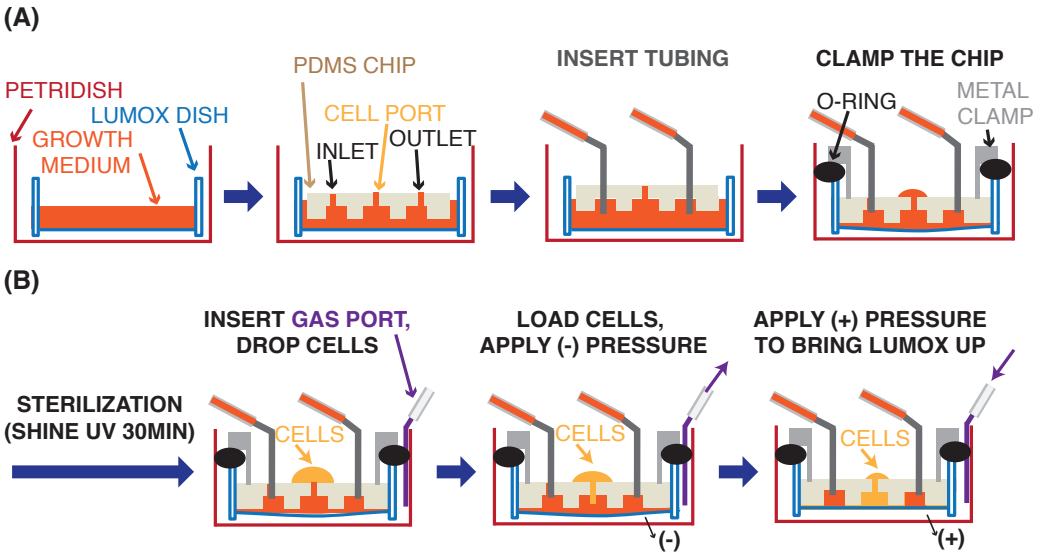

Figure 6.6: **The side view of packaging and cell loading process of the Death Galaxy chip. A. Packaging process.** 1. The Lumox dish is filled with growth medium. 2. The PDMS chip is inserted into the Lumox dish. 3. The tubing is connected with a syringe filled with growth medium (or stressor). 4. The metal clamp (gray) with an o-ring (black) presses the PDMS chip (ivory) against the Lumox membrane, which becomes concave up. At this point, there are some excess growth medium sandwiched by the PDMS chip and the Lumox membrane. **B. Cell loading process.** 1. Before loading cells, the chip was sterilized by UV exposure for 30 minutes. 2. The gas port (purple) is a needle penetrating through the o-ring, and connected with a gas regulator. 3. After the cell solution (a million cells per mL) is dropped on top of the cell port, a negative pressure is applied below the Lumox membrane by sucking air through the gas port. 4. The cells enter the culture chamber. 4. During the experiment, premixed air with 5% CO_2 is applied through the gas port to hold the Lumox membrane agains the PDMS chip.

Laboratory at University of California-Santa Cruz for testing on-chip cell collection using nanopipette technology.

As shown in Fig. 6.8A, Nader Pourmand Laboratory used a micromanipulator-controlled nanopipette to collect cells from the chip (soaked in red growth medium). Since the Lumox membrane reseals and remains leak-proof after being penetrated through (Fig. 6.8B-C), it provides a great potential for time-lapse cell-collection without interruption of the ongoing experiments. With this technology, the dynamic

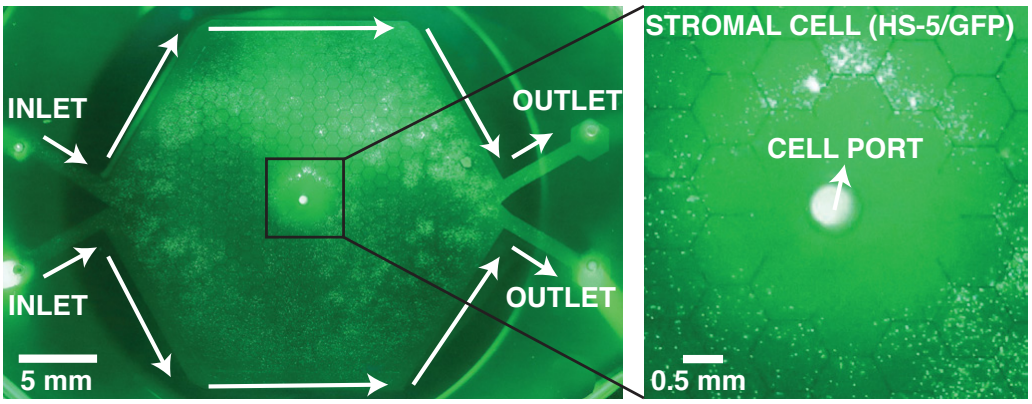

Figure 6.7: **Bone marrow stromal cells (HS-5/GFP) in the Death Galaxy.** Using a compound microscope, we can achieve single-cell resolution in one snap shot covering the whole chip.

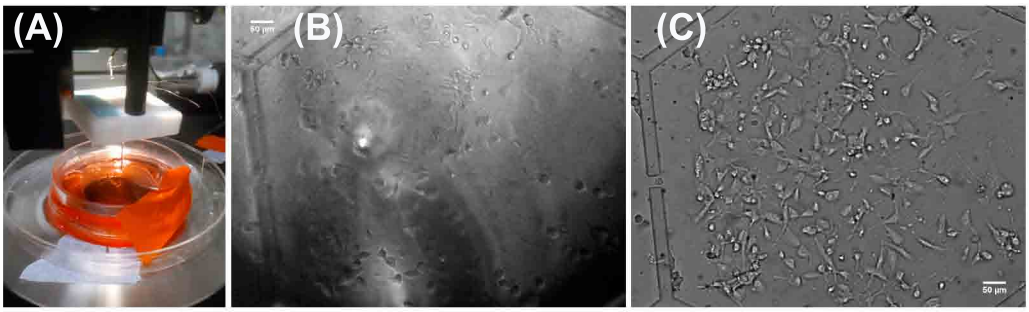

Figure 6.8: **MCF10A cells (MCF10A) collected from the Death Galaxy using nanopipette.** A. Micromanipulator-controlled nanopipette on top of the Lumox membrane. Breast cancer cells (MCF10A) were grown beneath the Lumox membrane, inside the chip. B. Micrograph of cells in the chip while the nanopipette was penetrating through Lumox membrane (thus out of focus). C. Micrograph of cells in the chip after the nanopipette was withdrawn. The Lumox membrane resealed due to membrane tension. Image courtesy of Nader Pourmand Lab at University of California-Santa Cruz.

cellular response to the spatial heterogeneity (created by the Death Galaxy) could be assessed via biomolecular measurements such as qPCR or RNA-sequencing.

In collaborating with Kenneth Pienta Laboratory at Johns Hopkins Medical Institute, we propose to study nonlinear interactions between various types of cells in prostate tumor and how that would impact cancer metastasis. This project is an experimental validation of the evolutionary game theory discussed in the Chapter 5. In

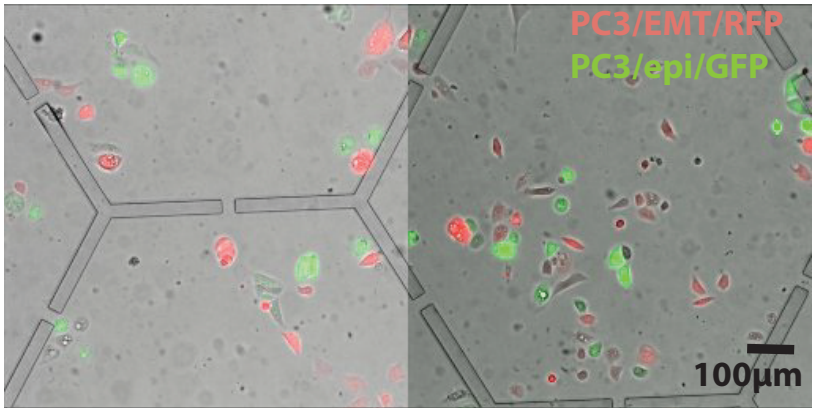

Figure 6.9: **Co-cuture of two types of prostate cancers (PC3/EMT-RFP and PC3/epi-RFP).** This image was acquired at Princeton University using a Nikon TE2000 microscope with a 10X objective.

the preliminary experiments, we co-culture prostate cancer cells PC3/epi/GFP and PC3/EMT/RFP in the Death Galaxy chip. PC3/epi/GFP are epithelial prostate cancer cells, and PC3/EMT/RFP are invasive prostate cancer cells which underwent epithelial-mesenchymal-transition (EMT). The PC3/epi/GFP and PC3/EMT/RFP cells are labeled with green and red fluorescent proteins, respectively (Fig. 6.9).

To acquire high resolution wide view image for the entire chip, we constructed a high resolution dual-color compound microscope with a micro-incubator, detailed in Appendix A. The preliminary result acquired at Johns Hopkins Medical Institute is shown in Fig. 6.10.

The Death Galaxy chip for mammalian cells is an ongoing project and the technology is still evolving based on the user experience of our collaborators. We hope the dynamic behaviors of cancer in the Death Galaxy chip, a complex fitness landscape, would inspire novel therapy design and provide more insights on the fundamental mechanisms of cancer progression.

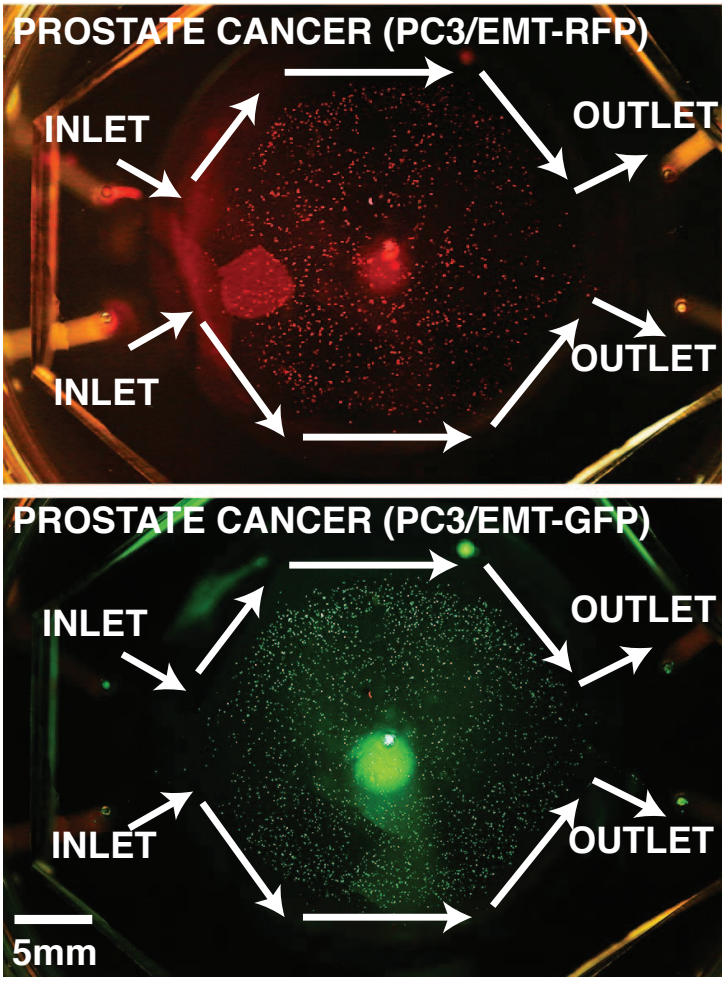

Figure 6.10: **Co-cuture of two types of prostate cancers (PC3/EMT-RFP and PC3/epi-RFP).** Image courtesy of Gonzalo Torga from Kenneth Pienta Laboratory at Johns Hopkins Medical Institute.

Chapter 7

Conclusion

7.1 Summary

In summary, we have studied the evolution of drug resistance in cancer using 3 approaches: microenvironments, genomics, and game theory. By constructing a tumor-mimicking microenvironment with a drug gradient, we could probe the population dynamics of cancer cells (and their interaction with stromal cells), accelerate the evolution of cancer drug resistance, and explore the genomic changes of cells in response to a drug gradient landscape.

In Chapter 2, we demonstrated the rapid emergence of breast cancer cells resistance to doxorubicin within three days in a microfluidic device with a drug gradient. We characterized phenotypic behaviors of breast cancer cells in the drug gradient environment, including cell population dynamics and migration. We surprisingly discovered that resistant cells were able to divide at high levels of drug, and migrate toward the drug source. However, we did not understand how can resistant cells spread in a population rapidly. The open question led us to explore the horizontal gene transfer in cancer, which was discussed in Chapter 3.

In Chapter 3, we tested the hypothesis that horizontal gene transfer in cancer plays a significant role in spreading drug resistant phenotypes in a population of breast cancer cells. We used histone-fluorescent proteins as indicators to probe the dynamics DNA transfer among cancer cells. Preliminary result shows that the genotoxic drug, doxorubicin, increases the rate of DNA transfer. The mechanism is still unknown and future direction addressing this topic will be discussed in Sec. 7.2.

We incorporated the concept of microhabitats into the drug gradient environment, to explore the emergence of rapid multiple myeloma evolution in Chapter 4. We observed a rapid emergence of myeloma resistance to doxorubicin, up to 16-fold, within 2 weeks instead of 10 months by conventional protocol, in such microenvironment. Then we focused on the genomic analysis of these resistant myeloma cells and their parental cells, including *de novo* mutations and expression levels, to unveil biomolecular signatures of rapid resistance to drug. Strikingly, the mutational cold spots which were abnormally regulated (4x) in the resistant cells, are more ancient (3 billions years old) compared to most human genes, indicating these "never-mutated genes" preserve very important functions to maintain the fitness of the cells, such as spermatogenesis, oxidation-reduction process, and apoptotic process.

In Chapter 5, we studied the myeloma resistance from an ecological perspective instead of the biomolecular perspective as shown in Chapter 4. Here we explore the nonlinear interaction of multiple myeloma cells and bone marrow stromal cells in the microenvironment used in Chapter 4, with a drug gradient and microhabitats. Although stroma-mediated drug resistance has been previously well investigated, we found that in a drug gradient landscape, stromal cells prolong the survival of myeloma cells in a high drug region, but outcompete myeloma cells at the low drug region. We developed a spatial evolutionary game theoretical model to describe the dynamics of myeloma and stromal cells, and successfully predict the progression of myeloma in such complex landscape.

In Chapter 6, we transferred our microfluidic and imaging technology to our collaborating labs. Collaborating with UCSF, we designed the metronomic dosing chip for the optimization of dosing schedules. Working with Salk Institute, we designed the two-dimensional gradients chip to study the combination of Taxol and TGF-β and therapy resistance. Furthermore, we developed the Death Galaxy chip for mammalian cells, an evolutionary accelerator which has been demonstrated in bacteria evolution of antibiotic resistance. Also, we explored the usage of the Lumox substrate, which enabled the collection of cells during ongoing experiments. Preliminary data conducted by our collaborating labs within Princeton Physical Sciences-Oncology Center were also presented in this chapter.

In Appendix A, we described four live-cell on-chip imaging approaches which are essential for data collection in this thesis. These experimental systems were also transferred to our collaborators' labs. All experimental protocols including device fabrication, cell culture, image acquisition and analyses, biological characterization (DNA damage, dose response), and transcriptome sequencing were presented in Appendix B. Statistical analysis, sequencing analyses, training and validation of models, and finite-difference method were shown in Appendix C.

Physical sciences approaches into oncology problems provides an alternative perspective in probing the complexity of cancer. Furthermore, we gained a better understanding of chemotherapy resistance, with implications for novel therapy design. For examples, non-mutated genes could be targets for prevention of cancer fitness, or stromal cells could be utilized as "antagonists" of cancer cells. The engineered micro environments with drug gradients, as an evolutionary accelerator, may enable rapid drug screening for cancer patients. In all, our research has contributed to the field of cancer evolution by focusing on reconstruction of a heterogeneous tumor microenvironment to study cancer genomes and interactions among various cells. We hope

this work can inspire further experimental validation, and eventually may provide a clinical impact on the intervention of cancer.

7.2 Future perspectives

In this thesis, we explored the rapid evolution of chemotherapy resistance in cancer in a landscapes with drug gradients. Although we focused on emergence of drug resistance, applying the microfluidic approach of accelerating cancer evolution may allow us to study the malignancy transformation of cancer. For examples, acidity and hypoxia are constantly observed in tumors. Would these environmental cues trigger the initiation of cancer or further induce cancer invasion, the first step of metastasis? With excellent spatio-temporal control of fluids, microfluidics would provide a great opportunity for probing spatio-temporal dynamics of human cells and may further suggest how to control cancer population by optimization of dosing schedules.

Also, information transfer (via metabolite transfer, protein transfer, or gene transfer) among various types of cells is clearly an important driver of cancer progression and requests more contributions from engineers, biophysicists, and quantitative biologists. Our proposal of exploring "how cancer cells may accept DNA from neighboring cells to construct a more heterogeneous genome" received the Young Investigator Award by the Physical Science Oncology Center program of the National Cancer Institute in 2013. In collaboration with molecular biologist (Fernando Lopez-Diaz, Beverly Emerson Laboratory) from Salk Institute and theorist (Chris MacFarland, Leonid Mirny Laboratory) from MIT, we used fluorescent protein with high DNA affinity as a live-cell DNA marker, and quantified the frequency of DNA transfer in various environments. Preliminary result shows that the DNA transfer event can only be detectable for metastatic breast cancer cells under genotoxic drug exposure, indicating the demand of creating a more heterogeneous genome under stress, as pre-

sented in Chapter 3. This work may provide deeper insights if we can detect the gene fusion in the recipient cells.

Moreover, we may pursue greater clinical impacts by comparing *in vitro* or *ex vivo* data to medical imaging database (such as Cancer Imaging Program of the National Cancer Institute) and genomic sequencing databases (such as COSMIC). What we learned from Chapter 4 is that ancient mutational cold spots play essential roles of cancer cell survival in rapidly evolved multiple myeloma cells. With publicly available sequencing data for various types of cancer, it is possible to find a deterministic and generalized pattern of mutational landscape in cancer evolution.

The complex dynamics of interacting myeloma and stromal cells described in Chapter 5 may have been observed by oncologists during clinical trials. Since stroma-mediated resistance has been widely accepted by oncologists, the "stroma inhibitor" developed by David Tuvecson Laboratory at Cold Spring Harbor Lab was once a promising candidate for targeted therapy. However, it failed to pass the phase II clinical trial because once the stromal cells were inhibited, cancer becomes even more aggressive. This example demonstrated the limitation of conventional tissue culture experiments and a great potential of microfluidic devices for addressing the complexity of cancer. With more validations of the physiological relevance, the microfluidic "evolution incubator" can be applied to rapid drug testing and provide significant insights on therapy design.

Appendix A

Instrumentation: On-Chip Live-Cell Imaging System

In this thesis, we study the long-term (multi-day) cancer cell dynamics in various microfluidic chips with a drug gradient. Time-lapse imaging of cell behaviors, such as proliferation, death, and migration, is the major source of data in our studies. The mammalian cell culture requests an incubating environment with a temperature fixed at 37^{o}C, humidity (RH) as 97-100%, and the atmosphere contained with 5% CO_2 for buffering the pH of growth medium. Therefore, an imaging instrument with a cell culture incubator which allows the manipulation of microfluidic chips is essential for data acquisition. The illustration of four on-chip live-cell imaging systems that we used is shown in Fig. A.1.

In Chapter 4 and 5, samples were kept in a conventional incubator (Fig. A.1 A). A Nikon upright microscope and a Qimaging charge-coupled device camera were used to obtain daily images of bright field, red fluorescent, and green fluorescent channels.

In Chapter 3 and 5, time-lapse red and green fluorescent images were acquired by a Nikon inverted microscope and an EMCCD charge-coupled device camera. The samples were in a micro-inbubator on the stage with fixed humidity and 5% CO_2, and

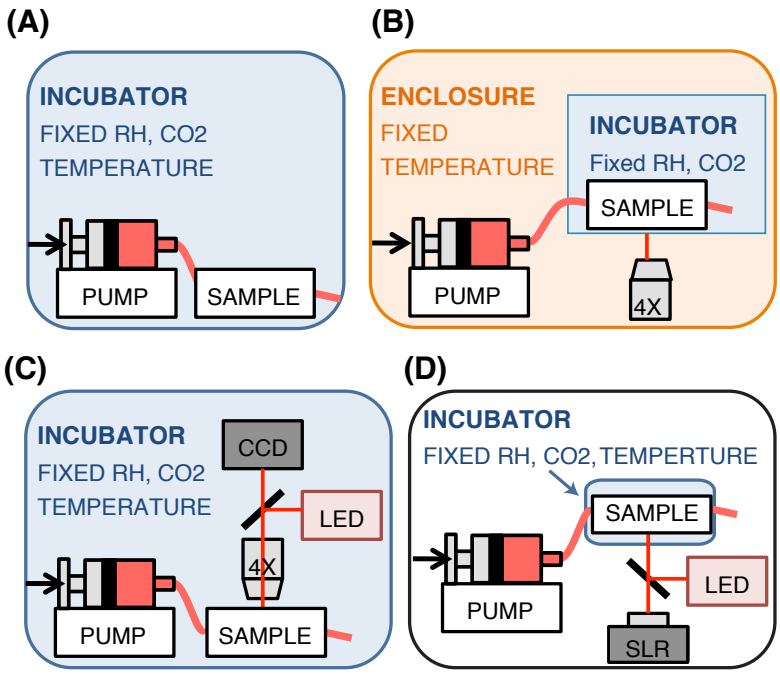

Figure A.1: **Microfluidic device, syringe pump, incubator, and cell-imaging system.** A. Conventional incubator. B. Cage incubator (OKOLab) on a conventional microscope. C. Compound microscope in a conventional incubator. D. Compound microscope with a micro-incubator. In any case the temperature is fixed at 37°C, humidity (RH) is 97-100%, and the atmosphere contains 5% CO_2 for buffering the pH of growth medium.

the syringe pump was inside a large temperature-controlled enclosure, as shown in Fig. A.1 B. To load the samples on conventional multi-well plate holder in conventional microscopes, we designed and machined an adapter which fits our device manifold and the multi-well plate holder (Fig.A.2). This setup was replicated at Thea Tlsty's Laboratory at University of California at San Francisco and some preliminary data were demonstrated in Sec. 6.3.

In Chapter 2, the cells in the device were observed by acquiring epi-bright field images every 5 minutes using a compound microscope (with a white LED, beam splitter, 4X objective, and a CMOS camera from Thorlabs, Inc). The entire device, the syringe pump to supply the growth medium and drugs (if any), and the imaging system were placed inside a conventional incubator with 5% CO_2 and 37^oC (Fig.

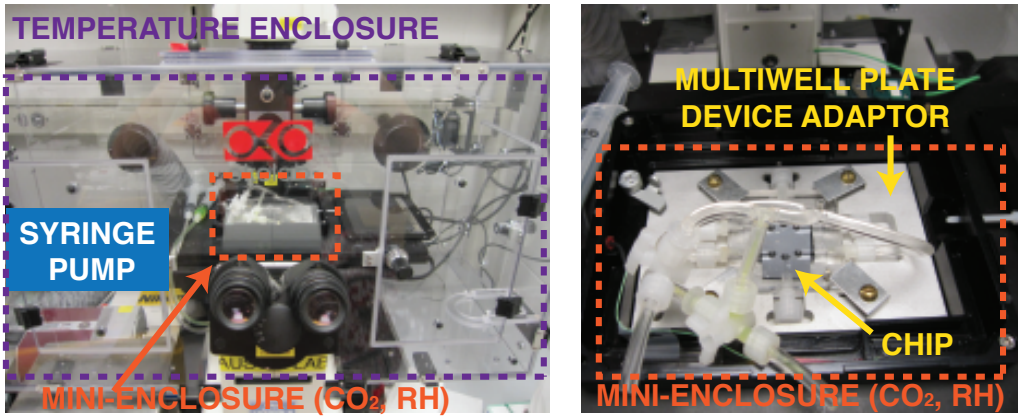

Figure A.2: **Photo of a microfluidic device in a manifold, and an OKOLab incubator on a Nikon inverted microscope.** The mini-enclosure is supplied with humidified air with 5% CO_2. Inside the mini-enclosure, a multiwell plate-device adaptor holds an acrylic manifold with a silicon chip, allowing tubing insertion for growth medium and drug delivering.

A.1 C). Similar setup for visualization of green fluorescence was built at Beverly Emerson's Laboratory at Salk Institute, as shown in Fig. A.3. Instead of a white LED and a beam splitter, we used a blue LED as excitation light source and a dichroic mirror which reflects blue excitation light and enables green fluorescence emitted by GFP-labelled cells to pass through. Preliminary data acquired at Salk Institute was presented in Sec. 6.2.

In Kenneth Pienta Laboratory at Johns Hopkins Medical Institute (JHMI), we built a dual-color compound microscope with a micro-incubator, as shown in Fig. A.4. This system was similar to the one described in Fig. A.1D. The micro-incubator had a thermocouple and conducting tapes for feedback temperature control, and tubing insertion for introducing humidified premixed air with 5% CO_2. The dual-color compound microscope was composed of two beam splitters, two LED illumination systems (one blue LED for exciting green fluorescence, and one green LED for exciting red fluorescence), two emission filters (one allows green fluorescence and the other allows red fluorescence to pass through) on a motorized filter flip mount, and a SLR

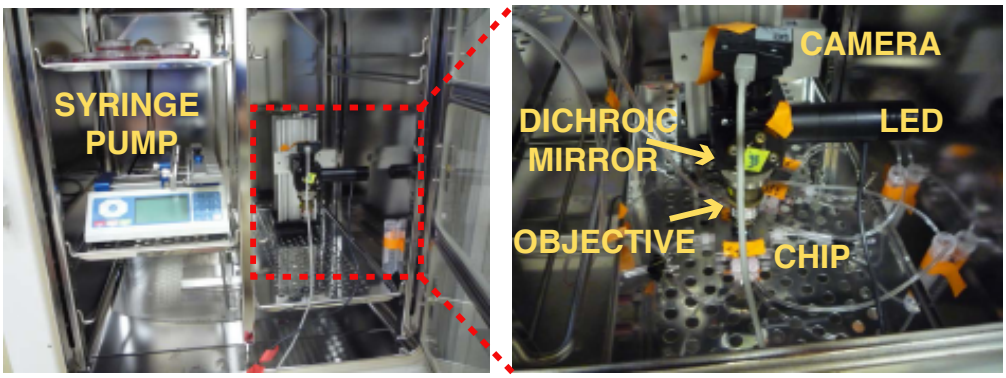

Figure A.3: **Photo of the green fluorescence imaging setup at Salk Institute.** Inside a conventional incubator, we put a syringe pump for introducing liquids into the chip. The compound microscope was composed of a camera, a blue LED, a dichroic mirror, a green emission filter, and a 4X objective. The chip was placed under the compound microscope and faced up for image acquisition.

camera (Canon) for collecting images. The two LEDs, motorized filter flip mount, and the camera were controlled by a laptop for taking time-lapse green and red fluorescent images of on-chip co-culture experiments. Preliminary data acquired at JHMI were presented in Sec. 6.3.

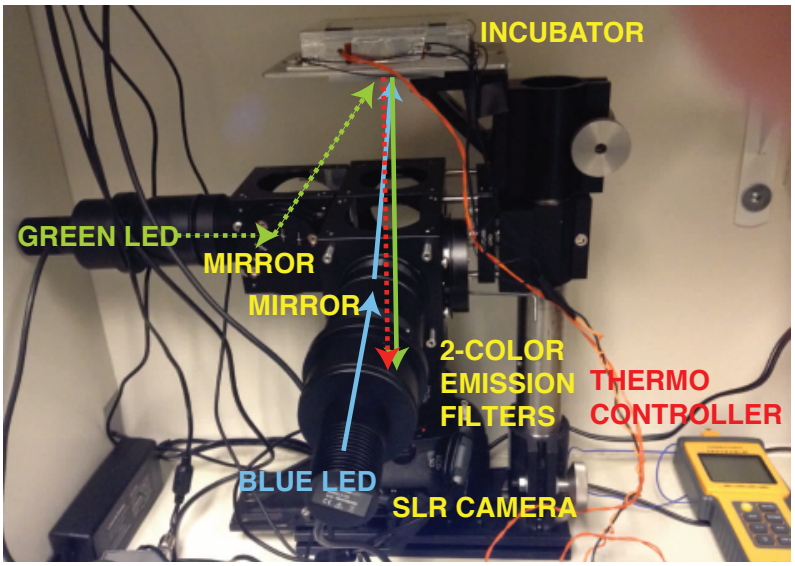

Figure A.4: **Dual-color (red and green) fluorescent imaging setup.** The bottom of the incubator provides a viewing window for on-chip live-cell imaging. The green LED excites red fluorescent cells (dotted arrows) and then the red fluorescent image is collected by the camera. Similarly, the blue LED excites green fluorescent cells (solid arrows) and then the green fluorescent image is collected by the camera.

Appendix B

Experiments

B.1 Device fabrication and flow characterization

The microfabrication process is performed in the Princeton Institute for the Science and Technology of Materials (PRISM) Micro/Nano Fabrication Laboratory (MNFL). The microstructure is drawn in L-Edit, and the chromium mask is written by a laser writer (Heidelberg DWL66). We use a mask aligner (Karl Suss MA6) to expose a silicon wafter coated with a 4 μm thick photoresist (AZ4330) and then developed by MIF300. The silicon structure was etched by reactive ion etching (RIE800iPB, Samco Inc, Japan).

The poly(dimethylsiloxane) (PDMS) devices (such as the pre-mixer, Sec. 2.1) were molded from an 120-μm deep silanized silicon mold using standard soft lithography techniques [100]. After punching the ports of the inlet and outlet by biopsy needles, the PDMS device was permanently bonded to glass slide via oxygen plasma treatment (Fig. B.1A).

Although PDMS soft lithography process is widely used in microfluidic technology, we switched from PDMS to silicon devices for cross-channel diffuser (Sec. **??** and devices in Chapter 4-5). It is because for such design, the micro posts at the sides are

hard to be transferred from the mold. Also, PDMS devices are permanently sealed by oxygen plasma, in which the cells are not collectable for other biological analysis such as RNA sequencing in Chapterch:MMEvo.

The silicon devices (150-μm deep) were made using standard photolithography technology. Then holes were sandblasted through the substrate so that fluidics could flow from the bottom of the substrate to the device on the top surface. We then remove the photoresist using acetone and then perform oxygen plasma to clean the silicon device. The top of the device was reversibly sealed by a PDMS-coated glass slide (baked at 60^{o}C for 2 hours), clamped by a polycarbonate manifold allowing liquids input and output to the through holes on the back of the chips, as shown in Fig. B.1B.

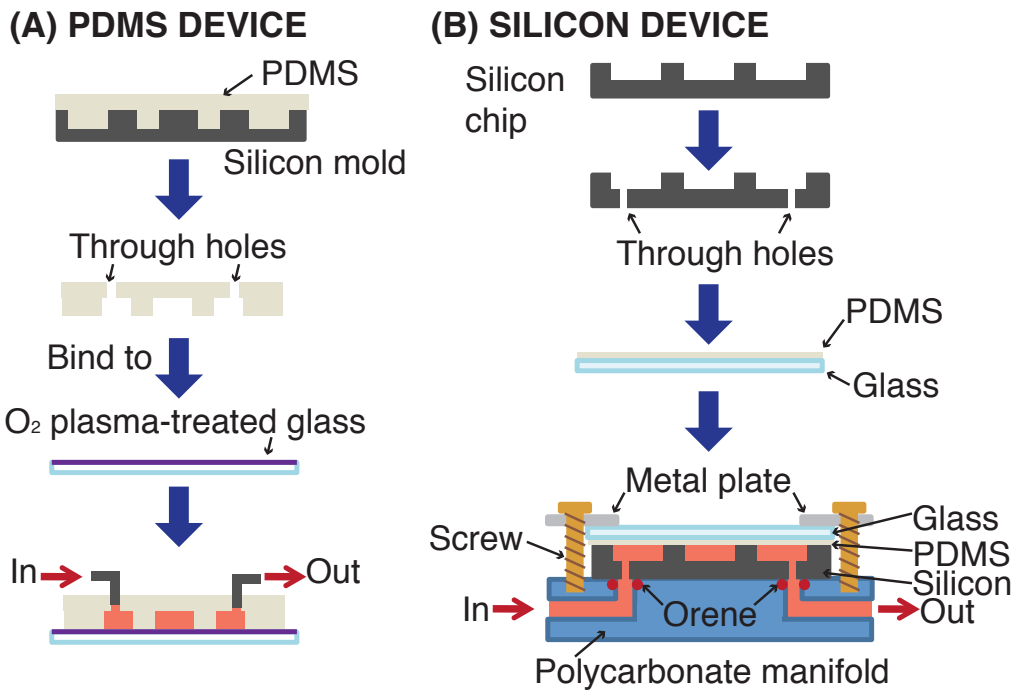

Figure B.1: **Microfluidic device fabrication and packaging process.** A. PDMS device. B. Silicon device.

For all devices described in this thesis, we constructed a concentration gradient by continuously supplying drug solution at source inlet, and drug-free solution at

sink inlet (Fig. 2.1A, Fig. 2.3A, Fig. 4.1A). To visualize the concentration gradient, we pumped growth medium dissolved with sodium fluorescein (Sigma-Aldrich) at the source inlet and growth medium alone at the sink inlet using a syringe pump (Chemyx Inc, USA). The diffusion coefficient of sodium fluorescein (D=4.04x10$^{-10}m^2$/s) is similar to that of doxorubicin (D=3.58x10$^{-10}m^2$/s), a common chemotherapeutic drug. The diffusion coefficients were calculated based on their molecular weights [101].

The flow speed in the culture chamber was measured by pumping fluorescent polystyrene beads (with the diameter of 1 μm) into source and sink channels and then tracking the bead trajectories from the image with the exposure time of 2 seconds.

B.2 Cell lines and cell culture protocol

The MDA-MB-231 breast cancer cells were provided by Thea Tlsty's lab (University of California, San Francisco) and were cultured in growth medium (DMEM supplemented with 10 % fetal bovine serum, 1 % penicillin-streptomycin) in an incubator with 5 % CO_2 and 37^oC.

The MDA-MB-231/GFP breast cancer cells expressing green fluorescent protein were provided by Beverly Emerson's lab (Salk Institute).

The MDA-MB-231 cells expressing red fluorescent histones were transduced with H2B-RFP LentiBrite vector (Millipore) by Karen Malatesta in our lab. We mixed 2×10^5 MDA-MB-231 cells (no fluorescent) with lentiviral particles at a minimum of $4 - 4.5 \times 10^6$ infectious units (IFU). The multiplicity of infection (MOI), defined as ratio of "number of IFU" to "number of cells being infected", was 20-23 in our samples. A week after the transduction, the red fluorescent cells were selected by fluorescence-activated cell sorting (FACS) flow cytometry.

The RPMI-8226/RFP multiple myeloma cells and HS-5/GFP bone marrow stromal cells were provided by Robert Gatenby's lab (Moffitt Cancer Center) and were cultured in growth medium (RPMI-1640 supplemented with 10 % fetal bovine serum, 1 % penicillin-streptomycin) in an incubator with 5 % CO_2 and 37^oC.

B.3 On-chip cell culture: 2D

Breast cancer cells and epithelial cells are adherent cells. In conventional cell culture, these cells are typically grown on tissue-culture polystyrenesubstrates. However, tissue-culture polystyrene can be challenging to use because it cannot bond to PDMS and is poorly compatible with microfabrication of the substrate (limited solvent resistance) [23]. Therefore, cell substrates such as glass or silicon substrates, used in microfluidic devices, require further protein coating to enable cell adherence and growth.

In Chapter 2, the silicon cross-channel mixer was coated with fibronectin (Sigma-Aldrich) with a density of 6 $\mu g/\mu m^2$ prior to cell seeding. To coat fibronectin, first we performed oxygen plasma treatment on the silicon device. The silicon device became hydrophilic, we then covered it with a 1-mm thick glass slide with PDMS film (about 50 μm thick), and dropped 10μL of the fibronectin solution (50μg/mL in phosphate buffer saline) from the through holes at the backside of the device. The fibronectin solution was then absorbed into inner channels in the device due to its hydrophilic surface. We then kept the device faced up to let the fibronectin molecules sediment on the cell culture region of the device for 30 minutes. We packaged the device with a manifold as illustrated in Fig. B.1B.

The PDMS device (used in Sec. 2.1), after sealing, was coated with 0.1% gelatin by incubation for 1 hour to promote the cell attachment onto the glass substrate. After removing the gelatin solution, the culture chamber was filled with growth medium.

For both devices, the suspended breast cancer cells were then gently seeded into the microfluidic device via the cell inlet at a density of two millions cells/ml and were allowed to attach to the substrate by overnight incubation. After 24 hours of static incubation, the growth medium and the drug solution was supplied continuously.

B.4 On-chip cell culture: 3D

In Chapter 4 and 5, multiple myeloma cells (8226/RFP) (and stromal cells, HS-5/GFP) were mixed with 33% matrigel and dropped on the silicon culture chamber previously coated by fibronectin (6 μg/(μm^2)), then sealed by another PDMS-coated glass slide. The device loaded with cells was placed in a standard incubator with 5% CO_2 and 37^oC overnight before the drug gradient was turned on. A stable gradient was established by continuously pumping growth medium (RPMI 1640 with 10% fetal bovine serum) containing doxorubicin at the source channel (top, Dox+) and growth medium alone at the sink channel (bottom, nutrient channel, Dox-) at a flow rate of 30 μl/hour.

B.5 Image acquisition and analysis

The cell population was determined by a threshold-based automatic counting software (Matlab) that was calibrated with manual counting. The cell trajectories and divisions were traced using u-track, a multiple-particle tracking Matlab software developed by Danuser Lab at Harvard University [33].

B.6 Characterization of DNA damage

The OxiSelect Comet Assay Kit (Cell Biolabs, Inc), a Single Cell Gel Electrophoresis assay (SCGE), was used to quantify the DNA fragmentation of the cells induced

by doxorubicin. After 72 hours of doxorubicin exposure, the cells were collected from the microfluidic device by scraping with a Rubber Policeman (Fisher Scientific). The cells were then combined with agarose and then treated with a lysis buffer and alkaline solution, which relaxes and denatures the DNA. Finally, the samples were electrophoresed to separate the intact DNA from damaged fragments. By staining with a DNA fluorescent dye, the migration of the damaged DNA (a "comet tail") was visualized by a epifluorescence microscope. The tail moment length is measured from the center of the head to the center of the tail.

B.7 Cell collection from the device and characterization of the dose response

After applying drug gradient to the cells for two weeks, the PDMS lid on the device was removed using a razor blade. Then the cells in the device were pipetted and transferred to a petri dish with growth medium at 37^oC in a conventional incubator. After expanding the population at drug-free medium (in tissue culture flasks for two weeks), Cell Proliferation kit (XTT) from Roche was used to characterize doxorubicin dose response of cells to determine its inhibition concentration of 50% of controlled population (IC_{50}). The assay is based on the cleavage of the yellow tetrazolium salt XTT to form an orange formazan dye by metabolic active cells, or viable cells. The formazan dye is soluble in aqueous solutions and is directly quantified using a scanning multi well spectrophotometer (Chromate plate reader, Allmedtech). Dose response curves were fitted by using Hill equation: $1 - V = \frac{E}{E_{max}} = \frac{C}{IC_{50}+C} + \epsilon$, where V: viability (%), E: drug effect, C: drug concentration, ϵ: constant [102].

B.8 Transcriptome sequencing

We collected about 100 cells from each DR sample, and then expanded them into 10000 cells for transcriptome sequencing. RNA extraction was performed using Absolutely RNA Nanoprep Kit (Agilent) at Robert Austin's Laboratory and the RNA concentration was determined on the Agilent 2100 Bioanalyzer (Agilent) by Sophia Li at Lewis-Sigler Institute for Integrative Genomics at Princeton University . Poly-A-enrichment of mRNA and cDNA library construction were performed by Jimmy Perrot from Nader Pourmand Laboratory at University of California at Santa Cruz. The RNA samples were sequenced using the Illumina HiSeq platform at Nader Pourmand's Laboratory at University of California at Santa Cruz, yielding 27-111 million 100bp paired-end high quality reads per sample.

Appendix C

Data Analysis

C.1 Significance analysis: cell migration

Significant test for a drift towards the high drug region: Based on the 72-hour trajectories for the 12 individual cells, 9 out of 12 cells migrated toward the high drug region (with final Y displacement is greater than 0). We design a significant test based on a binomial distribution B(n,p) where n is the cell counts and p is the probability of cells migrated toward the high drug region (with final Y displacement is greater than 0). If there is no significant drift toward the high or low drug region, p should be equal to 0.5.

Null hypothesis (H_0): p_0=0.5. Unbiased random walk dominates the cell migration in the doxorubicin gradient.

Alternative hypothesis (H_1): $p_0 \neq 0.5$. There is a bias in cell migration in the doxorubicin gradient.

Let n_1 be the number of cells migrated toward the high drug region, n is the total number of tracked cells, $p=n_1/n=9/12=0.75$. The 95% confidence interval based on the Wald method is $(p-1.96\sqrt{p(1-p)/n}, p+1.96\sqrt{p(1-p)/n})$=(0.505,0.995). The

null value p_0 is not in the 95% confidence interval. Thus, there is a bias of cell motion in Y-direction toward the high drug region during the 72-hour period.

C.2 Mapping, SNVs, and expression analyses

The sequencing data analyses were performed by Amy Wu at Princeton University, with the guidance of John Kim from Nader Pourmand's Laboratory at University of California at Santa Cruz. All the pipelines and bash scripts can be found at computer cluster MHP-3 at Room 116 of Jadwin Hall, Princeton University.

FastQC was used to perform quality control of the reads. The majority of reads from each sample (50-75%) were uniquely aligned against human reference genome build GRCh37 (hg19) using TopHat [103]. The Genome Analysis Toolkit (GATK) [104] was used to identify single nucleotide variants (SNVs). We filtered the SNVs with coverage depth more than 20 reads, base quality greater than 20, and p-value smaller than 0.01. Since we collected about 10000 cells from each DR sample for sequencing, not all mutations may be present in every cell. To analyze mutated genes, we annotated them using Oncotator (www.broadinstitute.org/oncotator/). We used bedtools to find covered bases per gene. The transcript abundances (fragments per kilobase of exon per million mapped fragments, FPKM) were compared between DR and WT cells to asses differential expression levels using Cufflinks [105].

C.3 Spatial pattern of transcriptome mutation and chromatin organization.

Hi-C eigenvectors at 1Mb resolution for the lymphocyte cell line GM06990 were downloaded from the Gene Expression Omnibus (GEO) entry. According to the original

paper [106], eigenvector 1 was used for all chromosomes except chromosomes 4 and 5 for which eigenvector 2 was chosen.

C.4 95% confidence intervals (CI) of per base substitution rate

Mean mutation rate (μ) is calculated by "total number of exon SNVs" divided by "total number of successfully sequenced exon bases". Here, x is number of exon SNVs for a given gene. To determine the 95% CI of per base substitution rate, we need to know "for a given exonic length, the probability to detect more then x_{up} (or less than x_{low}) mutations would be less than 5%". Based on binomial distribution, for a given exon length of a gene (L), the probability of detecting "more" than x_{up} SNVs is: $P(x > x_{up}) = \sum_{x_{up}}^{L} \binom{L}{x} \mu^{x} (1-\mu)^{L-x}$.

for a given exonic length of a gene (L), the probability of detecting "less" than x_{low} SNVs is: $P(x < x_{low}) = \sum_{0}^{x_{low}} \binom{L}{x} \mu^{x} (1-\mu)^{L-x}$.

We looked for minimal integers x_{up} and maximal integers x_{low} such that $P(x > x_{up}) \leq 0.025$ and $P(x < x_{low}) \leq 0.025$ for a given exonic length. Then, the upper bound of 95% CI would be x_{up}/L and the lower bound of 95% CI would be x_{low}/L. Since x_{up} and x_{low} are integers, kinks are observed in 95% CI.

C.5 Statistical analyses of significantly mutated genes.

We performed statistical tests on the observed mutations across samples to identify genes that harbor mutations under selection during emergence of drug resistance. We first estimate a BMR, based on total de novo mutations and then identify genes mutated beyond this rate. Since we worked with RNA sequencing with Poly-A en-

richment, we preferentially selected the mature RNA to sequence. Therefore, we only calculated the BMR using mutations and coverage at the exome. In at least one sample, we successfully sequenced (depth >20 reads) 13714589 bases at the exome. We detected 2617 *de novo* mutations at the exome in at least one sample. It turns out that the BMR is 2.0×10^{-4}.

We used the standard test for each mutated genes by treating all mutations equally. Given a uniform probability for each position in a gene, a one-tailed binomial test was used to assess whether the observed mutation rate was significantly higher or lower than the binomial distribution. Then, we performed multiple hypotheses tests (one per gene) using the standard Benjamini-Hochberg procedure to look for significantly hyper-mutated genes (Table 4.5).

C.6 Evolutionary ages of genes

The ages of 19786 human genes were a courtesy from Paul Davies' laboratory at Arizona State University based on the relative positions of the genes' homologues in a phylogenetic tree.

C.7 Gaussian and Lorentzian fit

We performed the fitting of the expression ratio histogram by using "histfit" function and "lorentzfit" function in Matlab.

C.8 Analytical method for training payoffs coefficients in game theoretical model

The analytical method for training and validating population dynamics equations was developed by David Liao from Thea Tlsty's Laboratory at University of California at San Francisco [87].

When we consider the absolute population of each type of players (α and β), then the population rate equations can be written as:

$$\frac{d\alpha}{dt} = (Ap_\alpha + Bp_\beta)\alpha \tag{C.1}$$

$$\frac{d\beta}{dt} = (Cp_\alpha + Dp_\beta)\beta \tag{C.2}$$

where population fractions $p_\alpha = \alpha/(\alpha+\beta)$ and $p_\beta = \beta/(\alpha+\beta)$, fitness of each player are $f\alpha = Ap_\alpha + Bp_\beta$ and $f_\beta = Cp_\alpha + Dp_\beta$.

To train the parameters in equations C.1 and C.2, we first isolate individual equation parameters by considering how population sizes (composed by cells of type α and cells of type β) vary while one subpopulation dominates. More specifically, we need at least two co-culture datasets with initially $\alpha-$ or $\beta-$rich population compositions, as shown in Fig. C.1.

For example, one dataset is corresponding to a co-culture that is initially highly enriched in cells of type α, with $\alpha(0) = 10000$ cells and $\beta(0) = 100$ cells at initial time $t = 0$ (Fig. C.1a and b). In this case, p_α is nearly unity and p_β is nearly zero, so equation C.1 becomes

$$\frac{d\alpha}{dt} = A\alpha, \tag{C.3}$$

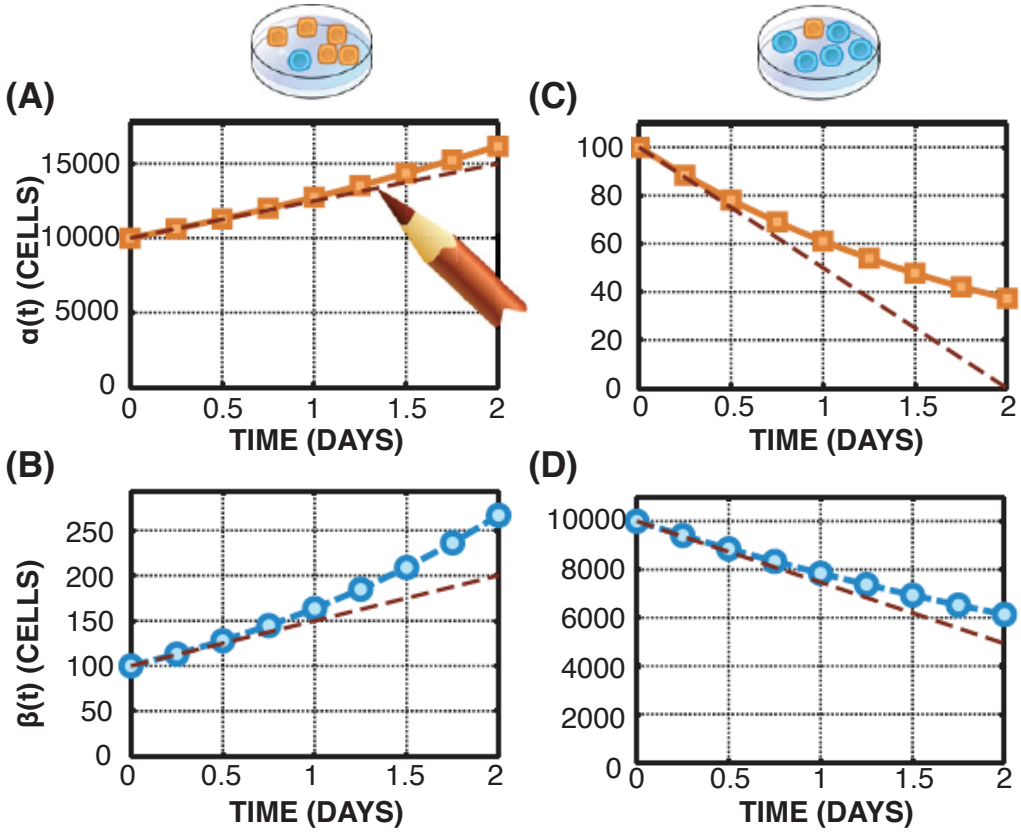

Figure C.1: **Training of population dynamics equations for an ecology consisting of two populations.** The number of cells of type α (A) and of type β (B) are monitored for a co-culture initially rich in cells of type α. The number of cells of type α (C) and of type β (D) are monitored for a co-culture initially rich in cells of type β. The slopes in (A)-(D) are used to specify the fitness in the phase diagram (Fig.5.4).

a simple proportionality between the instantaneous rate of change of population α and the population size α itself. This implies that

$$\frac{1}{\alpha}\frac{\delta\alpha}{\delta t} = A, \tag{C.4}$$

which means that the coefficient A is approximated by the product of the reciprocal of the population size α and the initial rate at which α changes. In Fig. C.1A, population α increases with curvature. The slope of the line tangent to the earliest data points covers a rise of $\delta\alpha = +5000$ cells over the course of $\delta t = 2$ days. Substituting these

values along with the initial population size of 10000 cells into equation C.4, we estimate

$$A = \frac{1}{10000cells}\frac{+5000cells}{2days} = 0.25day^{-1}. \tag{C.5}$$

The equation C.4 is equivalent to stating that the rate of change of the natural logarithm of α approximates A. Using a minimum least-square fitting of the plot of $ln(\alpha)$ versus t can provide an estimation of the parameter A.

Applying the arguments analogous to those we used to obtain equations C.3 to-C.5 allows us to use the slope of population β versus time in Fig. C.1B and equation C.2 to estimate that

$$C = \frac{1}{\beta}\frac{\delta\beta}{\delta t} = \frac{1}{100cells}\frac{+100cells}{2days} = 0.5day^{-1}. \tag{C.6}$$

To estimate the remaining parameters, we consider a co-culture initially rich in cells of type β. Setting p_α nearly equal to zero and p_β nearly equal to unity in equations C.1 and C.2 now allows us to use the plot of population α versus t in Fig. C.1C and the plot of population β versus t in Fig. C.1D to estimate that

$$B = \frac{1}{\alpha}\frac{\delta\alpha}{\delta t} = \frac{1}{100cells}\frac{-100cells}{2days} = -0.5day^{-1}. \tag{C.7}$$

and that

$$D = \frac{1}{\beta}\frac{\delta\beta}{\delta t} = \frac{1}{10000cells}\frac{-5000cells}{2days} = -0.25day^{-1}. \tag{C.8}$$

Now that we have determined the payoff parameter values by analyzing the dynamics of co-cultures with initially $\alpha-$ or $\beta-$rich population compositions.

C.9 Solving PDEs using finite-difference method

For most PDE problems, including game theoretical models, analytical solutions are difficult to obtain. To approximate the model equations by finite differences we divide the closed domain by a set of lines parallel to the spatial and time axes to form a grid or a mesh. The lines are equally spaced such that the distance between crossing points is Δx and Δt respectively. We seek approximations of the solution $MM(x_j, t_n)$ and $ST(x_j, t_n)$ to the game theory equation at these mesh points $(j\Delta x, n\Delta t)$;

$$\frac{\partial MM}{\partial t} = (A(x_j)p_{MM} + B(x_j)p_{ST})MM \tag{C.9}$$

$$\frac{\partial ST}{\partial t} = (C(x_j)p_{MM} + D(x_j)p_{ST})ST \tag{C.10}$$

where population fractions p_{MM}=MM/(MM+ST) and p_{ST}=ST/(MM+ST).

These approximate values will be denoted

$$\frac{MM(x_j, t_{n+1}) - MM(x_j, t_n)}{\Delta t} \approx (A(x_j)p_{MM(x_j,t_n)} + B(x_j)p_{ST(x_j,t_n)})MM(x_j, t_n) \tag{C.11}$$

$$\frac{ST(x_j, t_{n+1}) - ST(x_j, t_n)}{\Delta t} \approx (C(x_j)p_{MM(x_j,t_n)} + D(x_j)p_{ST(x_j,t_n)})ST(x_j, t_n) \tag{C.12}$$

In summary we obtain an approximation

$$MM(x_j, t_{n+1}) \approx MM(x_j, t_n) + \Delta t(A(x_j)p_{MM(x_j,t_n)} + B(x_j)p_{ST(x_j,t_n)})MM(x_j, t_n) \tag{C.13}$$

$$ST(x_j, t_{n+1}) \approx ST(x_j, t_n) + \Delta t(C(x_j)p_{MM(x_j,t_n)} + D(x_j)p_{ST(x_j,t_n)})ST(x_j, t_n) \tag{C.14}$$

Note that for a closed system, our cell culture region in the devices, we have Von Neumann boundary condition: cellular flux across the boundary is specified as zero ($\frac{\partial MM}{\partial n} = 0$ and $\frac{\partial ST}{\partial n} = 0$).

Appendix D

Publications and Presentations

Chapter 2 is based on works published in the *Proceedings of the National Academy of Sciences* [34]. Selected parts of Chapter 5 can be found in *Interface Focus*. As it is the policy with most of these journals, we include in the bibliography the appropriate copyright notices whenever we reproduce material directly from published articles. The publications and presentations as the outcome of my Ph.D. studies are listed below.

D.1 Refereed journal publication

1. **A. Wu**, D. Liao, V. Kirilin, R. A. Gatenby, T. D. Tlsty, J. C. Sturm, R. H. Austin. Criticality and dormancy in cancer community dynamics. *In preparation.*

2. **A. Wu**, Q. Zhang, G. Lambert, Z. Khin, R. A. Gatenby, H. Kim, N. Pourmand, K. Bussey, P. Davies, J. C. Sturm, R. H. Austin. Accelerating the emergence of chemotherapy resistance and the role of ancient mutational cold spots. *Under review.*

3. **A. Wu**, D. Liao, T. D. Tlsty, J. C. Sturm, R. H. Austin. (2014) Game theory in the Death Galaxy: interaction of cancer and stromal cells in tumor microenvironment. *Interface Focus*, 4, 20140028, 1-6.

4. **A. Wu**, K. Loutherback, G. Lambert, L. Estevez-Salmeron, T. D. Tlsty, R. H. Austin, J. C. Sturm. (2013) Cell motility and drug gradients in the emergence of resistance to chemotherapy. *Proceedings of the National Academy of Sciences*, 110, 40, 16103-16108.

5. L. Liu, G. Duclos, B. Sun, J. Lee, **A. Wu**, Y. Kam, E. D. Sontag, H. A. Stone, J. C. Sturm, R. A. Gatenby, R. H. Austin. (2013) Minimization of thermodynamic costs in cancer cell invasion. *Proceedings of the National Academy of Sciences*, 110, 5, 1686-1691.

6. K. Loutherback, J. D'Silva, L. Liu, **A. Wu**, R. H. Austin, J. C. Sturm. (2012) Deterministic separation of cancer cells from blood at 10 mL/min. *AIP Advances*, 2, 042107, 1-7.

D.2 Non-refereed articles

1. **A. Wu**, D. Liao, R. H. Austin. (2015) Game theory in cancer: a way to predict metastatic cancer progression? *Future Oncology*, 11 (6), 881-883.

2. **A. Wu**, J. C. Sturm, R. H. Austin. (2014) Big dirty data: looking in the wrong places for the Rosetta Stone. *Institute of Physics-Biological Physics Group Newsletter*, 8, 4-7.

D.3 Oral presentations

1. **(Invited talk)** A. Wu et al. Emergence of drug resistance in cancer chemotherapy: Galápagos Islands on a chip. *National Institute of Standards and Technology-Center for Nanoscale Science and Technology (CNST) Seminar*, Gaithersburg, MD (Jan. 2015)

2. **(Invited talk)** A. Wu et al. Emergence of drug resistance in cancer chemotherapy: Galápagos Islands on a chip. *Rising Stars in EECS workshop at University of California-Berkeley*, Berkeley, CA (Nov. 2014)

3. A. Wu, K. Malatesta, T. Epstein, R. H. Austin, J. C. Sturm. Tutorial of using the Death Galaxy for cancer. *Physical Sciences-Oncology Center Microhabitats workshop at Johns Hopkins Medical Institute*, Baltimore, MD (May 2014)

4. **(Invited talk)** A. Wu et al. Chemotherapy resistance in tumor microenvironment: from genomics to behavior modeling. *IBM Computational Biology Center Seminar*, Yorktown Heights, NY (Apr. 2014)

5. A. Wu, D. Liao, T. D. Tlsty, R. A. Gatenby, R. H. Austin, J. C. Sturm. Evolutionary game theory analysis of tumor progression. *Physical Sciences-Oncology Center Microhabitats workshop at University of California-San Francisco*, San Francisco, CA (Apr. 2014)

6. A. Wu, Q. Zhang, G. Lambert, Z. Khin, R. A. Gatenby, H. Kim, N. Pourmand, K. Bussey, P. Davies, J. C. Sturm, R. H. Austin. Finding haystacks and needles in the emergence of chemotherapy resistance. *American Physical Society March Meeting*, Denver, CO (Mar. 2014)

7. **(Invited talk)** A. Wu et al. Probing the horizontal gene transfer in cancer. *Computational and Theoretical Biology Symposium*, Rice University, Houston, TX (Dec. 2013)

8. A. Wu, F. Lopez-Diaz, C. McFarland, L. Mirny, B. Emerson, R. H. Austin, J. C. Sturm. Direct visualization of the role of horizontal gene transfer in the evolution of drug resistance in cancer. *Princeton Physical Sciences-Oncology Center Site Visit at Salk Institute*, La Jolla, CA (Sep. 2013)

9. **(Invited talk)** A. Wu et al. Game theory in the Death Galaxy: microhabitats, drug gradients, and myeloma-stroma co-culture. *Workshop on Game Theory and Cancer, Johns Hopkins Medical Institute*, Baltimore, MD (Aug. 2013)

10. A. Wu, K. Loutherback, G. Lambert, L. Estevez-Salmeron, T. D. Tlsty, R. H. Austin, J. C. Sturm. Population dynamics of breast cancer cells in a drug gradient. *Material Research Society Spring Meeting*, San Francisco, CA (Apr. 2013)

11. **(Invited talk)** A. Wu et al. Physics of evolution in cancer: the roles of microenvironmental and genetic heterogeneity. *Evolution of Cancer Symposium*, Brown University, Providence, RI (May 2013)

12. **(APS news highlight)** A. Wu, Q. Zhang, G. Lambert, Z. Khin, R. A. Gatenby, H. Kim, N. Pourmand, K. Bussey, P. Davies, J. C. Sturm, R. H. Austin. Rapid evolution of drug resistance of multiple myeloma in the microenvironment with drug gradients. *American Physical Society March Meeting*, Baltimore, MD (Mar. 2013)

13. A. Wu, Q. Zhang, G. Lambert, Z. Khin, R. A. Gatenby, H. Kim, N. Pourmand, K. Bussey, P. Davies, J. C. Sturm, R. H. Austin. Emergence of therapy resistance in multiple myeloma: the roles of genomic and microenvironmental heterogeneity. *Princeton Physical Sciences-Oncology Center Site Visit at Princeton*, Princeton, NJ (Sep. 2012)

14. **(Invited talk)** A. Wu et al. Evolution of drug resistance of multiple myeloma in microfluidic Death Alcatraz. *Chinese Academy of Sciences and Physical Sciences-Oncology Centers (CAS-PSOC) Cancer Biophysics Summer Workshop*, Beijing, China (Jun. 2012)

15. A. Wu, Q. Zhang, G. Lambert, Z. Khin, R. A. Gatenby, H. Kim, N. Pourmand, K. Bussey, P. Davies, J. C. Sturm, R. H. Austin. Evolution of drug resistance of multiple myeloma in gradient micro environments. *The 3rd Annual Physical Sciences-Oncology Centers (PS-OCs) Network Investigators Meeting*, Tampa, FL (Apr. 2012)

16. A. Wu, D. Liao, T. D. Tlsty, R. A. Gatenby, R. H. Austin, J. C. Sturm. Cancer-stroma evolutionary dynamics in stress-gradient micro environments. *American Physical Society March Meeting*, Boston, MA (Mar. 2012)

17. A. Wu, K. Loutherback, G. Lambert, L. Estevez-Salmeron, T. D. Tlsty, R. H. Austin, J. C. Sturm. Stable and precise stress gradient microenvironment for study of cancer cell migration and proliferation. *Material Research Society Spring Meeting*, San Francisco, CA (Apr. 2011)

18. A. Wu, K. Loutherback, G. Lambert, L. Estevez-Salmeron, T. D. Tlsty, R. H. Austin, J. C. Sturm. Study of cancer cell behaviors in a stable stress gradient microenvironment. *American Physical Society March Meeting*, Dallas, TX (Mar. 2011)

D.4 Poster presentations

1. A. Wu, D. Liao, J. C. Sturm, R. H. Austin. Evolutionary game theory analysis of tumor progression. *The Annual Retreat on Cancer Research in New Jersey*, Piscataway, NJ (May 2014)

2. A. Wu, F. Lopez-Diaz, C. McFarland, L. Mirny, B. Emerson, R. H. Austin, J. C. Sturm. Direct visualization of the role of horizontal gene transfer in the evolution of drug resistance in cancer. *The 5th Annual Physical Sciences-Oncology Centers (PS-OCs) Network Investigators Meeting*, Bethesda, MD (2014)

3. A. Wu, D. Liao, J. C. Sturm, R. H. Austin. Evolutionary game theory analysis of tumor progression. *American Physical Society March Meeting*, Denver, CO (Mar. 2014)

4. A. Wu, Q. Zhang, G. Lambert, Z. Khin, R. A. Gatenby, H. Kim, N. Pourmand, K. Bussey, P. Davies, J. C. Sturm, R. H. Austin. Rapid evolution of drug resistance of multiple myeloma in the microenvironment with drug gradients. *Gordon Research Conference-Biological Mechanisms in Evolution*, Easton, MA (Jun. 2013)

5. A. Wu, K. Loutherback, G. Lambert, L. Estevez-Salmeron, T. D. Tlsty, R. H. Austin, J. C. Sturm. Population dynamics of breast cancer cells in a drug gradient. *The 4th Annual Physical Sciences-Oncology Centers (PS-OCs) Network Investigators Meeting*, Scottsdale, AZ (Apr. 2013)

6. A. Wu, G. Lambert, R. H. Austin, J. C. Sturm. Cancer adaptation to drug gradient in microfluidic microenvironment.*Spring Meeting, Material Research Society*, San Francisco, CA (Apr. 2012)

7. A. Wu, K. Loutherback, G. Lambert, L. Estevez-Salmeron, T. D. Tlsty, R. H. Austin, J. C. Sturm. Study of cancer cell migration and proliferation in a stable stress gradient microenvironment. *2nd Annual Physical Sciences-Oncology Centers (PS-OCs) Network Investigators Meeting*, La Jolla, CA (Apr. 2011)

Bibliography

[1] Hanahan, D & Weinberg, R. A. (2000) *Cell* **100**, 57–70.

[2] Vogelstein, B, Papadopoulos, N, Velculescu, V. E, Zhou, S, Diaz, L. A, & Kinzler, K. W. (2013) *Science* **339**, 1546–1558.

[3] Wright, S. (1932) *Proceedings of the sixth international congress of genetics* pp. 356–366.

[4] Zhang, Q, Lambert, G, Liao, D, Kim, H, Robin, K, Tung, C.-k, Pourmand, N, & Austin, R. H. (2011) *Science* **333**, 1764–1767.

[5] Lambert, G, Estvez-Salmeron, L, Oh, S, Liao, D, Emerson, B. M, Tlsty, T. D, & Austin, R. H. (2011) *Nat Rev Cancer* **11**, 375–382.

[6] Zhang, Q & Austin, R. H. (2012) *Annual Review of Condensed Matter Physics* **3**, 363–382.

[7] Meads, M. B, Hazlehurst, L. A, & Dalton, W. S. (2008) *Clinical Cancer Research* **14**, 2519–2526.

[8] McMillin, D. W, Delmore, J, Weisberg, E, Negri, J. M, Geer, D. C, Klippel, S, Mitsiades, N, Schlossman, R. L, Munshi, N. C, Kung, A. L, Griffin, J. D, Richardson, P. G, Anderson, K. C, & Mitsiades, C. S. (2010) *Nature Medicine* **16**, 483–489.

[9] Bozic, I, Antal, T, Ohtsuki, H, Carter, H, Kim, D, Chen, S, Karchin, R, Kinzler, K. W, Vogelstein, B, & Nowak, M. A. (2010) *Proceedings of the National Academy of Sciences* **107**, 18545–18550.

[10] Leder, K, Foo, J, Skaggs, B, Gorre, M, Sawyers, C. L, & Michor, F. (2011) *PLoS ONE* **6**, e27682.

[11] Greaves, M & Maley, C. C. (2012) *Nature* **481**, 306–313.

[12] Gillies, R. J & Gatenby, R. A. (2007) *Journal of Bioenergetics and Biomembranes* **39**, 251–257.

[13] Tredan, O, Galmarini, C. M, Patel, K, & Tannock, I. F. (2007) *JNCI Journal of the National Cancer Institute* **99**, 1441–1454.

[14] Keenan, T. M & Folch, A. (2007) *Lab Chip* **8**, 34–57.

[15] Walsh, C. L, Babin, B. M, Kasinskas, R. W, Foster, J. A, McGarry, M. J, & Forbes, N. S. (2009) *Lab on a Chip* **9**, 545.

[16] Chung, B. G & Choo, J. (2010) *Electrophoresis* **31**, 3014–3027.

[17] Abhyankar, V. V, Toepke, M. W, Cortesio, C. L, Lokuta, M. A, Huttenlocher, A, & Beebe, D. J. (2008) *Lab on a Chip* **8**, 1507.

[18] Kim, D, Lokuta, M. A, Huttenlocher, A, & Beebe, D. J. (2009) *Lab on a Chip* **9**, 1797.

[19] Jeon, N. L, Dertinger, S. K. W, Chiu, D. T, Choi, I. S, Stroock, A. D, & Whitesides, G. M. (2000) *Langmuir* **16**, 8311–8316.

[20] Li Jeon, N, Baskaran, H, Dertinger, S. K. W, Whitesides, G. M, Van De Water, L, & Toner, M. (2002) *Nature Biotechnology*.

[21] Paliwal, S, Iglesias, P. A, Campbell, K, Hilioti, Z, Groisman, A, & Levchenko, A. (2007) *Nature* **446**, 46–51.

[22] Cimetta, E, Cannizzaro, C, James, R, Biechele, T, Moon, R. T, Elvassore, N, & Vunjak-Novakovic, G. (2010) *Lab on a Chip* **10**, 3277.

[23] Kim, L, Toh, Y.-C, Voldman, J, & Yu, H. (2007) *Lab on a Chip* **7**, 681–694.

[24] Regehr, K. J, Domenech, M, Koepsel, J. T, Carver, K. C, Ellison-Zelski, S. J, Murphy, W. L, Schuler, L. A, Alarid, E. T, & Beebe, D. J. (2009) *Lab on a chip* **9**, 2132–2139.

[25] Wang, S.-J, Saadi, W, Lin, F, Minh-Canh Nguyen, C, & Li Jeon, N. (2004) *Experimental Cell Research* **300**, 180–189.

[26] Davies, P. F, Barbee, K. A, Volin, M. V, Robotewskyj, A, Chen, J, Joseph, L, Griem, M. L, Wernick, M. N, Jacobs, E, Polacek, D. C, DePaola, N, & Barakat, A. I. (1997) *Annual Review of Physiology* **59**, 527–549.

[27] Mosadegh, B, Huang, C, Park, J. W, Shin, H. S, Chung, B. G, Hwang, S.-K, Lee, K.-H, Kim, H. J, Brody, J, & Jeon, N. L. (2007) *Langmuir* **23**, 10910–10912.

[28] Shieh, A. C, Rozansky, H. A, Hinz, B, & Swartz, M. A. (2011) *Cancer Research* **71**, 790–800.

[29] Smith, L. (2006) *Molecular Cancer Therapeutics* **5**, 2115–2120.

[30] Gouaz-Andersson, V, Yu, J. Y, Kreitenberg, A. J, Bielawska, A, Giuliano, A. E, & Cabot, M. C. (2007) *Biochimica et Biophysica Acta (BBA) - Molecular and Cell Biology of Lipids* **1771**, 1407–1417.

[31] Aroui, S, Ram, N, Appaix, F, Ronjat, M, Kenani, A, Pirollet, F, & Waard, M. (2008) *Pharmaceutical Research* **26**, 836–845.

[32] Liu, L, Duclos, G, Sun, B, Lee, J, Wu, A, Kam, Y, Sontag, E. D, Stone, H. A, Sturm, J. C, Gatenby, R. A, & Austin, R. H. (2013) *Proceedings of the National Academy of Sciences* **110**, 1686–1691.

[33] Jaqaman, K, Loerke, D, Mettlen, M, Kuwata, H, Grinstein, S, Schmid, S. L, & Danuser, G. (2008) *Nature Methods* **5**, 695–702.

[34] Wu, A, Loutherback, K, Lambert, G, Estevez-Salmeron, L, Tlsty, T. D, Austin, R. H, & Sturm, J. C. (2013) *Proceedings of the National Academy of Sciences* **110**, 16103–16108.

[35] Bergsmedh, A, Szeles, A, Henriksson, M, Bratt, A, Folkman, M. J, Spetz, A.-L, & Holmgren, L. (2001) *Proceedings of the National Academy of Sciences* **98**, 6407–6411.

[36] Holmgren, L. (2010) *Biochemical and Biophysical Research Communications* **396**, 147–151.

[37] Pawelek, J. M & Chakraborty, A. K. (2008) *Nature Reviews Cancer* **8**, 377–386.

[38] Babic, A, Lindner, A. B, Vulic, M, Stewart, E. J, & Radman, M. (2008) *Science* **319**, 1533–1536.

[39] Canchaya, C, Fournous, G, Chibani-Chennoufi, S, Dillmann, M.-L, & Brssow, H. (2003) *Current Opinion in Microbiology* **6**, 417–424.

[40] Mahindra, A, Laubach, J, Raje, N, Munshi, N, Richardson, P. G, & Anderson, K. (2012) *Nature Reviews Clinical Oncology* **9**, 135–143.

[41] Mercier, F. E, Ragu, C, & Scadden, D. T. (2011) *Nature Reviews Immunology* **12**, 49–60.

[42] Torisawa, Y.-s, Spina, C. S, Mammoto, T, Mammoto, A, Weaver, J. C, Tat, T, Collins, J. J, & Ingber, D. E. (2014) *Nature Methods* **11**, 663–669.

[43] Hermsen, R & Hwa, T. (2010) *Physical Review Letters* **105**.

[44] Lawrence, M. S, Stojanov, P, Polak, P, Kryukov, G. V, Cibulskis, K, Sivachenko, A, Carter, S. L, Stewart, C, Mermel, C. H, Roberts, S. A, Kiezun, A, Hammerman, P. S, McKenna, A, Drier, Y, Zou, L, Ramos, A. H, Pugh, T. J, Stransky, N, Helman, E, Kim, J, Sougnez, C, Ambrogio, L, Nickerson, E, Shefler, E, Corts, M. L, Auclair, D, Saksena, G, Voet, D, Noble, M, DiCara, D, Lin, P, Lichtenstein, L, Heiman, D. I, Fennell, T, Imielinski, M, Hernandez, B, Hodis, E, Baca, S, Dulak, A. M, Lohr, J, Landau, D.-A, Wu, C. J, Melendez-Zajgla, J, Hidalgo-Miranda, A, Koren, A, McCarroll, S. A, Mora, J, Lee, R. S, Crompton, B, Onofrio, R, Parkin, M, Winckler, W, Ardlie, K, Gabriel, S. B, Roberts, C.

W. M, Biegel, J. A, Stegmaier, K, Bass, A. J, Garraway, L. A, Meyerson, M, Golub, T. R, Gordenin, D. A, Sunyaev, S, Lander, E. S, & Getz, G. (2013) *Nature* **499**, 214–218.

[45] Bozic, I, Antal, T, Ohtsuki, H, Carter, H, Kim, D, Chen, S, Karchin, R, Kinzler, K. W, Vogelstein, B, & Nowak, M. A. (2010) *Proceedings of the National Academy of Sciences* **107**, 18545–18550.

[46] MacLean, R. C, Torres-Barcel, C, & Moxon, R. (2013) *Nature Reviews Genetics* **14**, 221–227.

[47] Calcagno, A. M & Ambudkar, S. V. (2010) in *Multi-Drug Resistance in Cancer*, ed. Zhou, J. (Humana Press, Totowa, NJ) Vol. 596, pp. 77–93.

[48] Simon, R & Norton, L. (2006) *Nature Clinical Practice Oncology* **3**, 406–407.

[49] Muller, H. J. (1932) *The American Naturalist* **66**, 118.

[50] Zhang, Q, Robin, K, Liao, D, Lambert, G, & Austin, R. H. (2011) *Molecular Pharmaceutics* **8**, 2063–2068.

[51] Darnton, N. C, Turner, L, Rojevsky, S, & Berg, H. C. (2006) *Journal of Bacteriology* **189**, 1756–1764.

[52] Pathak, A & Kumar, S. (2012) *Proceedings of the National Academy of Sciences* **109**, 10334–10339.

[53] Dalton, W. S, Durle, B. G. M, Alberts, D. S, Gerlach, J. H, & Cress, A. E. (1986) *Cancer Research* **46**, 5125–5130.

[54] Damiano, J. S, Cress, A. E, Hazlehurst, L. A, Shtil, A. A, & Dalton, W. S. (1999) *Blood* **93**, 1658–1667.

[55] Meads, M. B, Gatenby, R. A, & Dalton, W. S. (2009) *Nature Reviews Cancer* **9**, 665–674.

[56] Lang, G. I, Rice, D. P, Hickman, M. J, Sodergren, E, Weinstock, G. M, Botstein, D, & Desai, M. M. (2013) *Nature* **500**, 571–574.

[57] Shaffer, J. P. (1995) *Annual Review of Psychology* **46**, 561–584.

[58] Davies, P. C. W & Lineweaver, C. H. (2011) *Physical Biology* **8**, 015001.

[59] Davies, P. (2013) *Physics World* **26**, 37–40.

[60] Mi, H, Muruganujan, A, Casagrande, J. T, & Thomas, P. D. (2013) *Nature Protocols* **8**, 1551–1566.

[61] Minotti, G. (2004) *Pharmacological Reviews* **56**, 185–229.

[62] Brody, J. P, Williams, B. A, Wold, B. J, & Quake, S. R. (2002) *Proceedings of the National Academy of Sciences* **99**, 12975–12978.

[63] Bejerano, G. (2004) *Science* **304**, 1321–1325.

[64] Aktipis, C. A, Boddy, A. M, Gatenby, R. A, Brown, J. S, & Maley, C. C. (2013) *Nature Reviews Cancer* **13**, 883–892.

[65] He, J, Sun, J, & Deem, M. W. (2009) *Physical Review E* **79**.

[66] Tan, T, Frenkel, D, Gupta, V, & Deem, M. W. (2005) *Physica A: Statistical Mechanics and its Applications* **350**, 52–62.

[67] He, J & Deem, M. W. (2010) *Developmental Biology* **337**, 157–161.

[68] Hurley, L. H. (2002) *Nature Reviews Cancer* **2**, 188–200.

[69] Maga, G, Crespan, E, Markkanen, E, Imhof, R, Furrer, A, Villani, G, Hubscher, U, & van Loon, B. (2013) *Proceedings of the National Academy of Sciences* **110**, 18850–18855.

[70] SnchezAlvarado, A. (2012) *Current Biology* **22**, R772–R778.

[71] Chen, H, Lin, F, Xing, K, & He, X. (2015) *Nature Communications* **6**, 6367.

[72] Bardelli, A, Corso, S, Bertotti, A, Hobor, S, Valtorta, E, Siravegna, G, Sartore-Bianchi, A, Scala, E, Cassingena, A, Zecchin, D, Apicella, M, Migliardi, G, Galimi, F, Lauricella, C, Zanon, C, Perera, T, Veronese, S, Corti, G, Amatu, A, Gambacorta, M, Diaz, L. A, Sausen, M, Velculescu, V. E, Comoglio, P, Trusolino, L, Di Nicolantonio, F, Giordano, S, & Siena, S. (2013) *Cancer Discovery* **3**, 658–673.

[73] Tlsty, T. D & Coussens, L. M. (2006) *Annual Review of Pathology: Mechanisms of Disease* **1**, 119–150.

[74] Sun, Y, Campisi, J, Higano, C, Beer, T. M, Porter, P, Coleman, I, True, L, & Nelson, P. S. (2012) *Nature Medicine* **18**, 1359–1368.

[75] Nefedova, Y. (2004) *Blood* **103**, 3503–3510.

[76] Wilson, T. R, Fridlyand, J, Yan, Y, Penuel, E, Burton, L, Chan, E, Peng, J, Lin, E, Wang, Y, Sosman, J, Ribas, A, Li, J, Moffat, J, Sutherlin, D. P, Koeppen, H, Merchant, M, Neve, R, & Settleman, J. (2012) *Nature* **487**, 505–509.

[77] Maynard Smith, J. (1982) *Evolution and the theory of games*. (Cambridge University Press, Cambridge ; New York).

[78] Taylor, C & Nowak, M. A. (2007) *Evolution* **61**, 2281–2292.

[79] Dingli, D, Chalub, F. A. C. C, Santos, F. C, Van Segbroeck, S, & Pacheco, J. M. (2009) *British Journal of Cancer* **101**, 1130–1136.

[80] Basanta, D, Scott, J. G, Rockne, R, Swanson, K. R, & Anderson, A. R. A. (2011) *Physical Biology* **8**, 015016.

[81] Flach, E. H, Rebecca, V. W, Herlyn, M, Smalley, K. S. M, & Anderson, A. R. A. (2011) *Molecular Pharmaceutics* **8**, 2039–2049.

[82] Primeau, A. J. (2005) *Clinical Cancer Research* **11**, 8782–8788.

[83] Arendt, L. M, Rudnick, J. A, Keller, P. J, & Kuperwasser, C. (2010) *Seminars in Cell & Developmental Biology* **21**, 11–18.

[84] Liu, L, Sun, B, Pedersen, J. N, Aw Yong, K.-M, Getzenberg, R. H, Stone, H. A, & Austin, R. H. (2011) *Proceedings of the National Academy of Sciences* **108**, 6853–6856.

[85] Melin, J & Quake, S. R. (2007) *Annual Review of Biophysics and Biomolecular Structure* **36**, 213–231.

[86] Anderson, K. C, Alsina, M, Bensinger, W, Biermann, J. S, Chanan-Khan, A, Cohen, A. D, Devine, S, Djulbegovic, B, Faber, E. A, Gasparetto, C, Huff, C. A, Kassim, A, Medeiros, B. C, Meredith, R, Raje, N, Schriber, J, Singhal, S, Somolo, G, Stockerl-Goldstein, K, Treon, S. P, Tricot, G, Weber, D. M, Yahalom, J, & Yunus, F. (2011) *Journal of the National Comprehensive Cancer Network* **9**, 1146–1183.

[87] Liao, D & Tlsty, T. D. (2014) *Interface Focus* **4**, 20140037–20140037.

[88] Liao, D & Tlsty, T. D. (2014) *Interface Focus* **4**, 20140038–20140038.

[89] deForest, R & Belmonte, A. (2013) *Physical Review E* **87**.

[90] Rees, D. C, Johnson, E, & Lewinson, O. (2009) *Nature Reviews Molecular Cell Biology* **10**, 218–227.

[91] Anderson, A. R, Hassanein, M, Branch, K. M, Lu, J, Lobdell, N. A, Maier, J, Basanta, D, Weidow, B, Narasanna, A, Arteaga, C. L, Reynolds, A. B, Quaranta, V, Estrada, L, & Weaver, A. M. (2009) *Cancer Research* **69**, 8797–8806.

[92] Gatenby, R. A, Grove, O, & Gillies, R. J. (2013) *Radiology* **269**, 8–14.

[93] Scott, J, Kuhn, P, & Anderson, A. R. A. (2012) *Nature Reviews Cancer* **12**, 445–446.

[94] Liao, D, Estvez-Salmern, L, & Tlsty, T. D. (2012) *Physical Biology* **9**, 065005.

[95] Seidman, A. D, Berry, D, Cirrincione, C, Harris, L, Muss, H, Marcom, P. K, Gipson, G, Burstein, H, Lake, D, Shapiro, C. L, Ungaro, P, Norton, L, Winer, E, & Hudis, C. (2008) *Journal of Clinical Oncology* **26**, 1642–1649.

[96] Liao, D, Estvez-Salmern, L, & Tlsty, T. D. (2012) *Physical Biology* **9**, 065006.

[97] Johnston, R. N, Beverley, S. M, & Schimke, R. T. (1983) *Proceedings of the National Academy of Sciences of the United States of America* **80**, 3711–3715.

[98] Rath, H, Tlsty, T, & Schimke, R. T. (1984) *Cancer Research* **44**, 3303–3306.

[99] Lpez-Daz, F, Gascard, P, Balakrishnan, S, Zhao, J, delRincon, S, Spruck, C, Tlsty, T, & Emerson, B. (2013) *Molecular Cell* **50**, 552–564.

[100] Xia, Y & Whitesides, G. M. (1998) *Annual Review of Materials Science* **28**, 153–184.

[101] Krouglova, T, Vercammen, J, & Engelborghs, Y. (2004) *Biophysical Journal* **87**, 2635–2646.

[102] Goutelle, S, Maurin, M, Rougier, F, Barbaut, X, Bourguignon, L, Ducher, M, & Maire, P. (2008) *Fundamental & Clinical Pharmacology* **22**, 633–648.

[103] Trapnell, C, Pachter, L, & Salzberg, S. L. (2009) *Bioinformatics* **25**, 1105–1111.

[104] DePristo, M. A, Banks, E, Poplin, R, Garimella, K. V, Maguire, J. R, Hartl, C, Philippakis, A. A, del Angel, G, Rivas, M. A, Hanna, M, McKenna, A, Fennell, T. J, Kernytsky, A. M, Sivachenko, A. Y, Cibulskis, K, Gabriel, S. B, Altshuler, D, & Daly, M. J. (2011) *Nature Genetics* **43**, 491–498.

[105] Trapnell, C, Roberts, A, Goff, L, Pertea, G, Kim, D, Kelley, D. R, Pimentel, H, Salzberg, S. L, Rinn, J. L, & Pachter, L. (2012) *Nature Protocols* **7**, 562–578.

[106] Lieberman-Aiden, E, van Berkum, N. L, Williams, L, Imakaev, M, Ragoczy, T, Telling, A, Amit, I, Lajoie, B. R, Sabo, P. J, Dorschner, M. O, Sandstrom, R, Bernstein, B, Bender, M. A, Groudine, M, Gnirke, A, Stamatoyannopoulos, J, Mirny, L. A, Lander, E. S, & Dekker, J. (2009) *Science* **326**, 289–293.